

Electronic Thesis and Dissertation Repository

10-3-2012 12:00 AM


Studies of Microscopic Scale Strains in Nickel Alloys Resulting from Mechanical and Chemical Forces

Jing Chao
The University of Western Ontario

Supervisor
Stewart McIntyre
The University of Western Ontario

Graduate Program in Chemistry
A thesis submitted in partial fulfillment of the requirements for the degree in Doctor of Philosophy
© Jing Chao 2012

Follow this and additional works at: <https://ir.lib.uwo.ca/etd>

 Part of the [Analytical Chemistry Commons](#), [Materials Chemistry Commons](#), and the [Physical Chemistry Commons](#)

Recommended Citation

Chao, Jing, "Studies of Microscopic Scale Strains in Nickel Alloys Resulting from Mechanical and Chemical Forces" (2012). *Electronic Thesis and Dissertation Repository*. 900.
<https://ir.lib.uwo.ca/etd/900>

This Dissertation/Thesis is brought to you for free and open access by Scholarship@Western. It has been accepted for inclusion in Electronic Thesis and Dissertation Repository by an authorized administrator of Scholarship@Western. For more information, please contact wlsadmin@uwo.ca.

Studies of Microscopic Scale Strains in Nickel Alloys Resulting from Mechanical and
Chemical Forces

(Spine title: Studies of Microscopic Scale Strains in Nickel Alloys)

(Thesis format: Monograph)

by

Jing Chao

Graduate Program in Chemistry

A thesis submitted in partial fulfillment
of the requirements for the degree of
Doctor of Philosophy

The School of Graduate and Postdoctoral Studies
The University of Western Ontario
London, Ontario, Canada

© Jing Chao 2012

THE UNIVERSITY OF WESTERN ONTARIO
School of Graduate and Postdoctoral Studies

CERTIFICATE OF EXAMINATION

Supervisor

Examiners

Dr. N. Stewart McIntyre

Dr. Gary Was

Supervisory Committee

Dr. Sean Shieh

Dr.

Dr. David Shoesmith

Dr.

Dr. Viktor N. Staroverov

The thesis by

Jing Chao

entitled:

**Studies of Microscopic Scale Strains in Nickel Alloys Resulting
from Mechanical and Chemical Forces**

is accepted in partial fulfillment of the
requirements for the degree of
Doctor of Philosophy

Date

Chair of the Thesis Examination Board

Abstract

The nickel-based Alloy 600, also known as Inconel 600 has been found to be susceptible to stress corrosion cracking (SCC) in high temperature aqueous environments. Despite extensive research, the mechanisms by which this process occurs remain in question.

It is known that SCC results from the simultaneous effects of a chemically corrosive environment and a tensile stress. Many studies have been conducted on the microscopic chemical changes associated with SCC. There have been fewer studies of the microscopic stress/strain process. The main objective of this thesis is to use the new x-ray based diffraction technique – polychromatic x-ray microdiffraction (PXM) to study changes of the microstructure and elastic/plastic deformation introduced by SCC in Alloy 600, thus leading us to an understanding of the mechanisms of SCC.

More traditional techniques such as neutron diffraction and electron backscatter diffraction (EBSD) were also used in this thesis. Neutron diffraction measures information down to a depth resolution of a few mm, while EBSD is considered to be a surface measurement (1-2 μm). By comparison, PXM examines strain to a depth of several grains in alloy 600 ($\sim 60 \mu\text{m}$), which is particularly appropriate for detecting information from intergranular interactions under typical stress corrosion conditions. The capability of measuring strain directions (compressive or tensile) is another advantage of PXM in SCC study. Besides the microstructure and elastic strain information, the local plastic deformation can also be examined by assessing the streaking/splitting of the Laue spots and modeling of the Laue diffraction images.

In this thesis, PXM was first validated by comparing the data to those from neutron diffraction and EBSD for a simple case – uniaxially stressed tensile specimens. Then studies were carried out on C-ring samples before and after cracked by SCC. Torsional stressing of an Alloy 600 C-ring specimen results in significant tensile strain in the stress axis direction. Intergranular SCC (IGSCC) was observed in Alloy 600 C-ring specimens electrochemically corroded in a high temperature caustic solution. Tensile strains with respect to the stress axis and plastic strain could be identified in regions ahead of the crack tip. These regions

correspond to triple junctions where crack arrest occurs and re-initiation requires a buildup of the strains.

Keywords

Alloy 600, Polychromatic X-ray Microdiffraction (PXM), neutron diffraction, Electron Backscatter Diffraction (EBSD), Stress Corrosion Cracking (SCC), deviatoric strain, plastic deformation, dislocation

Co-Authorship Statement

This thesis contains material from previously published manuscripts, progress reports, as well as submitted manuscript that is under reviewing, which were prepared by Jing Chao and co-authored, performed, or edited by others mentioned below. Jing Chao's research Ph.D. supervisor Prof. N. Stewart McIntyre is a co-author on all materials presented in this thesis. Prof. N. Stewart McIntyre played a major role in the editing and revision of the materials presented in this thesis. Dr. Marina L. Suominen Fuller is also a co-author on the materials presented in Chapter 3-7. Dr. Marina L. Suominen Fuller was responsible for training Jing Chao to use the PXM processing software (ThreeDimX-rayMicroscopy) and helping Jing Chao with all the data analysis and interpretation.

The uniaxial tensile test and the calculation of the strain from the stress-strain curve for bar samples in Chapter 3 and 4 was done by Prof. Robert Klassen in the Department of Mechanical Engineering at the University of Western Ontario. Neutron diffraction measurements were carried out by Dr. Alison Mark from Prof. Richard Holt's group at Queen's University for the bar samples in Chapter 3. EBSD measurements on bar samples in Chapter 3 were performed by Kinetrics, while the EBSD data on the C-ring sample in Chapter 7 was collected by Mr. Jagan Athanu from Prof. Roger Newman's group at the University of Toronto. Dr. Anatolie Carcea also from Prof. Roger Newman's group was responsible for performing all the SCC test for the C-ring samples used in Chapter 6 and 7.

Dr. Rozaliya Barabash from Oak Ridge National Laboratory did the modeling of the dislocations in Chapter 3. PXM data on the mid-bar tensile sample in Chapter 3 and 4 was collected by Jing Chao at APS with the help of Dr. Marina Fuller and beamline scientist – Dr. Wenjun Liu. All the rest PXM data were collected by Dr. Marina Fuller, as Jing Chao was unable to get the US visa in time. The PXM data for C-ring samples presented in Chapter 5-7 were collected at ALS with the help of Dr. Martin Kunz and Dr. Nobumichi Tamura.

The sample preparation and part of the SEM imaging were carried out in Surface Science Western with the help of Dr. Sridhar Ramamurthy. The FIB work was done by Dr. Todd Simpson in Western Nanofabrication Laboratory. Jinhui Qin and Nathaniel Sherry were responsible for helping Jing Chao with the use of FOXMAS and Strainviewer.

Acknowledgments

This thesis is a result of not only my own efforts but also many others' supports and help throughout my Ph.D study. It is my great pleasure to acknowledge them here.

First and foremost, I would like to express my deepest gratitude to my supervisor, Prof. N. Stewart McIntyre. Without his full support and careful guidance, it is an impossible task for me to finish my Ph.D study. His enthusiasm and love of the research is what I will always admire. His insight idea and brilliant advice always inspired me and gave me the confidence to carry out the research work and face all the challenges. I'd especially like to take this opportunity to thank for his kindness and patience during my pregnancy and the difficult but memorable writing times.

Next, I would like to thank all the former members in our research group, Dr. Marina Suominen Fuller, Dr. Brad Payne and Mr. Mike Edwards for their inspiration in research, friendship and fun. Special thanks go to Dr. Marina Suominen Fuller. Dr. Marina Suominen Fuller played an important role in my study. Her valuable comments and suggestions have led to significant achievements in this thesis work. I am also grateful for her help and advices on daily life issues. I would also like to extend my thanks to my friends, in particular Zhaohui Dong, Lijia Liu, Yanyu Xiao and Zhongying Mi. I'm lucky to have them with me during this long journey. My life would not be the same without them.

I also want to thank our collaborators for their input: Prof. Rob Klassen's group in the Department of Mechanical Engineering at the University of Western Ontario, Prof. Richard Holt's group at Queen's University, Prof. Roger Newman's group at University of Toronto and our industry collaborator - Kinetrics.

The following people are acknowledged for their technical expertise and guidance: Dr. Sridhar Ramamurthy, Mr. Ross Davidson, Mr. Brad Kobe and Mr. Gary Good from Surface Science Western for their help with all the research work done at SSW; Dr. Todd Simpson and Mr. Tim Goldhawk from the Western Nanofabrication Facility for SEM, EDX and FIB help; Mr. Brian Dalrymple and Mr. Frank Van Sas from the Western Physics and Astronomy machine shop for their help with machining; Beamline scientists Dr. Wenjun Liu

from the Advanced Photon Source, Dr. Nobumichi Tamura from the Advanced Light Source and Dr. Renfei Feng from Canadian Light Source; Dr. Jinhui Qin, Mr. Nathaniel Sherry and Dr. Yuzhen Xie from Computer Science at University of Western Ontario for their support in software. Mr. Alex Brennenstuhl and Mr. Ted Lehocky of Ontario Power Generation (OPG) were acknowledged for their discussion and suggestions at the early stage of this project. A special thank goes to Dr. Rozaliya Barabash from Oak Ridge National Laboratory for the modeling of the Laue image.

Finally, I would like to thank my parents for their unconditional love and endless support. Especially my mom, without her tirelessly and carefully taking care of my little Jennie, I would never be where I am now. Thanks, mom. I am also grateful to my husband Qing. His full support, love and understanding always encourage me and give me confidence. Of course, Jennie, my little girl, thank you for being a healthy and happy baby. You are such a gift. Whenever I got frustrated or tired from writing, I would feel so peaceful and happy immediately after holding you in my arm or even looking at your sleeping face. Mom loves you, Jennie.

Table of Contents

CERTIFICATE OF EXAMINATION	ii
Abstract	iii
Co-Authorship Statement.....	v
Acknowledgments.....	vi
List of Tables	xii
List of Figures	xiv
List of Appendices	xx
Symbols and Acronyms	xxi
Chapter 1	1
1. Introduction	1
1.1 Basic Concepts	4
1.1.1 Deformation in Polycrystalline Material	4
1.1.2 Grain Boundaries	8
1.2 SCC Studies of Alloy 600.....	10
1.2.1 Factors for SCC behavior in Alloy 600	10
1.2.2 Mechanisms	12
1.2.3 Remedies.....	13
1.3 Diffraction Techniques for Microscopic Deformation Studies.....	14
1.3.1 Polychromatic X-ray Microdiffraction (PXM).....	15
1.3.2 Electron Backscatter Diffraction (EBSD).....	20
1.3.3 Neutron Diffraction.....	22
1.4 Objectives and Arrangement of the Thesis	22
Chapter 2.....	24
2. Experimental Details.....	24
2.1 Specimen Description	24

2.2 Specimen Preparation Techniques	24
2.2.1 Uniaxial Tensile Test	25
2.2.2 Making C-Ring Samples.....	26
2.2.3 SCC Test	27
2.2.4 Sample Surface Treatment Techniques	27
2.3 Polychromatic X-ray Microdiffraction (PXM)	30
2.3.1 PXM Beamlines.....	30
2.3.3 Data Analysis Software.....	31
2.4 Electron Backscatter Diffraction (EBSD).....	32
2.5 Neutron Diffraction.....	33
2.6 Other Instruments.....	34
Chapter 3.....	35
3. Comparisons of Polychromatic X-ray Microdiffraction (PXM) with Neutron Diffraction and Electron Backscatter Diffraction (EBSD)	35
3.1 Brief Review of Experimental (Samples & Techniques).....	35
3.2 Results and Discussion.....	36
3.2.1 PXM Elastic Strain Results.....	36
3.2.2 2D PXM Comparison with Neutron Diffraction	41
3.2.3 3D PXM Comparison with Neutron Diffraction	44
3.2.4 PXM Comparison with EBSD.....	46
3.3 Summary	49
Chapter 4.....	51
4. PXM Results from Tensile Bar Samples	51
4.1 Brief Review of Experimental (Samples & Techniques).....	51
4.2 Results and Discussions	51
4.2.1 Elastic Strain Study.....	51

4.2.2 Plastic Deformation Study	52
4.3 Summary	60
Chapter 5	62
5. PXM Study of Unstressed and Stressed C-rings.....	62
5.1 Brief Review of Experimental (Samples & Techniques).....	62
5.2 Results and Discussions	62
5.2.1 Elastic Strain Study.....	63
5.2.2 Study of Pole Figures.....	66
5.2.3 Peak Study	67
5.3 Summary	70
Chapter 6.....	72
6. PXM Study of 6h and 18h SCC-cracked C-rings	72
6.1 Brief Review of Experimental (Samples & Techniques).....	72
6.2 Results and Discussions	73
6.2.1 Elastic Strain	73
6.2.2 Grain Boundary Study	78
6.2.3 Schmid Factor	82
6.2.4 Local Mis-orientation (Plastic Strain) Study	83
6.2.5 Ellipticity.....	85
6.2.6 Slip System Modeling.....	87
6.3 Summary	88
Chapter 7.....	90
7. PXM and EBSD Study of 24h SCC-cracked C-ring.....	90
7.1 Brief Review of Experimental (Samples & Techniques).....	90
7.2 Results and Discussions	91
7.2.1 SEM Characterization.....	91

7.2.2 PXM Measurement	94
7.2.3 EBSD Measurement.....	97
7.3 Summary	98
Chapter 8.....	100
8. Conclusions and Future Work.....	100
8.1 Conclusions	100
8.1.1 Evaluation of PXM	100
8.1.2 SCC Study.....	102
8.2.3 Use of FOXMAS	104
8.2 Value and Implication	104
8.3 Future Work	105
References	108
Appendix I Angle calculation from PXM data for Chapter 3.....	114
Appendix II Calculation of Schmid factor from Laue data	116
Appendix III Copyright permissions	120
Curriculum Vitae	137

List of Tables

Table 1.1 Alloys/environment systems exhibiting stress corrosion cracking (SCC). Excerpted from Table 3.4 in [3].....	2
Table 1.2 Nominal chemical composition and selected properties of nickel alloys. Excerpted from Table 29.1 in [11].....	3
Table 1.3 12 slip systems operating in fcc crystals.....	7
Table 1.4 Comparison of different non-destructive strain detection techniques	14
Table 2.1 Chemical composition of bar samples and C-ring samples.....	24
Table 2.2 Summary of treatments of samples studied in this project	25
Table 3.1 Average deviatoric strain (elastic strain) for the PXM scanned area of control, end-bar and mid-bar strained samples.	41
Table 3.2 Strain measurements for the end-bar sample using neutron diffraction.	42
Table 3.3 Averaged strain values from the whole grain for the 5 selected grains in the 2D PXM map.....	43
Table 3.4 Calculated orientations for Grains 1-5 of the end-bar sample from 2D PXM data to RD, TD, ND.....	43
Table 3.5 Strain from the 5 selected regions from 2D PXM and neutron results for the end-bar sample.	43
Table 3.6 Calculated orientations for Grains 1-5 from 3D PXM data to RD, TD, ND system.	45
Table 3.7 Strain from Grains 1-5 from the 3D PXM and neutron results for the end-bar sample.	45

Table 6.1 Average strain values calculated over the detected areas for all four C-ring samples*.....	76
Table 6.2 Schmid factors calculated for the grains around cracks of both 6h and 18h SCC cracked C-ring samples. Refer to Figure 6.5 for the grain number locations. Note that only the maximum value of Schmid factors calculated from the 12 slip systems was reported for the grain.	83

List of Figures

- Figure 1.1 Model of simple cubic lattice with (a) edge dislocation and (b) screw dislocation. Burgers vector and dislocation line are also shown. Modified from Figure 1.18 in [14]. 5
- Figure 1.2 Sketch of (a) Incidental dislocation boundary and (b) geometrically necessary boundary. Notice that the mis-orientation angle between cells at GNBs are usually bigger than those at IDBs. Adopted from Figure 2 in [15]. 6
- Figure 1.3 Illustration of the geometry of slip in a cylinder. Note that $\alpha + \beta \neq 90^\circ$ in general. . 8
- Figure 1.4 An example of coincidence plot of two lattices. It is a $\Sigma 5$ boundary, as every 1 in 5 lattice points coincide with each other. Adopted from Figure 11.1 in [21]. 10
- Figure 1.5 Illustrations of (a) the storage ring, (b) bending magnet, (c) wiggler and (d) undulator. Differences in the size of the photon beam achieved from the three magnetic elements are also shown. Adopted from [56]. 16
- Figure 1.6 General experimental arrangement of PXM. Modified from [65]. 18
- Figure 1.7 Schematic diagram of electron backscatter diffraction system in SEM. 21
- Figure 2.1 (a) Layout for the tensile test. The engineering strain was calculated to be 1%. (b) True stress-true strain curve for the Alloy 600 tensile test. E is the Young's modulus. The residual plastic strain is calculated to be 0.5% shown in the figure. 26
- Figure 2.2 Optical images of a C-ring: (a) before and (b) after stressing by bolt tightening to achieve a nominal 2% strain. Green boxes at the sample apex indicate the analysis area. 27
- Figure 2.3 SEM image of the FIB polished area at the flat end face. Cutting lines and Pt lines were made on both sides of the polished area, to help find the area during Laue diffraction. 29
- Figure 2.4 The photograph shows the sample orientation with respect to the coordinate systems of: (a) PXM measurements and (b) neutron diffraction measurements. 33
- Figure 3.1 Orientation map and deviatoric strain component maps of the control sample from 2D PXM. The field of the diffraction patterns comprises an area of $180 \times 180 \mu\text{m}^2$. The color

legend for OM is on the top of the OM map, while the color legend with a scale of -5 to 5 ($\times 10^{-3}$) for all strain maps is shown at the right corner.	37
Figure 3.2 Orientation map and deviatoric strain component maps of the end-bar tensile sample from 2D PXM. The field of the diffraction patterns comprises an area of $180 \times 160 \mu\text{m}^2$. The color legends for OM and strain maps are the same as in Figure 3.1. The blue line across grain 2 in the OM indicates the position for the 3D PXM scan. The numbers in OM indicate 5 grains for later comparison with neutron diffraction.	38
Figure 3.3 Orientation map (OM) and strain maps of 3D PXM scan from the end-bar sample. Refer to Figure 3.1 for the color legend of OM and strain maps. The numbers in OM indicate 5 selected grains for later comparison with neutron diffraction.	39
Figure 3.4 Orientation map and deviatoric strain component maps of the mid-bar tensile sample from 2D PXM. The field of the diffraction patterns comprises an area of $200 \times 200 \mu\text{m}^2$. The color legends for the OM and strain maps are the same as in Figure 3.1.	40
Figure 3.5 Comparison of (a) EBSD and (b) PXM orientation maps for the mid-bar sample. The PXM results are plotted for two different directions. The pole figure grain orientation is denoted by color and the orientation can be determined from the color legend.....	48
Figure 3.6 Comparison of PXM and EBSD composite strains for the mid-bar sample.	48
Figure 3.7 Laue patterns for four different pixels from the same grain within the map for the mid-bar sample: (a) pixel from an area of high elastic strain; (b) pixel from an area of low elastic strain; (c) pixel close to the grain boundary; (d) pixel on the grain boundary.	49
Figure 4.1 Orientation map and von Mises strain map for the end-bar sample. Angular misorientations are shown across some of the grain boundaries.....	52
Figure 4.2 Case 1: A $\Sigma 13\text{b}$ GB from the end-bar sample. Diffraction spots are streaked in Grain 1 indicating plastic strain, particularly near the GB where the presence of dislocation walls is indicated by the splitting. Grain 2, although having higher elastic strain, shows little evidence of plastic strain.....	53

Figure 4.3 Case 2: A 60 degree mis-orientation ($\Sigma 3$) from the 2D PXM data of the end-bar sample. Streaked diffraction spots are found close to the twin boundary on either side, but not near the grain centres.	54
Figure 4.4 Case 3: A 60 degree mis-orientation ($\Sigma 3$). Dislocations are found on both sides of the twin boundary.	55
Figure 4.5 Case 4: A 12 degree GB. Diffraction spots from the two grains, mid -grain and near the grain boundary are presented. Dislocations are found on both sides of the boundary, while cell walls are only evident in Grain 8.	56
Figure 4.6 Case 5: A boundary whose mis-orientation is not able to be determined. Diffraction spots from the two grains, mid-grain and near the grain boundary are presented. Grain 10 shows significantly more elongation and splitting, indicating the formation of significant cell walls.	57
Figure 4.7 Comparison between the experimental pattern and simulated pattern for an area in the 2D map shown in Figure 4.6.	58
Figure 4.8 In-depth orientation map with diffraction patterns from different sample depths.	60
Figure 5.1 (a) Schematic of the analysis area, tensile stress direction, sample positioning in the beamline and the sample coordinate system; Laue XRD orientation maps (OM) and von Mises equivalent strain maps (VM) for the C-ring sample: (b) before and (c) after stress. ...	63
Figure 5.2 The deviatoric strain component maps for the C-ring samples: (a) before and (b) after stress. The same color scale was used for both samples, as shown at the top of the figure.	65
Figure 5.3 The pole figures for the C-ring samples: (a) before and (b) after stress.	65
Figure 5.4 The zoomed-in pole figures for the C-ring sample: (a) before and (b) after stress.	66
Figure 5.5 Comparison of the peak shape from the same locations of the (a) unstressed C-ring and (b) stressed C-ring samples. Panels a1, a2, a3 show selected peaks from each of these	

locations in the unstressed C-ring, while panels b1, b2, b3 represent peak patterns from the corresponding locations in the stressed C-ring. The numbers on the peak images are the Miller indices of the chosen peak. 68

Figure 5.6 Laue XRD images for the C-ring sample from a location denoted by the blue triangle in the OMs shown in Figure 5.5: (a) before and (b) after stress..... 69

Figure 5.7 Laue XRD images for the C-ring sample near the sample outer surface, denoted by the blue star in the OMs shown in Figure 5.5: (a) before and (b) after stress..... 69

Figure 6.1 SEM images from the cross sectional surface of: (a) the 6h cracked C ring and (b) 18h cracked C ring samples showing the area covering cracks after FIB polishing. SEM images with higher magnification of the cracks are also shown here. Note the line within the FIB polished area and tiny scratches around both crack tips; these are defects from FIB polishing..... 73

Figure 6.2 (a) Schematic of the analysis area, sample positioning in the beamline and the sample coordinate system; (b) Orientation and strain maps for the scanned area from the 6h SCC-cracked C-ring sample. The color legend for the deviatoric strain maps is shown above the maps, with a scale of -7 to $+7 (\times 10^{-3})$. A unique color legend was used for the VM strain map, shown below the VM map. The dashed lines in the maps indicate the sample edges, while the black/white filled lines show the locus of the crack by overlaying the SEM images. 74

Figure 6.3 (a) Schematic of the analysis area, sample positioning in the beamline and the sample coordinate system; (b) Orientation and strain maps for the scanned area from the 18h SCC-cracked C-ring sample. Refer to Figure 6.2 for the color legend for strain maps. The dashed lines in the maps indicate the sample edges, while the black/white filled lines show the locus of the crack by overlaying the SEM images..... 75

Figure 6.4 OMs, VM map and the y principal deviatoric strain ϵ_{yy} map with the mis-orientation angles shown between grains around cracks for the (a) 6h and (b) 18h SCC cracked C-ring samples. Enlarged maps from the square in the ϵ_{yy} map are shown at the top

right corner of 6h and 18h results. The white arrow 'c' in 6h shows a tensile area which indicates a potential crack initiation site..... 77

Figure 6.5 Peak patterns collected from adjacent grains around the cracks formed on the (a) 6h and (b) 18h SCC cracked C-ring samples. For each sample, peaks are shown from four locations along the colored arrows crossing two adjacent grains. For (a1) G1-G2, peaks from mid-grain G1 to mid-grain G2 following the arrow are displayed. Peak (i) is from the mid-grain G1 and peak (ii) is from the G1 side of the grain boundary, while peak (iii) is from the G2 side of the grain boundary and peak (iv) is from the mid-grain G2. The peaks in all the following examples are arranged similarly to that in (a1) G1-G2. The numbers on images of the peaks are the Miller indices of the chosen reflection..... 81

Figure 6.6 (a) Magnification of the mis-orientation map in the region of the crack tip for the 18h sample; (b-e) the zoomed-in pole figures for 4 individual grains surrounding the crack tip along with point to point orientations within each of these four grains..... 84

Figure 6.7 (a) Magnification of the mis-orientation map in the region of the crack tip for the 6h sample; (b-c) the zoomed-in pole figures for 2 individual grains surrounding the crack tip along with point to point orientations within each of these two grains. 84

Figure 6.8 [001] Orientation map (a), local misorientation map (b) and ellipticity map (c) from the selected region of the 18h cracked C-ring sample. Color legends are located below the corresponding maps. 86

Figure 6.9 (a) Magnification of the ellipticity map in Figure 6.8 in the region of the crack tip; (b-d) show the shapes and inclinations of diffraction spots from different regions indicated in (a). 87

Figure 6.10 The Laue diffraction image from the interior of Grain 5 in the 18h sample. (a) experimental; (b) simulated pattern using XMAS for a single screw dislocation $(-1-11)\langle -110 \rangle$. Three indexed peaks were enlarged under the image..... 88

Figure 7.1 SEM image of the cracks found around the apex of the flat end surface of the 24h C-ring. Site A is a crack with length of $\sim 200 \mu\text{m}$, while site B is a crack with length of ~ 500

μm. More cracks were observed within a certain distance from the apex besides the two shown.	91
Figure 7.2 (a) SEM image of the whole crack and (b-c) enlarged SEM images from locations (i) and (ii) as outlined by red boxes in (a). Yellow circle on the image in (a) indicates an area with isolated crack segment.	92
Figure 7.3 (a) SEM image of the crack area studied by PXM. The sample coordinate system is also shown on the image. The y direction is the main stress axis. (b) x-ray absorption map of the above region. A color scale with green being the lowest to red the highest absorption intensity is used. The green trail shown indicates the location of the crack path. (c) [001] orientation map and (d) the three principal deviatoric strain maps of the area covering crack from the PXM scan. A scale of -5 to $5 (\times 10^{-3})$ with color changing from blue (compressive) to red (tensile) is used.	93
Figure 7.4 Laue diffraction images from the black areas close to the sample edge and an example of an indexed pattern further into the bulk.	95
Figure 7.5 (a) Index quality map which shows number of indexed diffraction spots for each Laue pattern; (b) local mis-orientation map, an angular scale of 0-2 degrees was used; (c) von Mises strain map and (d) a plot of the average von Mises strain changing with the distance from the C-ring OD.	96
Figure 7.6 (a) Orientation maps of the large crack using EBSD and PXM. The triangle color scale for OM in EBSD is also shown; (b) local mis-orientation maps of the crack area using EBSD and PXM. The same scale 0 to 2 degrees was used. The red boxes outline the portion from which the EBSD scan was taken.	98
Figure 8.1 (a) SEM image of the bar sample surface after a 12h SCC test; (b-e) OM, index quality map, local mis-orientation map and ellipticity map of the area shown in the SEM image obtained from PXM.	107
Figure A.1 Illustration of the geometry of slip in a cylinder. Note that $\alpha + \beta \neq 90^\circ$ in general. Adopted from Chapter 1 (Figure 1.3).	116

List of Appendices

Appendix I Angle calculation from PXM data for Chapter 3.....	114
Appendix II Calculation of Schmid factor from Laue data	116
Appendix III Copyright permissions	120

Symbols and Acronyms

Symbols

\bar{b}	Burgers vector
τ	dislocation line
τ_c	shear stress
σ	stress
σ_y	yield stress
m	Schmid factor
α	angle between loading direction and the slip plane normal
β	angle between loading direction and the slip direction
$\Delta\theta$	minimum rotation angle between two adjoining grains
Σ	the degree of coincidence between two adjoining grains
ν_m	the maximum angular deviation of a coincidence site lattice grain boundary
ν_0	the angular limit for low-angle grain boundary
λ	wavelength
d	lattice spacing
θ	incident angle of diffraction
ψ	opening angle of the synchrotron radiation
E	electron energy
ε	strain
hkl	Miller indices of diffraction spots
$\mu\varepsilon$	microstrain, a strain unit at the level of 10^{-6}

Acronyms

SCC	stress corrosion cracking
IGSCC	intergranular stress corrosion cracking

TGSCC	transgranular stress corrosion cracking
PXM	polychromatic x-ray microdiffraction
EBSD	electron backscatter diffraction
OPG	Ontario Power Generation
NACE	National Association of Corrosion Engineers
SG	steam generator
GND	geometrically necessary dislocation
SSD	statistically stored dislocation
IDB	incidental dislocation boundary
GNB	geometrically necessary boundary
fcc	face-centered cubic
bcc	body-centered cubic
hcp	hexagonal closed packed
GB	grain boundary
CSL	coincidence site lattice
CW	cold work
KB	Kirkpatrick-Baez
CCD	charge coupled device
DAXM	differential-aperture x-ray microscopy
SEM	scanning electron microscopy
OIM	orientation imaging microscopy
EBSP	electron backscatter diffraction pattern
COG	CANDU Owners Group
AECL	Atomic Energy of Canada Limited
ASTM	American Society for Testing and Materials
OD	outside diameter

RE	reference electrode
SSW	Surface Science Western
SCE	saturated calomel electrode
FIB	focused ion beam
μ XRF	x-ray microfluorescence spectroscopy
APS	Advanced Photon Source
ANL	Argonne National Laboratory
ALS	Advanced Light Source
LBNL	Lawrence Berkeley National Laboratory
VESPERS	very powerful elemental and structural probe employing radiation from a synchrotron
CLS	Canadian Light Source
XMAS	x-ray microdiffraction analysis software
ORNL	Oak Ridge National Laboratory
FOXMAS	fast online x-ray microanalysis software
CNBC	Canadian Neutron Beam Center
CRL	Chalk River Laboratories
RD	rolling direction
TD	transverse direction
ND	normal direction
EDX	energy dispersive x-ray analysis
VM	von Mises
OM	orientation map

Chapter 1

1. Introduction

Metals are important structural materials because of their strength, fracture toughness, and tolerance of high temperature; however, metals are subject to chemical corrosion. Most people are familiar with corrosion in one form or another, such as the rusting of a galvanized wire fence or the degradation of a steel bridge. Corrosion can be both costly and dangerous. It is not simply a loss of metal, but also a waste of energy, water, and human effort that was used to reproduce and fabricate the structures. According to the cost study by NACE (the National Association of Corrosion Engineers), the total direct cost of corrosion in US was \$276 billion in 1998 [1], which did not even include the large indirect corrosion cost from the lost productivity because of failure, outages, etc. In the case of failure of bridges or other structures due to corrosion, human injury and/or loss of life usually are involved.

So what is corrosion? It is the deterioration of a material, usually a metal that results from a reaction with its environment according to a NACE definition [2]. Generally speaking, it is a process of a chemical element returning to its most stable thermodynamic state. This usually means a formation of oxide or sulfide from which the metal originally started when they were taken from the earth. These processes can usually be modeled as electrochemical reactions. The metal that serves as anode will usually undergo corrosion. However, the cathodic reaction is equally important as the corrosion process can only proceed when anodic and cathodic reactions happen simultaneously and at the same rate. Corrosion can appear in different forms. The most common form is the uniform or general attack that proceeds over a large area of the material. Pitting, crevice corrosion and intergranular corrosion are forms of localized corrosion, which only occur at particular sites of the exposed material. They may sometimes turn into stress corrosion cracking (SCC).

SCC is a particular form of corrosion for metals, which involves the initiation and growth of cracks due to a corrosive chemical reaction and a mechanical stress. Such

cracks can be intergranular (IGSCC, along the grain boundaries of a metal) or transgranular (TGSCC, through the grain) or a mixture of both. These processes can affect the integrity and reliability of the metal. SCC usually occurs without any visible deformation and is difficult to be detected at its early stage.

Table 1.1 Alloys/environment systems exhibiting stress corrosion cracking (SCC). Excerpted from Table 3.4 in [3].

Alloys	Environment
Carbon steel	Hot nitrate, hydroxide, and carbonate/bicarbonate solutions
High-strength steels	Aqueous electrolytes, particularly when containing H ₂ S
Austenitic stainless steels	Hot, concentrated chloride solutions; chloride-contaminated steam
Nickel alloys	High-purity steam; caustic alkaline solutions; high temperature chloride solutions; hydrofluoric acid; acidic fluoride solutions
α -brass	Ammoniacal solutions
Aluminum alloys	Aqueous Cl ⁻ , Br ⁻ , and I ⁻ solutions
Titanium alloys	Aqueous Cl ⁻ , Br ⁻ , and I ⁻ solutions; organic liquids; N ₂ O ₄
Magnesium alloys	Aqueous Cl ⁻ solutions
Zirconium alloys	Aqueous Cl ⁻ solutions; organic liquids; I ₂ at 350°C

SCC can be found in various metal alloys, as shown in Table 1.1. It was towards the end of the 19th century that SCC was first reported as a widespread problem when it appeared in brass condenser tubing in electric power generators [4]. One cause of SCC in steels was found to be a local high concentration of free alkali and elevated temperature that resulted in “caustic cracking”. Later, SCC was observed in aluminum alloys, magnesium alloys and other alloys, including those of nickel.

High content nickel alloys possess remarkable mechanical strength and provide outstanding resistance to specific chemicals. Nickel-based alloy 600 (Alloy 600) is a kind of solid solution with major element composition Ni-16Cr-9Fe, and minor alloying additions such as Cu, Si, Mn and C. It has been widely used as the primary steam generator (SG) tubing material and other safety-critical components such as reactor vessel components and seals in nuclear reactors. However, SG tubes made from Alloy 600 have proven to be highly susceptible to SCC, which is in fact the single most important reason that Alloy 600 SG tubes are replaced. Alloy 690 and Alloy 800 both from the Ni-Cr-Fe family are used to replace Alloy 600 SG tubes in US, Canada and Europe, respectively. In Table 1.2, the chemical composition and selected mechanical properties of the three alloys are shown. The tensile strength is the highest stress that the material can sustain, which usually is calculated by dividing the maximum load by the

original cross-sectional area. The yield strength is the stress at which the material starts to deform plastically. This value can often be obtained from the stress-strain curve. The elongation is defined as the gage length change over the original gage length of the specimen in a tensile test. These are three important mechanical properties to a material and they are very similar for the three alloys. Though there are no reports of SCC failure in Alloy 690 and 800 SG tubes under service, there are reasons to believe that Alloy 690 and Alloy 800 may also undergo SCC. There are studies showing possible SCC in Alloy 690 and 800 in some circumstances [5-10]. SG tubes essentially act as heat transporter between primary and secondary coolant. Leaking of the tubes makes the heat transport unreliable, which means that a shutdown of the nuclear station may be necessary for repair or exchange of the tubes. In other words, great economic and energy loss would be result from unexpected failure of these tubes. Therefore, understanding the mechanism of SCC is critical to reducing the unexpected failure.

Table 1.2 Nominal chemical composition and selected properties of nickel alloys. Excerpted from Table 29.1 in [11].

	Composition, wt%	Tensile strength, MPa	Yield strength, MPa	Elongation in 50mm, %
Alloy600	Ni-16Cr-9Fe	655	310	40
Alloy690	Ni-29Cr-9Fe	725	348	41
Alloy800	Ni-21Cr-39.5Fe	600	295	44

Stress, one of the main contributors to SCC, becomes our focus in this study. Unlike the applied stress, local residual stress is usually hard to predict and/or detect; it can increase the total stress to a value as high as or even above the yield stress. In this work, we have focused on the study of changes of the microstructure and mesoscopic (0.1 - 100 μm) elastic/plastic deformation of Alloy 600 that is introduced either by applied stress or by SCC, thereby leading us to a better understanding of the mechanism of the SCC. Dislocation movement and possible acting slip systems are also discussed. The main technique used was synchrotron-based polychromatic x-ray microdiffraction (PXM). Neutron diffraction and electron backscatter diffraction (EBSD) measurements were also performed on some of the samples.

1.1 Basic Concepts

1.1.1 Deformation in Polycrystalline Material

The imposition of a small stress on a polycrystalline alloy will first produce residual elastic strains whose magnitude and directions are grain orientation dependent. As the yield point is approached, plasticity in the material is introduced through the creation of crystallographic dislocations. These accommodate slip and lattice rotation [12], and provide the bases for plastic flow in a polycrystalline system. They form under high strain gradients and are thus often influenced by the proximity of a grain boundary [13] where they can form cell-wall structures.

1. Residual stress and residual strain

Force applied to a single crystal material can cause elastic or plastic deformation. The deformation is considered to be elastic if the material is completely restored after the force is removed, otherwise, it is a plastic deformation. However, in polycrystalline material, the deformations become more complex. The elastic deformation may not completely be relaxed due to the inhomogeneous deformation within the system, associated with local incompatibility (e.g., volume change, thermal dilatation, grain boundaries etc.) and these result in so called "residual elastic deformation" or "residual elastic stress/strain". By definition, residual stresses are stresses that remain in the material after the original cause of stresses (external force, heat gradient) has been removed. The residual strain is the strain induced by plastic deformation and/or from residual elastic deformation. Residual stress/strain is the combined result of residual elastic and plastic deformation. In general, residual stress/strain can be introduced in a material during manufacture and/or use by such mechanical forming processes as bending, swaging, welding or annealing.

The presence of residual stress/strain in materials and components can heavily influence their behavior. It can be beneficial or detrimental. For example, the residual tensile stress/strain at a material surface is believed to be one of the most important factors that causes material cracking. However, unlike applied stress, residual

stress/strain is difficult to predict. The tensile and compressive residual stress/strain counteract one another to keep stress in balance macroscopically, however, they can be dramatically different from point to point. Methods using diffraction techniques have turned out to be effective in determining residual stress/strain. Other methods include ultrasonics and destructive measurements.

2. Dislocations

A dislocation is a linear defect in the crystalline material around which the atoms are misaligned in a crystal structure. The existence of dislocations usually strongly affects many properties of materials. Plastic deformation of metals is produced by forming (heating, bending, striking or swaging) resulting in creation and storage of dislocations.

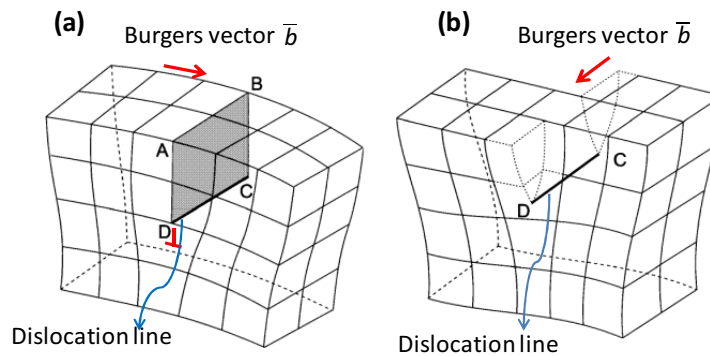


Figure 1.1 Model of simple cubic lattice with (a) edge dislocation and (b) screw dislocation. Burgers vector and dislocation line are also shown. Modified from Figure 1.18 in [14].

There are two fundamental types of dislocations: edge and screw dislocations, as shown in Figure 1.1. Edge dislocations are defects where extra half-plane of atoms are introduced in crystal structure. There are positive and negative edge dislocations depending on where the extra half plane located in the crystal structure (top – positive, bottom - negative). Screw dislocations are harder to visualize, but usually can be thought as the result of shear stress: the upper front portion of the crystal shifted one atomic distance towards the right relative to the bottom portion in Figure 1.1b. Screw dislocations can also be positive or negative depending on if the screw advancing along the dislocation line is right-handed or left-handed. In general, the dislocations with different signs will attract and cancel out each other, while the ones with same signs will

be repulsive to each other. In Figure 1.1, Burgers vector and dislocation lines are also displayed. The Burgers vector \bar{b} is a measure of the magnitude and the direction of the lattice distortion in crystal generated by dislocations. It is usually defined by means of a circuit containing dislocations. The vector required to complete the closed loop is defined as the Burgers vector. Burgers vector is found to be perpendicular to the dislocation line for edge dislocations, while it is parallel to the dislocation line for screw dislocations.

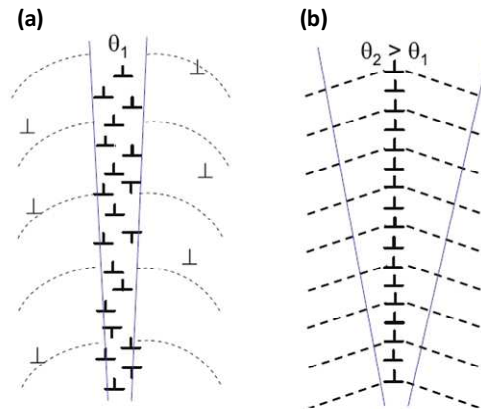


Figure 1.2 Sketch of (a) Incidental dislocation boundary and (b) geometrically necessary boundary. Notice that the mis-orientation angle between cells at GNBs are usually bigger than those at IDBs. Adopted from Figure 2 in [15].

Dislocations introduced during homogenous deformation at very low strains, generally are stored in very loose arrangement that do not cause significant rotation of the lattice. However, when inhomogeneous deformation occurs in metals, there will be an accumulation of local "excess dislocations" with the same sign. These are generally referred to as "geometrically necessary" dislocations (GNDs). They are result of the incompatibility of plastic deformation and the local curvature of the corresponding crystal lattice. In other words, GNDs arise from non-uniform deformation of crystals to maintain the continuity of the crystal lattice. Dislocations make the lattice distorted around them and create stress/strain field (strain energy). To minimize the energy within materials, the dislocations tend to move together and form cell-walls/boundaries when enough strain is provided, thus leaving some areas with few dislocations - the cell interior, which are relatively strain free. The walls/boundaries formed can usually be classified into two types: incidental dislocation boundaries (IDBs) and geometrically

necessary boundaries (GNBs), shown in Figure 1.2. IDBs are formed by random trapping of dislocations with any sign, while GNBs form between regions of different strain patterns to accommodate the accompanying differences in lattice rotation (usually with dislocations of one sign). For large strains, the lattice at each side of the GNBs can rotate very differently ($>15^\circ$), which becomes equivalent to ordinary grain boundaries.

3. Slip

Slip is the process describing the motion of the dislocations. The crystallographic plane that the dislocation line transverses is the slip plane. The direction that the dislocation moves is the slip direction. The slip plane and slip direction have preferential crystallographic forms in each crystal system. Slip planes are normally planes with the highest density of atoms, while the slip directions are the most closely packed directions within the slip plane. A slip plane and a slip direction constitute a so-called slip system. For instance, in face-centered cubic (fcc) crystals, the four $\{111\}$ planes are the most dense planes and the three $\langle 110 \rangle$ directions within the $\{111\}$ planes are the most closely packed directions. In other words, there are 12 slip systems for fcc crystals, as listed in Table 1.3. In body-centered cubic (bcc) crystals, there are closely packed directions $\langle 110 \rangle$, but no really closely packed planes exist as slip planes. However, this does not mean that there is no slip happening in bcc material. It simply needs more energy, such as a higher temperature, for bcc material to slip. Compared to fcc and bcc material, slip in hexagonal close packed (hcp) materials is much more difficult, as even fewer active slip systems exist in hcp materials.

Table 1.3 12 slip systems operating in fcc crystals.

Slip planes	Slip directions
(111)	$[-110]$; $[-101]$; $[0-11]$
(-1-11)	$[-110]$; $[-10-1]$; $[0-1-1]$
(-11-1)	$[110]$; $[-101]$; $[0-1-1]$
(-111)	$[110]$; $[-10-1]$; $[0-11]$

4. Schmid factor

To activate slip, a characteristic shear stress is required. As shown in Figure 1.3, the shear stress τ_c resolved on the slip plane in the slip direction can be expressed as:

$$\tau_r = \sigma \cos \alpha \cos \beta \quad (\text{Eq. 1.1})$$

In theory, the slip occurs when σ reaches the yield stress σ_y of the material and the shear stress on the slip plane in the slip direction is so-called critical resolved shear stress τ_c . The Schmid factor, m is defined as the quantity $\cos \alpha \cos \beta$. Therefore, the yield stress becomes:

$$\sigma_y = \frac{\tau_c}{m} \quad (\text{Eq. 1.2})$$

From Eq. 1.2, the greater value of m indicates lower applied stress is needed for activating slip. The Schmid factor thus becomes a way of estimating the operating slip systems in crystal materials. Briefly speaking, if one determines the angles between slip systems and the loading direction, then the slip system with the highest Schmid factor m is believed to be the operating slip system in the material.

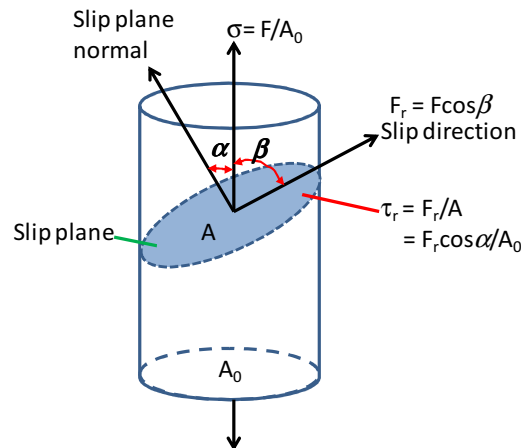


Figure 1.3 Illustration of the geometry of slip in a cylinder. Note that $\alpha + \beta \neq 90^\circ$ in general.

Note that in practice, especially in the case of polycrystalline materials, there usually are more than one active slip systems and sometimes the expected slip system may not even be active because of the interactions from the surrounding grains.

1.1.2 Grain Boundaries

Metallic materials usually exist in the form of a polycrystal, which consists of a collection of single crystallites or "grains". Each of these single grains has its own

orientation and they are held together by some common lattice points, but at other locations between the grains there is a discontinuity. Both these features comprise the grain boundary (GB). The average atomic volume in a grain boundary is greater than that in the grain interior, which indicates that free volume exists in the grain boundary. Excess free volume and lower atomic coordination are fundamental intrinsic properties of grain boundaries, which induce other properties. For example, grain boundaries have higher energy and they are usually more chemically reactive and preferential sites for impurity atoms.

The minimum rotation angle $\Delta\theta$ between the orientations of two adjoining grains is the GB mis-orientation angle. It is the simplest description of the GB structure. In general, grain boundaries can be classified into low-angle grain boundaries (mis-orientation angle $\leq 15^\circ$) and high-angle grain boundaries (mis-orientation angle $> 15^\circ$). The energy of the grain boundary is a function of the mis-orientation angle for low-angle grain boundaries, however, it becomes complex for the high-angle grain boundaries because of the existence of "special" boundaries. The boundaries with markedly different properties (e.g., low energy) or geometry from average are so referred to as "special" boundaries. The coincidence site lattice (CSL) theory is a popular way to describe these boundaries [16-18]. In CSL theory, when superimposing two properly mis-oriented grains, some of the atomic sites coincide and are so called coincidence sites. The coincidence sites throughout the superimposed system create the coincidence site lattice. The reciprocal density of the coincidence sites is then defined as Σ - the degree of coincidence. For example, in Figure 1.4, the two lattices are related by a rotation of 36.9° around the $\langle 100 \rangle$ axis, which leads to one coincidence site in five lattice sites, that is a $\Sigma 5$ CSL grain boundary. Ideally, the Σ number corresponds to an exact mis-orientation angle. However, in practice, the dislocations piled up around the grain boundary change the mis-orientation angle, and thus probably the properties of the grain boundary. Therefore, for a Σ CSL GB, the maximum angular deviation, v_m , is defined, within which the character of the Σ grain boundary is still conserved with the addition of the secondary grain boundary dislocations. This relationship can be empirically expressed as:

$$v_m = v_0 \Sigma^{-\xi} \quad (\text{Eq.1.3})$$

where ν_0 is the angular limit for a low angle grain boundary, for which 15° is usually taken, so that all low-angle grain boundaries can be treated as $\Sigma 1$ boundaries. ξ in the Brandon criterion [19] has generally been assigned a value of $1/2$. A more restrictive criterion uses $5/6$ as ξ , according to Palumbo *et al.* [20]. Though different criteria exist, it is commonly accepted that the grain boundaries with $\Sigma \leq 29$ are special boundaries, as special behavior is often detected for them. A particular interesting case is that of the $\Sigma 3$ boundaries (60° with $\langle 111 \rangle$ axis), which are usually twin boundaries in an fcc crystal structure. Twin boundaries are those with symmetrical lattice points at each side of the boundary. In other words, the lattice from one side of the boundary is the mirror image of the other side. These twin boundaries usually are of very low energy, due to their high symmetric structure.

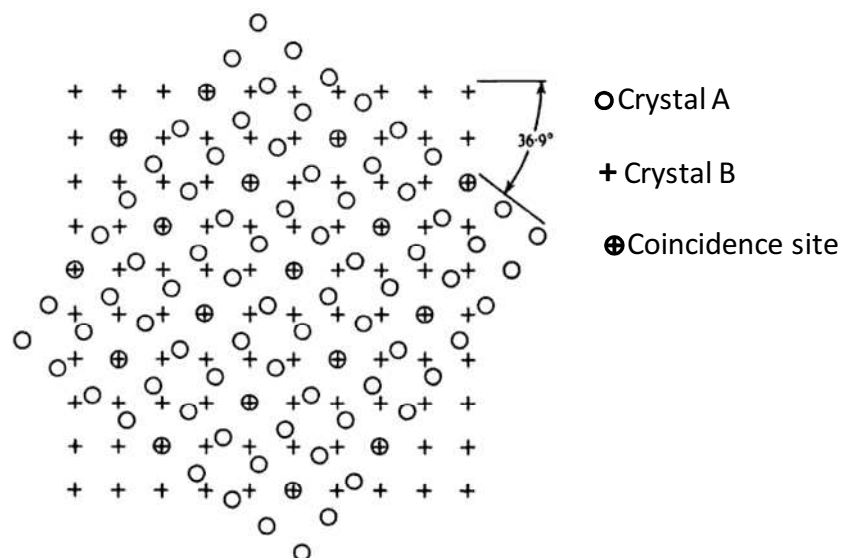


Figure 1.4 An example of coincidence plot of two lattices. It is a $\Sigma 5$ boundary, as every 1 in 5 lattice points coincide with each other. Adopted from Figure 11.1 in [21].

1.2 SCC Studies of Alloy 600

1.2.1 Factors for SCC behavior in Alloy 600

Insights into the mechanism of SCC began with the study of effects of different parameters on SCC. Among these, heat treatment of the material has been studied extensively, as research [22-27] shows that IGSCC is strongly affected by the thermal history of the material. For instance, Stiller *et al.* [23] found that Alloy 600 processed by

mill annealing at 1024 °C cracked 10 times faster in pure water than Alloy 600 processed by mill annealing at 927 °C. Although the exact mechanism of the effect of the heat treatment was not identified, grain boundary chemistry and character was shown to be different for the different heat treatments. The two most obvious grain boundary phenomena of Alloy 600 observed after heat treatment are chromium depletion and the appearance of grain boundary carbides. According to Was [26], the more severe the depletion of chromium, the higher a susceptibility is found for IGSCC in acidic media. The grain boundary carbides can be beneficial or detrimental to IGSCC, depending on the density, structure and morphology of the carbides: grain boundary carbides with a continuous or semi-continuous structure will enhance the resistance of the nickel alloy to IGSCC.

One of the other characteristics of the grain boundary that heavily affects IGSCC behavior is its mis-orientation. Many studies [16, 28-31] have shown that low Σ (≤ 29) grain boundaries are usually less susceptible to IGSCC. However, even the $\Sigma 3$ grain boundaries are not totally immune to IGSCC [29].

The effects of the applied stress axis are also important. The grain boundaries perpendicular to the tensile stress axis are found to be the most favorable cracking direction [32-34].

The effects of prior deformation, including cold work, welding, scratches and indents, have also been widely studied [6, 35-38]. Welding is a fabrication process that joins materials and it usually involves melting a material between work pieces without melting the work pieces. Cold working (CW) is a process which induces plastic deformation by forging or rolling at a temperature below the recrystallization temperature of the material. The percent of cold work (%CW), which is the change in cross-sectional area over the original cross-sectional area, represents the degree of plastic deformation. The welding procedures and cold work are both found to affect the crack growth rate [37]. The specimen with 20% cold work was reported to have the highest crack growth rate, compared to those with 8% and 40% cold work. Also, both IGSCC and TGSCC have been only found in 40% cold worked Alloy 600, while only IGSCC

occurred in the 8% and 20% specimens. It was proposed in this paper [37] that the crack growth rate is related to the crack tip mechanics, the sub-microstructure after cold work, and the crack tip oxidation process. Generally, cold work was believed to increase yield strength, to decrease the material ductility and to cause local high stress or clusters of dislocations, especially at grain boundaries. Cold work may also change the microstructure or sub-microstructure of the material, depending on how much deformation is applied. Levels of 8% and 20% cold work are moderate and do not change the microstructure significantly. The enhanced yield strength resulted in a high local stress at the crack tip, which thus speeds up crack growth. In the case of the 40% cold work, the material microstructure changed severely into a cellular texture and the differences between the original grain boundaries and intragrain region became very small, thus cracking preferentially occurred transgranularly (TGSCC).

Studies have also been carried out on the effects of the oxide film [39, 40], electrochemical potential [41], additives (e.g., lead) [42, 43] on SCC. The additive lead has gained a lot of attention, as it is one of the species that can result in rapid SCC and general corrosion in Alloy 600, but also in Alloy 690 and 800 with their various heat treatments [43].

1.2.2 Mechanisms

Mechanisms for SCC have been proposed and reviewed by different groups [44-49]. The slip dissolution/film rupture model and the hydrogen embrittlement model are two classical mechanisms which may account for most known cases of SCC [47]. The main idea of the slip dissolution/film rupture model is that plastic strain, concentrated at the crack tip causes slip in the metal crystal. This slip results in a break in the surface oxide film that had previously protected (or “passivated”) the metal from corrosion. Then, oxidation/dissolution of the underlying bare metal could occur. In another words, the crack grows with a cyclic process of film rupture, dissolution and film repair. Hydrogen embrittlement usually happens in an aqueous environment where hydrogen may be present. The hydrogen atoms diffuse through the metal and recombine together

in metal defects, which build up a high local stress and cause cracking when the stress is high enough.

The internal oxidation model was first proposed by Scott and Le Calvar [50] in 1993. The base of this model is oxygen diffusion in the metal matrix. Then the dissolved oxygen would oxidize a reactive alloying element in the material and form a brittle intergranular oxide, CO₂ bubbles or an oxygen film, which could cause embrittlement. Another mechanism proposed by Angeliu *et al.* for IGSCC [51] is the creep damage model, where voids caused by creep collect at grain boundaries and exert a local stress until a crack is generated.

However, no single model can account for all SCC phenomena found in Alloy 600. For example, according to the slip dissolution model, factors like Cr depletion that can increase the metal dissolution rate are expected to enhance SCC, but Cr depletion has been found to have no such effect on Alloy 600 SCC in some cases [52]. The hydrogen embrittlement model was found to describe Alloy 600 SCC in caustic solution within a certain potential range [44]. However, the operating mechanism seems to change with the environment and condition of the alloy.

1.2.3 Remedies

As seen in the definition of SCC, SCC behavior is controlled by mechanical, chemical and metallurgical factors. The most effective and common method used to control SCC would be to remove or prevent the application of the tensile stress. The stress usually is induced by faulty installation or residual stress from improper manufacturing procedures, such as welding, bending or accidental denting of the material. Annealing or shot peening are often used to reduce/remove the stress and so decrease the possibility of SCC. The other methods would be either changing/modifying the chemical environment for a special material or selecting a different material for construction that is immune to SCC under this particular environment, such as one with more “special boundaries” [31, 53, 54].

1.3 Diffraction Techniques for Microscopic Deformation Studies

As discussed above, the residual stress/strain is the key driving force for the evolution of the microstructure in materials and has long been associated with SCC, therefore how to accurately measure it in grains and at the grain boundary becomes rather important to localize and analyze the initiation and growth of the intergranular cracking. Generally, to comprehensively understand the mechanical properties of polycrystalline materials, the ability to completely characterize their microstructure at every length scale, from the macroscopic to the atomic level, is required. Neutron diffraction, EBSD and the relatively new PXM method are the major non-destructive methods used for determination of microstructure and mechanical strain. Each of the three techniques has its strengths and weaknesses; these are summarized in Table 1.4.

Table 1.4 Comparison of different non-destructive strain detection techniques.

	EBSD	PXM	Neutron Diffraction
Detects elastic strain?	Yes	Yes	Yes
Detects plastic strain?	Indirectly – requires calibration	Yes	Yes
Information depth	2 μm	10 – 100 μm	cm
Lateral resolution	~100 nm	1 μm	Low
Depth resolution	No	1 μm voxels	No
Strain sensitivity	Unknown	1×10^{-4}	1×10^{-5}
Strain latitude	Unknown	$\leq 5\%$	$> 10\%$
User accessibility	Good	Low	Low

Neutron diffraction, because of the high penetration of solids by neutrons, provides only a bulk assessment of strain; however, it can provide quite accurate information on the crystallographic directions where strains have accumulated in a solid. EBSD has such a high surface sensitivity that careful surface preparation is required to eliminate effects that are unrelated to the real strains in the sample. However, EBSD does allow measurements with very high spatial resolution and the technique can be accessed in a number of laboratories. PXM seems well suited to examine strain in a region extending down some 100 microns into the nickel alloy. Within such an information depth, strain relationships along the lengths of several grains can be followed.

In the content below, the new technique PXM will be discussed in details, while a brief description is given for the EBSD and neutron diffraction.

1.3.1 Polychromatic X-ray Microdiffraction (PXM)

X-ray diffraction has been routinely used to study the structural properties of materials. It has long been used for strain measurement in metals, however not on a micro scale until more recently. With the development of high-brilliance synchrotron radiation sources and advanced x-ray optics, polychromatic x-ray microdiffraction (PXM), which is Laue diffraction, has become an effective technique capable of detecting local variations of mesoscale structure and strain (0.1 - 100 μm). It uses polychromatic x-rays as the incident beam and obtains reflections from different crystallographic planes at one shot without sample rotation, whenever Bragg's law (Eq. 1.4 as below) is satisfied.

$$\lambda = 2d \sin \theta \quad (\text{Eq. 1.4})$$

where λ is the wavelength of the incident beam, d is the spacing between planes in the atomic lattice and θ is the angle between the incident beam and the scattering plane.

1.3.1.1 Synchrotron Radiation

When charged particles, such as electrons, travel in a circular orbit with high energies at relativistic speed (a speed close to light), radiation tangential to the orbit will be emitted, which is called the "synchrotron radiation" [55]. The electron accelerator that confines the electrons in the orbit is known as storage ring. In Figure 1.5a, a schematic layout of the modern storage ring is presented. Electrons are initially generated from the electron gun and accelerated to nearly the speed of light (99.9997%) in the linear accelerator (linac). Then the electrons are transferred to the booster ring and increased in energy. Finally, the electrons with certain energy are poured into the outer storage ring and circulated in the ring. A beam of light is then produced at the deflection of the electron path and guided to the end station for experimental use after focusing.

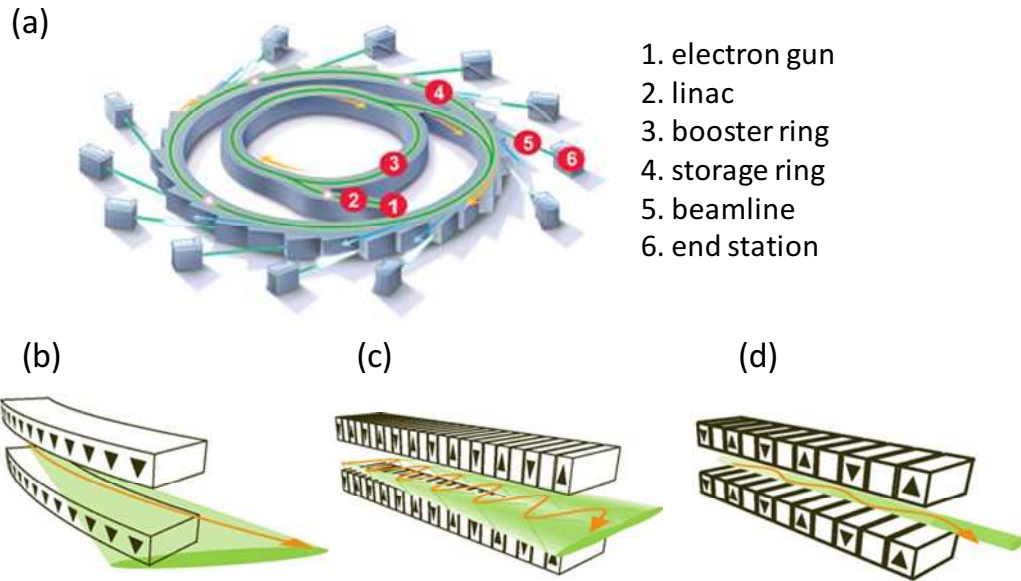


Figure 1.5 Illustrations of (a) the storage ring, (b) bending magnet, (c) wiggler and (d) undulator. Differences in the size of the photon beam achieved from the three magnetic elements are also shown. Adopted from [56].

Though with the name “ring”, the storage ring is composed of curved sections with a series of bending magnets separated by straight sections. Wigglers and/or undulators, which are referred to insertion devices, can be positioned in the straight sections of the storage ring. Unlike the bending magnets, wigglers and undulators are magnetic devices introducing periodic magnetic fields on the electrons. An illustration of bending magnets and insertion devices is shown in Figure 1.5(b-d). The differences of the emitted radiation size from the three devices are also displayed.

At the relativistic speed, the radiation emitted is folded in the forward direction into a cone with an opening angle (full angle of the divergence, refer to Figure 1.5a)

$$\psi [\text{rad}] \sim 1/1957E [\text{GeV}] \quad (\text{Eq. 1.5})$$

where E is the electron energy in GeV. This means that the synchrotron radiation with higher electron energy will have a smaller opening angle and thus generate brighter synchrotron light. The undulators give a cone with the smallest opening angle, which indicates very bright beams. Generally, the intensity of the radiation is directly related to the strength of the magnetic field and the energy of the electron in the storage ring.

Synchrotron radiation has several advantages over the traditional x-ray sources, making the synchrotron radiation facilities such an attraction to researchers.

1. Broad spectrum. It covers continuously from Infra-red to gamma rays, which users can select according to their experimental needs.
2. High brightness. It is highly collimated beam with good spatial coherence. This is particularly true for the polychromatic radiation used in our experiments.
3. Pulsed time structure. The electrons are stored and accelerated in bunches. By controlling the frequency of replenishment, different time structures can be achieved.
4. Polarization. It is almost 100% linearly polarized in the plane of the electron orbit. Circular polarization can also be achieved by adjusting the insertion devices.

1.3.1.2 Experimental Setup of PXM

PXM is capable of detecting 2D and 3D information in materials [57-63]. Figure 1.6 shows the general experimental arrangement of 2D PXM. The polychromatic x-ray beam impinges directly on the Kirkpatrick-Baez (K-B) mirror pair, which provides both vertical and horizontal focusing of the x-ray beam and then onto the sample. Samples are mounted on movable plates and positioned by a computer-controlled three-axis translation stage. Samples are usually set at a 45° reflective geometry with the CCD (charge coupled device) area detector on a vertical slide at a certain distance from the sample area illuminated by the beam. The CCD is used to collect the Laue patterns generated by the grain volume of the sample exposed to the x-ray beam. Then all the patterns collected by CCD are sent to a computer. The analysis software in the computer provides fitting of the Laue patterns, automatic indexation and extraction of crystal orientations and full strain information [64].

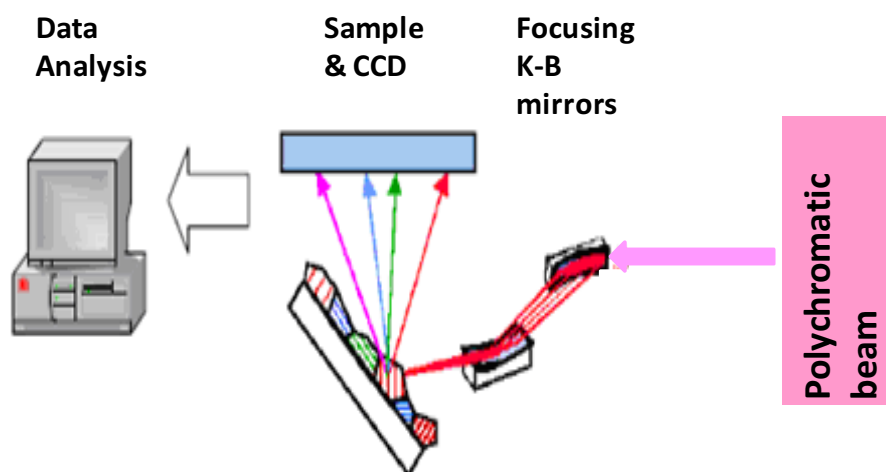


Figure 1.6 General experimental arrangement of PXM. Modified from [65].

For 3D PXM, a Pt wire is positioned between the sample and the detector and used as a “differential-aperture” to depth resolve the Bragg diffracted intensity from the sample; this is thus usually referred to as “differential-aperture x-ray microscopy” (DAXM) [59, 63, 66]. At each sample position, the Pt wire takes submicron steps parallel to the sample surface. Then the sample moves to the next position and the Pt wire repeats its steps until the target sample area is finished scanning. The full diffraction patterns for each step length along the penetration direction can be computer-reconstructed. Then the data is processed the same way as the 2D PXM data and a real 3D information is obtained from the sample.

1.3.1.3 Data Processing

The first and most important step is obviously to find the reflection positions on the CCD detector and to index them. The details about the algorithm can be found in references [64, 67]. Generally, the CCD/sample geometry is first determined using a silicon Laue pattern as a reference. The inter-ray angles for the Laue spots are determined and compared to known calculated values with an adjustable angular tolerance until a match is found. Once the indices for all reflections are obtained, the lattice orientation and the experimental unit-cell parameters are determined for each pixel illuminated by the microscopic beam.

Basically, the strain tensor (residual elastic strain) is determined by comparing the measured unit-cell parameters to unit-cell parameters of a strain-free sample. The complete strain tensor contains two terms – distortion/deviatoric strain and hydrostatic strain (dilatation), shown as below

$$\boldsymbol{\varepsilon} = \begin{pmatrix} \varepsilon_{11} - \frac{\Delta}{3} & \varepsilon_{12} & \varepsilon_{13} \\ \varepsilon_{21} & \varepsilon_{22} - \frac{\Delta}{3} & \varepsilon_{23} \\ \varepsilon_{31} & \varepsilon_{32} & \varepsilon_{33} - \frac{\Delta}{3} \end{pmatrix} + \begin{pmatrix} \frac{\Delta}{3} & 0 & 0 \\ 0 & \frac{\Delta}{3} & 0 \\ 0 & 0 & \frac{\Delta}{3} \end{pmatrix} \quad (\text{Eq. 1.6})$$

where $\Delta = \varepsilon_{11} + \varepsilon_{22} + \varepsilon_{33}$ and $\frac{\Delta}{3}$ is defined as the hydrostatic strain. In Eq. 1.6, the first component is the distortional term and the second term is the dilatational term.

However, only the deviatoric strain is determined in this thesis. The unit cell volume which is necessary for hydrostatic strain can only be determined by measuring the energy of one of four independent reflections. But compared to polychromatic beam Laue diffraction, measurements with scanable monochromatic beam are too time-consuming. Moreover, in most cases, the deviatoric term contains all the information needed for the study of deformation. In other words, the hydrostatic strain components are not important to be included because most changes occurs in deviatoric components. Other than the directional strain components, von Mises strain, a scalar measure of the strain in the sample, is also presented in our work. It is calculated according to

$$\varepsilon_{vm} = \frac{1}{\sqrt{2}} \sqrt{(\varepsilon_{xx} - \varepsilon_{yy})^2 + (\varepsilon_{yy} - \varepsilon_{zz})^2 + (\varepsilon_{zz} - \varepsilon_{xx})^2 + 6(\varepsilon_{xy}^2 + \varepsilon_{yz}^2 + \varepsilon_{zx}^2)} \quad (\text{Eq. 1.7})$$

Plastic deformation is another piece of important information that can be deduced from PXM. It basically comes from the assessment of the distortions in the Laue spots. As dislocations form in the material by plastic deformation, local curvature happens in the lattice. This results in the streaking/splitting of the reflections. In Laue diffraction the orientation of the diffracting volume determines the position of the spots. The spots become streaked if the orientation within the diffracting volume changes continuously,

which is usually due to the presence of dislocations. The streaking direction is directly related to the lattice curvature and the dislocation density. When the diffracting volume contains GN boundaries and the cells separated by the GN boundaries are oriented differently enough, the Laue spots become discontinuous (split). Note that only dislocations with the same sign, in other words, GNDs cause the streaking/splitting of Laue spots, since paired dislocations annihilate the effects of each other. Thus the information about the number and kind of GNDs can be recovered from the streaking/splitting in Laue images. The detailed theory is discussed by Barabash and Ice *et al.* [68, 69]. The local lattice curvature and GNDs density is determined first from the analysis of the orientation change at each probed location. The GNDs density is then modeled to determine the most probable primary GNDs slip systems activated. Different combinations of most probable GN slip systems can be further used to model lattice curvature and GNDs density tensors, and to numerically calculate Laue patterns close to the experimentally observed one. Least square fitting was adopted between experimental and simulated Laue spots to find the combination of GN dislocation population best fitting the experimental data. The model takes into account most probable slip systems. Certainly, real dislocation networks are always more complicated than the model one due to the formation of small densities of dislocations in even the least active slip systems. This introduces small differences between experiments and simulations.

Local mis-orientation (local change in the crystal orientation), a common way of measuring the plastic deformation used in EBSD, has also been adopted in PXM. The mis-orientation measurement by PXM is much more accurate than by EBSD, due to its higher sensitivity.

1.3.2 Electron Backscatter Diffraction (EBSD)

Electron backscatter diffraction (EBSD) is a microanalysis technique which provides the crystallographic nature of samples in Scanning Electron Microscope (SEM). With the emerging of the automated data acquisition features, EBSD is also known as Orientation Imaging Microscopy (OIM). In Figure 1.7, the general setup of the EBSD is shown. The electron beam of the SEM operating in the spot mode scans the highly tilted

sample surface (usually $\sim 70^\circ$) with a certain step size. The sample is mounted on a moveable sample stage. Either the sample stage or the beam is moved to accomplish the scan. For each point with its coordinates (x,y), an electron backscatter diffraction pattern (EBSP) is generated on the phosphor screen and then is captured by the camera and subsequently indexed by the automated computer system. EBSPs are essentially Kikuchi patterns and the bright bands are so called "Kikuchi bands" (a pair of Kikuchi lines). The Kikuchi lines are formed by elastic scattering from the crystal planes when the Bragg's law is satisfied. Inelastic scattering is also happening, which contributes to the blurring of the lines and high background.

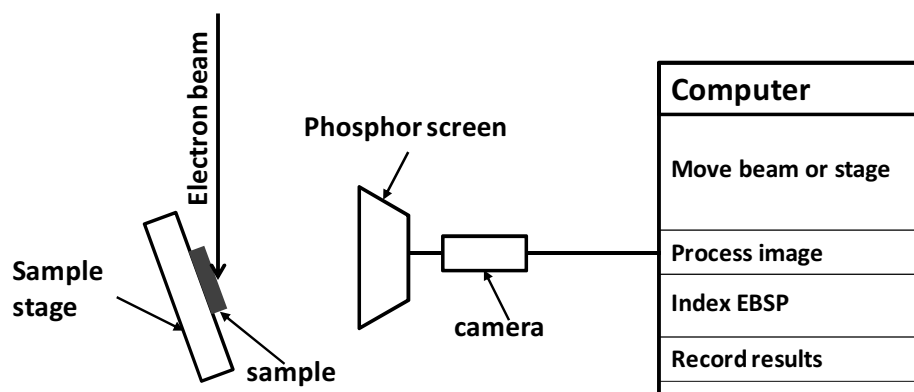


Figure 1.7 Schematic diagram of electron backscatter diffraction system in SEM.

Besides the crystallographic aspects of the microstructures (orientation), the strain information can also be obtained from EBSD. Elastic strain distorts the crystal structure, which may cause the shift of the Kikuchi lines, changes of the bandwidths, and/or even blurring of the edges of the diffraction bands. This makes the elastic strain measurement rather difficult practically, as the one or two pixel shifting from the lattice bending is too small to be detected unless the images are taken at high resolution with very careful image analysis. Plastic strain, existing as the form of dislocations, usually make the diffracting patterns more diffuse. Two main methods [70] have been proposed for making quantitative measurements of plastic strain: the image quality approach and the local mis-orientation approach. However, neither of them give the actual strain values, as both methods are indirect, employing calibration curves based on the changes of the diffraction patterns in the strained sample relative to those from unstrained materials. Local mis-orientation has been used quite extensively to analyze the plastic

strain in metals [71-74]. A full discussion about the potential and limitations of EBSD in characterizing the elastic and plastic strain can be found in [70].

1.3.3 Neutron Diffraction

Neutron diffraction is a form of elastic scattering. It also relies on the Bragg's law, which stipulates that neutron wave reflects on lattice planes when the condition in Eq. 1.4 is satisfied. For a polycrystalline sample, the detector at a particular orientation relative to the incident beam records all the signals from the lattice planes that satisfy the Bragg's law. In other words, the diffraction signals of the lattice planes from many grain depths can be recorded on the detector with one shot, due to the large penetration depth of the neutrons and the large beam spot size. A neutron diffraction measurement requires a neutron source, a sample, and a detector. Free neutrons do not usually occur in nature, because of their short life time. Nuclear reactors are the main sources of neutrons generated artificially. The other most used source is spallation source, which irradiates a metal target with high-energy protons from an accelerator. Samples are generally large in size compared to those used in PXM or EBSD. More detailed instrumentation can be found in [75].

1.4 Objectives and Arrangement of the Thesis

This thesis is part of the COG (CANDU Owners Group) project, a joint project between industrial partners and different academic groups. The overall purpose of this project has been to generate methodologies for the analysis of stress corrosion cracks, especially the microstrain distribution along the crack path and determine its composition using analytical techniques. There are two main objectives in this thesis: first, to evaluate the reliability and limits of the application of PXM on microstructural and strain analysis of Alloy 600, by comparing the results with those from the other advanced techniques, neutron diffraction and EBSD; second, using PXM to study changes in microstructure and microstrain distribution before and after SCC crack initiation and to establish the connections between these changes and the SCC process.

The structure of this thesis is as follows. Chapter 1 provides a general description of some basic concepts (e.g., dislocations, slip, grain boundaries), a brief review of SCC factors, mechanisms and the remedies, as well as a comprehensive discussion of the three microanalysis techniques (PXM, EBSD and Neutron diffraction). Chapter 2 describes the sample preparation methods and instrumentation used in this thesis. Chapter 3 evaluates the reliability of PXM on Alloy 600 study by comparing the PXM results from uniaxial tensile stressed samples with those from EBSD and neutron diffraction. Then Chapter 4 displays the detailed PXM results of samples that had been externally stressed by a uniaxial force. It shows some of the more promising parts of the PXM technique. We then move to the C-ring samples in the remaining chapters, as C-rings are a popular means for determining the susceptibility to SCC of alloys. The microstructure and microstrain changes after applying stress to a C-ring is described first in Chapter 5. In the following chapters, different C-rings were used to generate cracks and studied by PXM. In Chapter 6, PXM studies are shown for samples that were electrochemically corroded to produce SCC. Chapter 7 discussed the results of PXM from a massive SCC crack with 24h corroding time. Last, in Chapter 8, a summary of the work in this thesis is presented and the possible additional work is suggested.

Chapter 2

2. Experimental Details

This chapter contains general information regarding all the samples and various experimental techniques employed in this thesis project. It also includes experimental procedures that are common to all samples. Additional experimental details will be provided, as necessary, immediately prior to the discussion of results in later chapters.

2.1 Specimen Description

Nickel Alloy 600, also known as Inconel 600, was used for all the studies discussed in this thesis, either in the form of tensile test specimens or C-ring samples. The tensile samples were provided by Atomic Energy of Canada Limited (AECL) and were stress relieved at 800°C in flowing argon for 1hr in a furnace. Note that not the complete thermo-mechanical history of the samples has been described as it is not known by the authors. The resultant specimens had large “domains” with equi-axed grain structures, but the grain size varied from domain to domain, the largest being ~200 μm and the smallest ~10 μm . The C-ring samples were made from actual SG tubes, which were produced by Rolled Alloys™ in the bright annealed condition. The average grain size is ~25 to 40 microns. The compositions for the tensile samples and the C-ring samples are summarized in Table 2.1, which were provided by the supplier.

Table 2.1 Chemical composition of bar samples and C-ring samples.

wt.%	Ni	Cr	Fe	C	Si	Mn	Cu	Ti	Al	S	Mo
Bars	balance	15.5	8.8	-	0.2	0.2	0.2	0.3	0.3	-	0.2
C-rings	72.4	16.2	9.7	0.02	0.39	0.79	0.01	-	-	0.003	-

2.2 Specimen Preparation Techniques

Before detailed description of techniques used to process the samples, a summary of the treatments of samples is listed in Table 2.2. Three tensile test samples were studied in this thesis: the control sample without applied strain, a specimen from the middle part of the tensile bar (mid-bar sample) and one from the end of the same tensile bar (end-bar sample). As well, five C-ring samples were studied, two of which were not cracked by

SCC, while the other three were SCC cracked with different corroding time in the autoclave.

Table 2.2 Summary of treatments of samples studied in this project.

samples		Strain history	Surface treatment	SCC test
Tensile	Control	No applied strain	Mechanical polish + eletropolish	-
	Mid-bar	0.5% plastic strain	Mechanical polish + eletropolish	-
	End-bar	0.5% plastic strain	Mechanical polish + eletropolish	-
C rings	Unstressed	No applied strain	Mechanical polish + FIB polish	-
	Stressed	2% plastic strain	Mechanical polish + FIB polish	-
	6h	2% plastic strain	Mechanical polish + eletropolish + FIB polish	6h
	18h	2% plastic strain	Mechanical polish + eletropolish+ FIB polish	18h
	24h	2% plastic strain	Mechanical polish + FIB polish	24h

2.2.1 Uniaxial Tensile Test

The purpose of this test is to generate a simple case of residual elastic strain and plastic deformation, which then can be studied by PXM and so evaluate the reliability of PXM technique. This test was carried out by our collaborators in the Department of Mechanical Engineering at UWO. Standard bar-type tensile specimens were used for this test. The specimen was uniaxially stretched to a nominal 1% extension using an MTS tensile tester QT/25. Two marks were made on the specimen and the distance between the marks was measured before and after stretching (Figure 2.1a). The nominal strain (engineering strain) was calculated by using the change in length over the original length. In real cases, especially during the tensile test, the cross sectional area and the length of the specimen change with the stretching process. Thus the engineering stress/strain that is calculated based on fixed references (the original cross sectional area and original length) is not the true stress/strain at that particular moment. True stress/strain gives a more accurate measurement by using the instantaneous values for area/length. In Figure 2.1b, the true stress-true strain curve for the tensile test is shown. The end point is beyond the yield point and this may have resulted in some macroscopic plastic deformation. Analysis of the resulting stress-strain curve [76] indicates that this sample endured an average uniaxial plastic strain of about 0.5%.

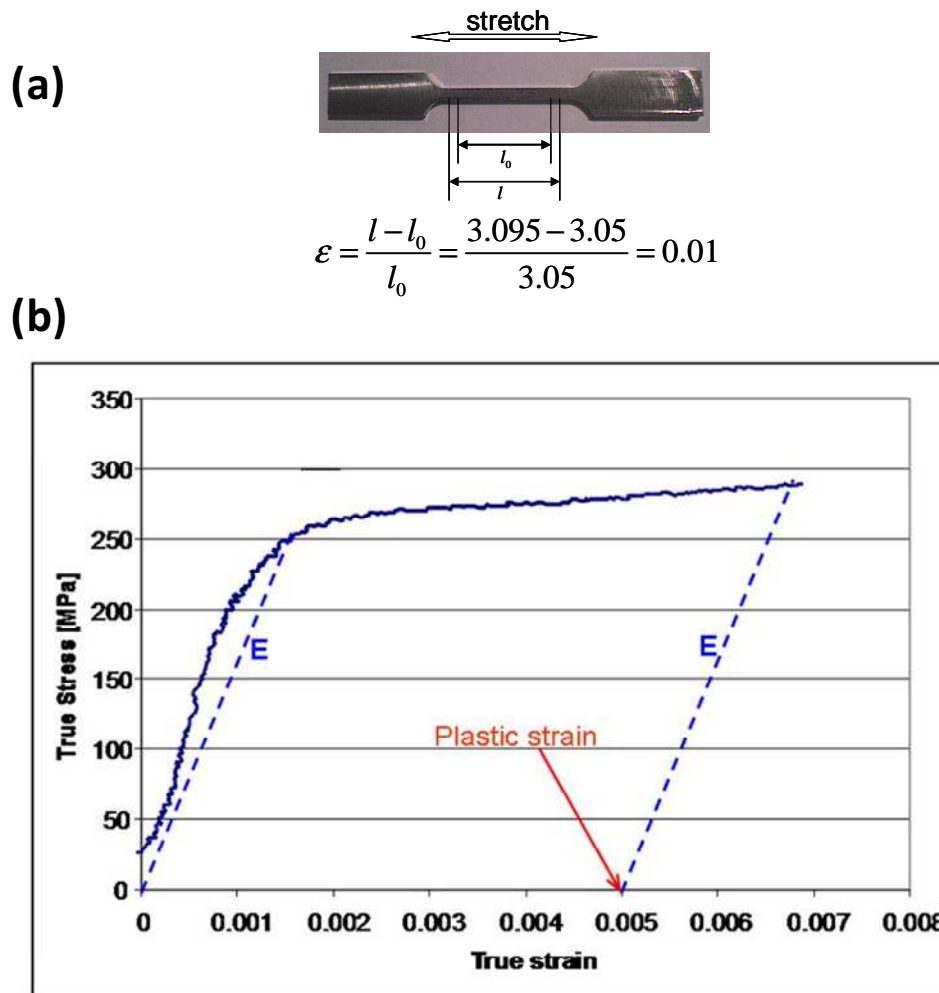


Figure 2.1 (a) Layout for the tensile test. The engineering strain was calculated to be 1%. (b) True stress-true strain curve for the Alloy 600 tensile test. E is the Young's modulus. The residual plastic strain is calculated to be 0.5% shown in the figure.

2.2.2 Making C-Ring Samples

C-rings are commonly used to determine the susceptibility of SCC in different materials. They were prepared according to ASTM standard G-38 [77]. Two cm long sections were cut from the tubing, which has an outer diameter (OD) of 15.1 mm and tube thickness of 1.2 mm. Care was taken during sectioning by employing a diamond saw with sufficient cooling such that the cut edges were smooth and sections were not heated up during cutting. Slots were cut and holes were drilled in these sections for the fabrication of C-rings. The cut edges were polished to a smooth finish. The outside diameter surface was also polished through various grit silicon carbide papers, down to a 0.05 micron alumina finish. Then the polished sections were stressed to 2% plastic strain

by screwing Alloy 600 bolts and nuts, as shown in Figure 2.2. This strain value was estimated roughly by assuming that the stress-strain curve is still linear when applying a stress at ten times of the yield strength.



Figure 2.2 Optical images of a C-ring: (a) before and (b) after stressing by bolt tightening to achieve a nominal 2% strain. Green boxes at the sample apex indicate the analysis area.

2.2.3 SCC Test

This test is to generate cracks in the C-ring samples by SCC. This test was done by our collaborators at University of Toronto. In their facility SCC of Alloy 600 has been able to be induced in acidic or caustic environments. In this work, a caustic solution was used for all the SCC tests. Samples were spot welded to Ni wires and suspended from electrode holders. Then the samples were exposed in an autoclave containing a solution, 10% by weight NaOH in deionized water (resistivity of 18.2 M Ω -cm), at a temperature of 315 °C [78, 79]. All tests were conducted in a 0.5-L nickel beaker (liner) containing 230 mL of solution inside an alloy-625 autoclave. Prior to heating the autoclave, the caustic solution was deaerated by nitrogen for at least 12 hours. After temperature stabilization, a potential of +150mV vs. a pseudo-reference electrode of Alloy 600 was applied to the whole sample (C-ring, bolt and washer assembly) and the total current density was monitored. After initial decay from 100-200 $\mu\text{A cm}^{-2}$, the current densities finally reached values of 25-35 $\mu\text{A cm}^{-2}$, depending on the total exposure time.

2.2.4 Sample Surface Treatment Techniques

All the polishing procedures are adopted to smooth the sample surface and so minimize the residual stress. The purpose of the etching procedure is to reveal the microstructure of the sample surface.

1. Mechanical polishing

A polishing machine at Surface Science Western (SSW) was used to conduct the mechanical polishing. The surface of interest from samples was polished with graded silicon paper, followed by diamond pastes with diminishing particle size and then with 0.05 μm $\gamma\text{-Al}_2\text{O}_3$ paste.

2. Electropolishing

Electropolishing, also known as electrochemical polishing, is an electrochemical process removing materials from a metallic work piece. It can eliminate some of the defects after mechanical polishing and thus further improve the surface condition (e.g., less residual deformation), by removing the top most plastically deformed surface layer. Two methods of electropolishing were adopted in this work:

(i). A solution of 10% perchloric acid in methanol at $-60\text{ }^\circ\text{C}$ and with a potential of 40 V DC for 8~10 sec. This method has only been used for the mid-bar tensile test sample, which was carried out by Kinetrics - one of our collaborators. It should be noted that perchloric acid is dangerous to work with, as it is explosively unstable and can be exceedingly corrosive to skin at its anhydrous state.

(ii). A solution of 25 vol.% nitric acid and 25 vol.% phosphoric acid in water at ambient temperature, using a potential of 0.81 V to SCE (Saturated Calomel Electrode) for ~1 min. This is the method that was used for other samples where electropolishing was needed.

3. Focused ion beam (FIB) process

Focused ion beam (FIB) is a technique being widely used in semiconductor research and processing environments. FIB setup is similar to that of scanning electron microscope (SEM), except for the use of the focused ion (usually gallium ion Ga^+) beam

instead of a focused electron beam. However, FIB is generally incorporated into a system with both ion and electron beam sources. FIB allows imaging, localized milling and even deposition of materials with high precision when combined with a gas injection system.

In this work, FIB milling and deposition were applied to all C-ring samples. The LEO 1540XB, a dual beam system with a gas injection system at the Western Nanofabrication Laboratory, was used. A focused beam of gallium ions was used to remove mechanical damage from the near surface region by ion bombarding at a glancing angle, over an area close to the edge of the apex of the arch at the flat end face. Subsequently, this ion bombardment was found to have no measurable effect on the strain measurements of the surface. Also, using the ion beam, cuts were made in the surface as markers of features in the microstructures; these could be identified by optical microscopy at the synchrotron. As well, localized platinum deposition was used to mark regions on the sample. These regions could also be identified by X-ray microfluorescence spectroscopy (μ XRF) during analysis at the synchrotron. In Figure 2.3, an SEM image of the surface after FIB processing was shown as an example. Note that though FIB smooths the surface by removing the strained layer at the top most surface, it can create defects (e.g., scratches) because of different milling rate for grains with different orientations.

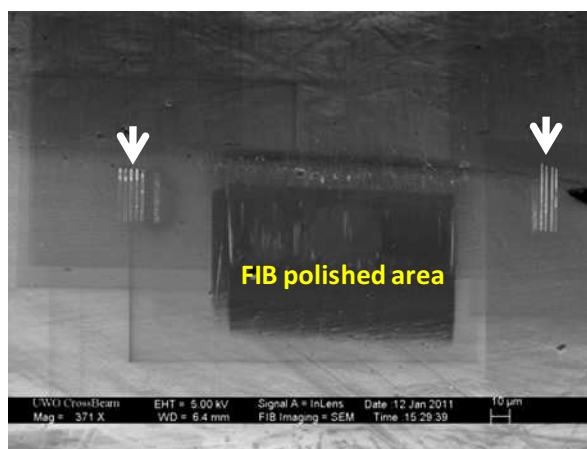


Figure 2.3 SEM image of the FIB polished area at the flat end face. Cutting lines and Pt lines were made on both sides of the polished area, to help find the area during Laue diffraction.

4. Etching

Etching is a primary process used in metallography to reveal the microstructure of a specimen. Though some information can be obtained from as-polished surfaces, the microstructure is usually visible only after etching as light is uniformly reflected on a polished sample [80]. The most commonly used etching method is electrochemical etching, a forced corrosion process by applying an external voltage. In this process, the metallic elements within each grain orientation dissolve at different rates because of differences in surface energy. The light can thus be reflected from the attacked grains and boundaries at an angle, creating the microstructure contrast.

In this work, etching was carried out in 10 vol.% HCl and 90 vol.% methanol solution at room temperature with a DC voltage at 4.0 V. The sample was connected to the positive electrode as the working electrode, while a Pt wire, which was connected to the negative electrode as the counter electrode, was swept over the top of the sample surface without touching the surface for ~ 20 sec.

2.3 Polychromatic X-ray Microdiffraction (PXM)

2.3.1 PXM Beamlines

PXM studies were carried out on Beamline 34ID-E at the Advanced Photon Source (APS) of the Argonne National Laboratory (ANL) and Beamline 12.3.2 at the Advanced Light Source (ALS) of the Lawrence Berkeley National Laboratory (LBNL).

Beamline 34ID-E at APS is an undulator x-ray source, with an optimal beam size of $0.3 \mu\text{m} \times 0.3 \mu\text{m}$. The beam energy can range from 7 keV up to 30 keV. Note that undulators are not ideal for white beam experiments due to their highly structured energy spectrum, it is usually achieved by tapering the magnetic gap or aligning them off-axis. Beamline 12.3.2 at ALS is a source from a superbend magnet, with an optimal beam size of $0.5 \mu\text{m} \times 0.5 \mu\text{m}$. The energy range is 6 – 22 keV. There are several different types of detectors at each beamline. For our experiments, a Roper Scientific PI*SCX:4300 CCD detector was used at APS, while a Dectris Pilatus 1M Pixel detector was used for collecting PXM data at ALS. The detailed beam parameters were slightly different for

each experiment (e.g., beam spot size) as the beam status can somehow drift a bit at each visit.

VESPERS (Very powerful Elemental and Structural Probe Employing Radiation from a Synchrotron) at Canadian Light Source (CLS) is another new PXM beamline under development. It is a bending magnet beamline with a typical beam size of (2 - 4) μm x (2 - 4) μm . Experiments have also been carried out there, however, the data was not satisfactory because the pixel mapping calibration in the CCD detector had not been completed and some inherent strain tensors were found to exist in all maps collected. Therefore, the results from these experiments were not presented in this thesis.

2.3.3 Data Analysis Software

The software packages, XMAS (X-ray Microdiffraction Analysis Software) and ThreeDimX-RayMicroscopy, used to process the data, were respectively obtained from the group at beamline 12.3.2 at the Advanced Light Source (ALS) [3], and the Advanced Photon Source (APS)-Oak Ridge National Laboratory (ORNL) group at the APS beamline 34-ID-E [2]. The algorithms used for both software codes are similar, but not identical. The lattice orientation is determined to within 0.01° [65]. These software packages are capable of processing Laue patterns even when there are interfering patterns from nearby grains. Indexing can sometimes be done using as few as four diffraction spots but more spots greatly increase the accuracy of the results. The results of these analyses are presented as two-dimensional maps of the crystallographic orientation and the components of the residual deviatoric elastic strain tensor over the detected region. ThreeDimX-rayMicroscopy was used to plot the orientation maps and measure the GB mis-orientation angles. Strainviewer, a software program developed in our own group, was also used to plot strain maps and calculate the average strain for each map.

FOXMAS (Fast Online X-ray Microanalysis Software) is parallelized software [81] developed using the XMAS code and was also used to process some of the Laue data. In addition to calculating the orientation maps and strain maps, FOXMAS has capabilities for assessing streaking of a Laue spot, in particular the direction of the streak

and its shape as measured by the ratio of its major to minor axes, the so called “ellipticity map”. In addition, FOXMAS software is capable of measuring and comparing the angle of mis-orientation with respect to a particular crystal plane for any Laue diffraction pattern associated with a particular pixel. The local mis-orientation maps produced employ the same convention as those used in the EBSD measurements. That is, the mis-orientation angle between every two adjacent pixels is calculated first using the orientation matrix. Then the local mis-orientation angle of a pixel is assigned to be the average of mis-orientation angles between this particular pixel and its eight neighbours, but only those angles smaller than 5° are adopted. Any local mis-orientation with angles between 5° and 15° are counted as low angle grain boundaries.

2.4 Electron Backscatter Diffraction (EBSD)

EBSD measurements for bar samples in Chapter 3 were performed at Kinetrics using an EBSD detector attached to a Philips XL30 FEG-SEM. A 15 kV accelerating voltage was employed for this examination with a working distance of 10 mm. EDAX/TexSEM TSL OIM Software was used for data acquisition and data processing. EBSD scans were performed on the tensile bar samples using step sizes ranging from 1 to 4 μm . The number of steps varied from 300×300 steps to 700×900 steps and the step size varied accordingly so that the data acquisition could be completed within a day.

EBSD measurements have also been performed on the 24h SCC-cracked C-ring specimen by our collaborators at University of Toronto. EBSD measurements were done on a Field Emission SEM using a Nordyls detector (Oxford Instruments), and Channel 5 HKL software. An accelerating voltage of 20 keV and a beam current of 20 μA were used during the pattern acquisition. The electron beam was scanned across the sample surface in a raster motion, and orientation data were obtained at 1 μm intervals, from which local mis-orientation maps were calculated. The method of calculating local mis-orientation has been described in section 2.3.3. Prior to EBSD measurements, the sample surface around the crack was electropolished in order to reduce the contribution of surface asperities to the mis-orientation result.

2.5 Neutron Diffraction

The neutron diffraction measurements were performed on the control bar sample in Chapter 3 by our collaborators at Queen's University. The strain measurements were performed on the L3 beam line at the Canadian Neutron Beam Centre (CNBC) at Chalk River Laboratories (CRL) using a monochromatic beam and a 32-wire position sensitive detector. Diffraction intensity measurements were made for four hkl peaks (111, 200, 220, 311) in five directions, the three principal directions: the rolling direction (RD), the transverse direction (TD) and the normal direction (ND) and two more in the RD-ND plane at 30 and 60 degrees from the RD. The directions RD, TD and ND are the exact equivalents of the principal directions x , y and z in the PXM method. Two wavelengths were used to keep the range of 2θ (PHI) angles small. For the {111} and {200} measurements the wavelength (λ) was 2.37\AA and for the {220} and {311} measurements $\lambda = 1.51\text{\AA}$. A Ge monochromating crystal was used.

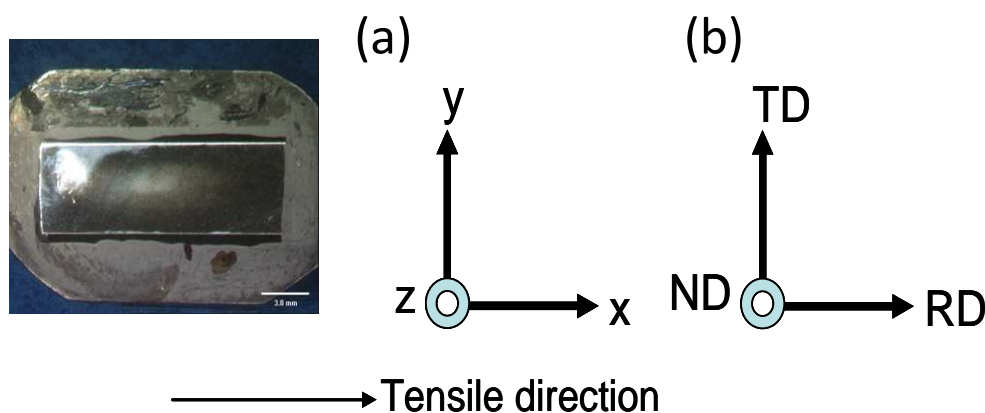


Figure 2.4 The photograph shows the sample orientation with respect to the coordinate systems of: (a) PXM measurements and (b) neutron diffraction measurements.

The unstrained lattice parameter $d_0 = 0.35564 \pm 0.00004$ nm is determined from the neutron diffraction pattern of the Alloy 600 control sample (no tensile stress applied). This value is the average of the lattice parameter values calculated from all the measured d-spacings for the control sample (five values for four types of hkl planes). The uncertainty is the sum in quadrature of the standard deviation of the values and the average uncertainty of the values, which arises from the peak fitting and wavelength

calibration. The PXM and neutron diffraction data were all processed using this as the reference lattice spacing. The sample tensile directions with respect to the coordinate systems of the PXM and neutron diffraction measurements are shown in Figure 2.4.

2.6 Other Instruments

Optical microscopy was performed using Zeiss Axioplan Compound Microscope and Zeiss Discovery V8 Stereomicroscope at Surface Science Western (SSW). Scanning electron microscopy (SEM) coupled with energy dispersive X-ray analysis (EDX or EDS) was performed using Hitachi S-5400 FESEM equipped with Quartz XOne EDX system at SSW and the LEO (Zeiss) 1540XB FIB/SEM at the Western Nanofabrication Facility.

Chapter 3

3. Comparisons of Polychromatic X-ray Microdiffraction (PXM) with Neutron Diffraction and Electron Backscatter Diffraction (EBSD)

As discussed in Chapter 1, the major objective of our study is to determine the micro-strain distribution in Alloy 600 prior to and during the SCC initiation using the PXM method. The first step was to assess the reliability of PXM method for the measurement of the magnitude and distribution of mechanical strains in Alloy 600. PXM data will be compared to that from neutron diffraction and EBSD. In this chapter, PXM, neutron diffraction and EBSD measurements were made on samples of the alloy that had been stressed uniaxially. Contents presented in this chapter are excerpted from a previously published paper and a progress report [82-84].

3.1 Brief Review of Experimental (Samples & Techniques)

Samples studied came from a bar of Alloy 600, described in Chapter 2, that had been machined into tensile test specimens. These test specimens had been uniaxially stretched to 0%, 1% and 10% extensions; the 0% sample served as an “as received” (control) reference. The end-bar tensile sample and mid-bar tensile sample were respectively cut from the end and the middle part of 1% extension bar, which is actually plastically strained to 0.5% (refer to Figure 2.1). The samples to be analyzed by various techniques were cut from these test specimens and their surfaces prepared using methods described in Chapter 2. 2D PXM scans were run on all samples and one in-depth (3D) scan was carried out for the end-bar strained sample at APS. All measurements were carried out on areas denoted by Au or Pt metal fiducial marks. Neutron diffraction measurements were made on the control and end-bar strained samples, while EBSD measurements were only carried out on the mid-bar strained sample. The PXM patterns collected from the 10% extension sample was found to be unindexable, as there was extensive plastic deformation produced in this sample.

3.2 Results and Discussion

3.2.1 PXM Elastic Strain Results

2D PXM scans were collected from the control and end-bar 1% strained samples, using an x-ray beam spot size of $1 \times 1 \mu\text{m}^2$ and a step size (lateral resolution) of $2 \mu\text{m}$. The PXM data was indexed using lattice parameter $d_0 = 0.35564 \pm 0.00004 \text{ nm}$ obtained from the control sample analyzed by neutron diffraction. The resulting orientation and strain maps are shown in Figures 3.1 and 3.2, respectively. In the orientation map different colors represent different orientations with respect to a chosen directional pole (in this case [111]). The orientation of grains can be identified from the color legend. In the strain map, a strain scale from -5 to $5 (\times 10^{-3})$ is adopted, corresponding to a color scale from deep blue (most compressive) to red (most tensile). Areas with a green color are relatively strain free. Some black areas are seen, resulting from non-indexing, which is mostly due to the existence of high plastic deformation or the confusion of the indexing process because of several overlapping grains. Also shown is a plot of “von Mises (VM) strain” for each area studied.

Inspection of the principal deviatoric strain component maps from the control and the end-bar samples (Figures 3.1 and 3.2) clearly shows lower strain in the control strain component maps compared to the end-bar strained sample. The VM maps also register this difference. Closer inspection of the 2D strain components for the end-bar strained specimen (Figure 3.2) shows compressive strain for the xx component (ε_{xx}) of many grains and tensile strain for some of the zz component (ε_{zz}).

An in-depth (3D) $44 \mu\text{m}$ line scan with lateral resolution of $2 \mu\text{m}$ and depth resolution of $1 \mu\text{m}$ was also collected from the end-bar 1% strained sample within the 2D scanned area (see blue line in Figure 3.2). The 3D map probes to a depth of over $60 \mu\text{m}$ into the bulk material. The resulting in-depth orientation map and corresponding strain maps are shown in Figure 3.3. Again, most grains exhibit compressive ε_{xx} strains. There is no measurable difference in the elastic strain magnitudes or directions from the surface region to the interior; however surface/bulk differences in dislocations are shown later.

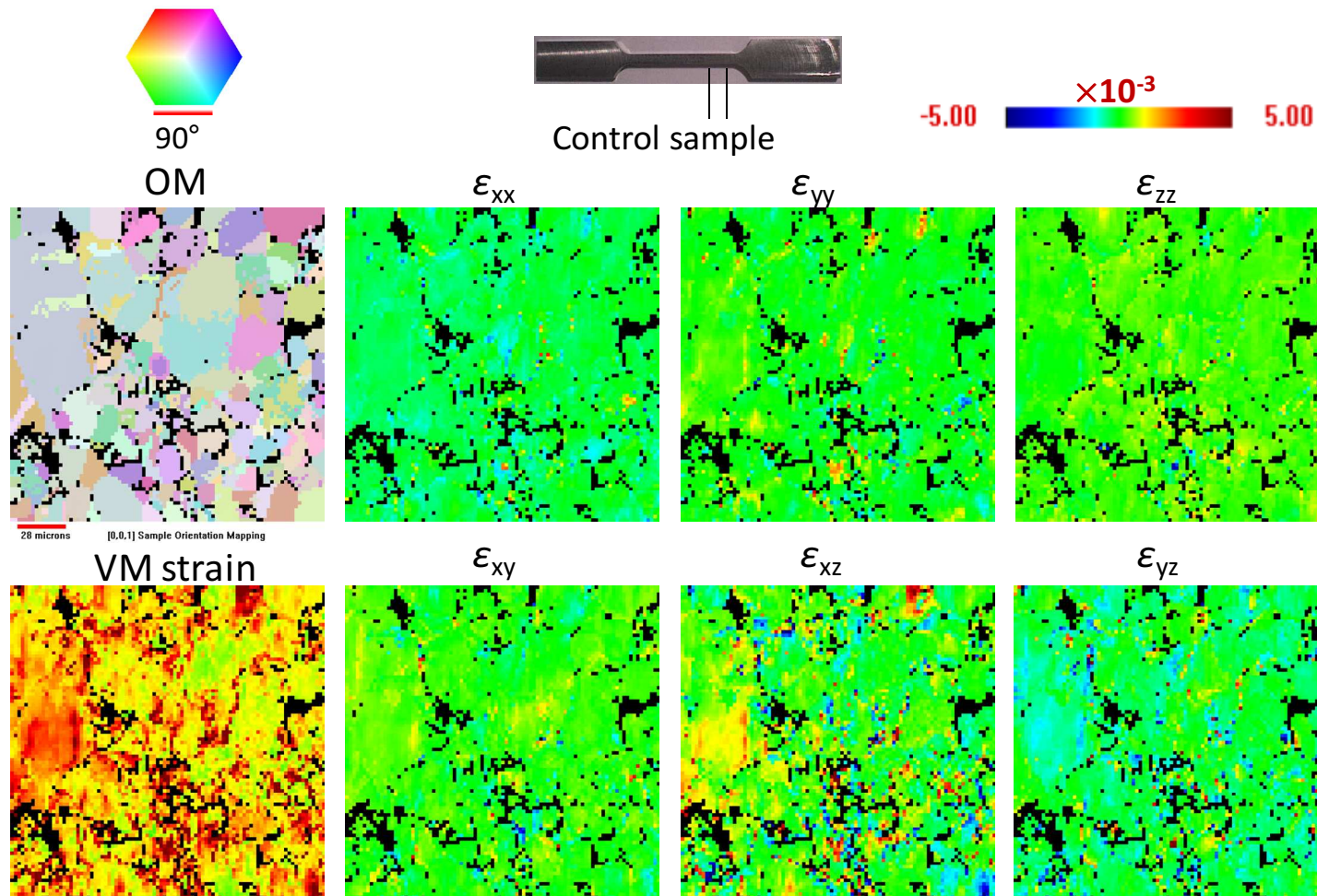


Figure 3.1 Orientation map and deviatoric strain component maps of the control sample from 2D PXM. The field of the diffraction patterns comprises an area of $180 \times 180 \mu\text{m}^2$. The color legend for OM is on the top of the OM map, while the color legend with a scale of -5 to 5 ($\times 10^{-3}$) for all strain maps is shown at the right corner.

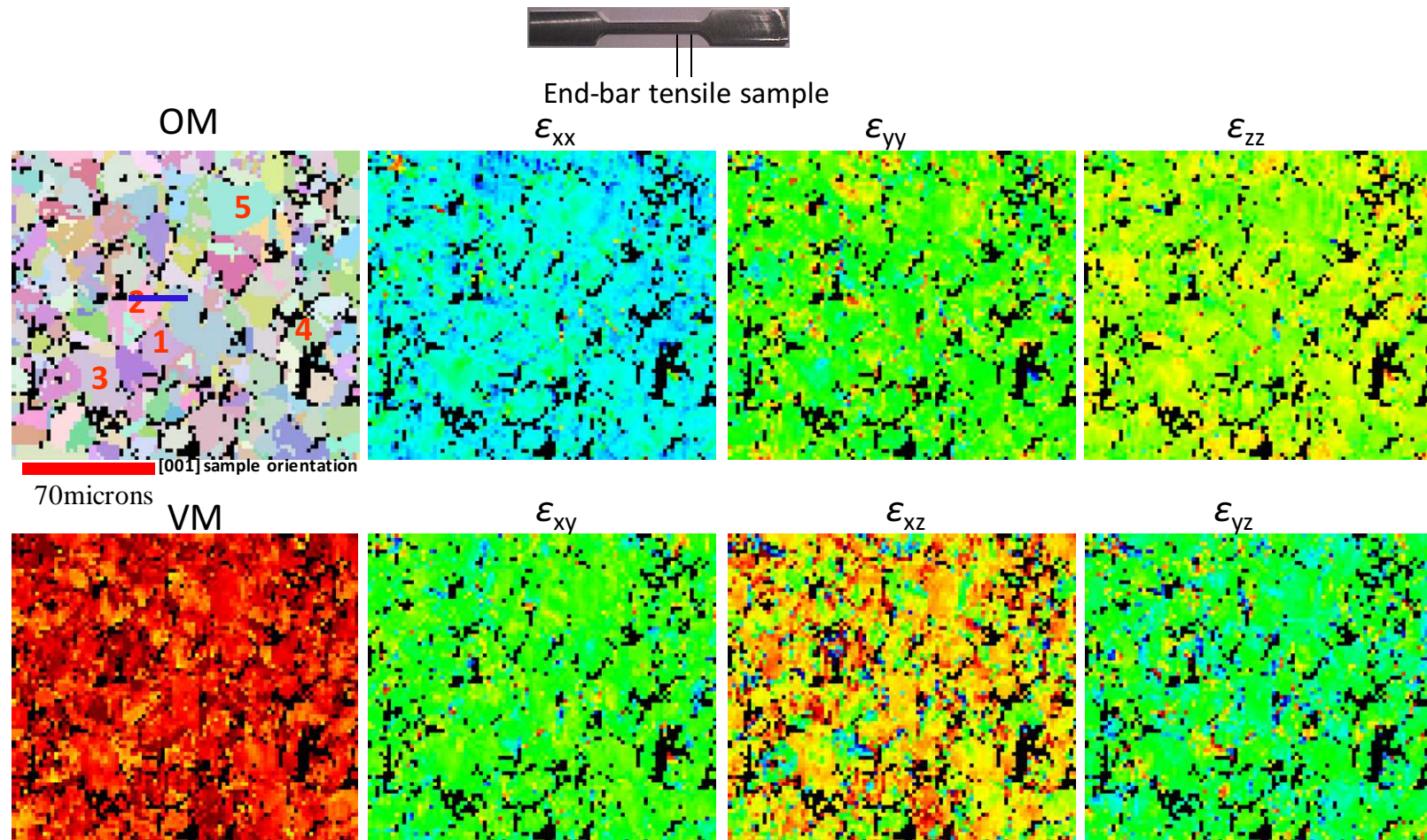


Figure 3.2 Orientation map and deviatoric strain component maps of the end-bar tensile sample from 2D PXM. The field of the diffraction patterns comprises an area of $180 \times 160 \mu\text{m}^2$. The color legends for OM and strain maps are the same as in Figure 3.1. The blue line across grain 2 in the OM indicates the position for the 3D PXM scan. The numbers in OM indicate 5 grains for later comparison with neutron diffraction.

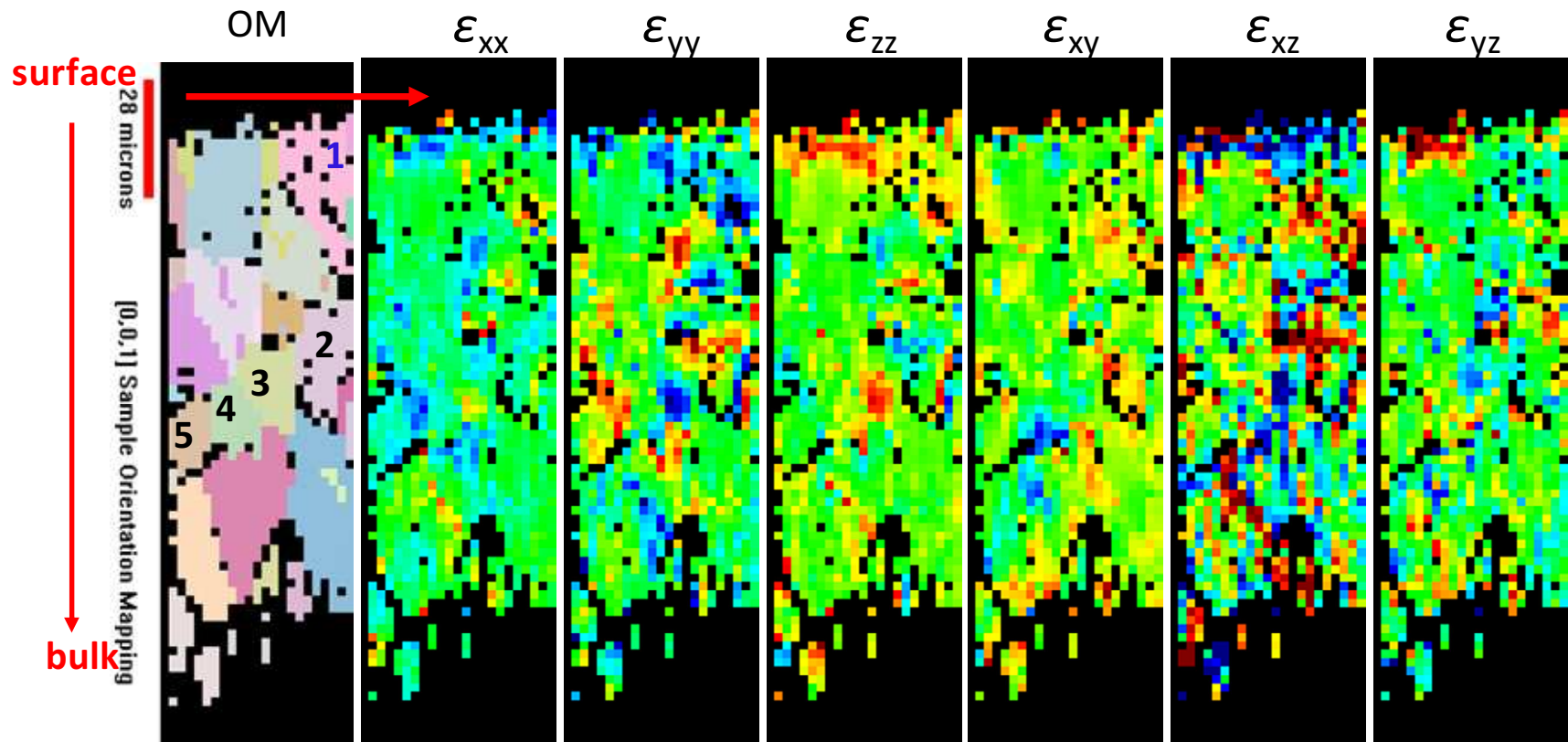


Figure 3.3 Orientation map (OM) and strain maps of 3D PXM scan from the end-bar sample. Refer to Figure 3.1 for the color legend of OM and strain maps. The numbers in OM indicate 5 selected grains for later comparison with neutron diffraction.

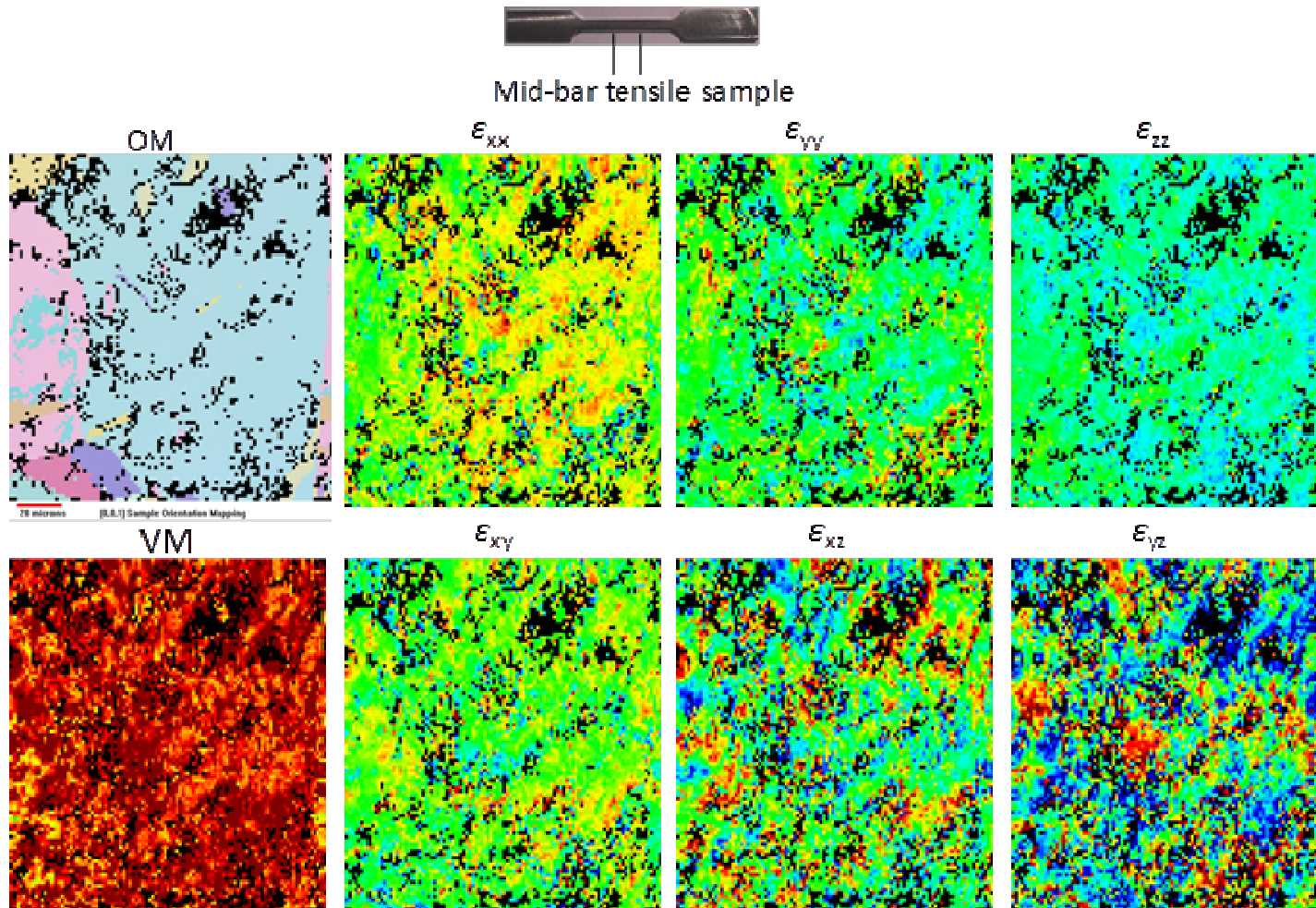


Figure 3.4 Orientation map and deviatoric strain component maps of the mid-bar tensile sample from 2D PXM. The field of the diffraction patterns comprises an area of $200 \times 200 \mu\text{m}^2$. The color legends for the OM and strain maps are the same as in Figure 3.1.

2D PXM scans were also collected from the mid-bar strained sample in March 2007 at APS. Figure 3.4 shows the resulting orientation map and strain maps. This region had a grain structure quite different from the relatively regular grain size of the end-bar and the control samples; the orientation image in Figure 3.4 is dominated by one or more large grains surrounded by a cluster of smaller ones.

According to the color scale, the two strained samples in Figures 3.2 and 3.4 obviously have bigger VM strain than the control sample in Figure 3.1, which matched the expected results. It is also noted that mid-bar sample shows bigger VM strain than the end-bar sample.

Table 3.1 listed the average strain for the scanned area of all samples. It is important to note the degree to which even small compressive and tensile elastic strains are able to be differentiated by PXM. Such elastic strain cannot be measured by EBSD; therefore PXM has a major advantage in the study of SCC cases where strain direction can indicate the probability of a subsequent mechanical failure.

Table 3.1 Average deviatoric strain (elastic strain) for the PXM scanned area of control, end-bar and mid-bar strained samples.

$\times 10^{-3}$		ϵ_{xx}	ϵ_{yy}	ϵ_{zz}	ϵ_{xy}	ϵ_{xz}	ϵ_{yz}	ϵ_{VM}
control		-0.30	0.03	0.27	0.19	0.20	-0.28	1.98
End-bar	2D	-1.00	0.29	0.72	0.15	1.22	-0.12	3.71
	3D	-0.36	-0.11	0.48	0.47	0.16	0.11	5.04
Mid-bar		0.74	-0.09	-0.65	0.31	-0.26	0.19	5.18

3.2.2 2D PXM Comparison with Neutron Diffraction

The comparison between PXM and neutron diffraction was made on the end-bar strained sample. The reference coordinate systems of PXM and neutron diffraction can be found in Chapter 2 (Figure 2.4). The directions RD, TD and ND in neutron diffraction are the exact equivalent of ϵ_{xx} , ϵ_{yy} and ϵ_{zz} in the PXM method.

Table 3.2 lists the average elastic normal strains along the RD, TD, and ND as measured by neutron diffraction on the end-bar sample. Listed in this table are the average normal strains calculated from the angular diffraction peak shifts of four planes

aligned along each of the RD, TD, and ND directions. The uncertainties in the calculated strain values are large and may be partly caused by uncertainty in the peak fits and from wavelength calibration. For any given direction in the material, the normal strain along that direction is different for the different crystal systems, i.e., (200) compared to (220) or (111) (Table 3.2). This reflects the elastic anisotropy of this polycrystalline Alloy 600 [85].

Table 3.2 Strain measurements for the end-bar sample using neutron diffraction.

Direction	<i>hkl</i>	Strain ($\mu\epsilon$)
RD	111	-134 ± 142
	200	-140 ± 132
	220	-63 ± 137
	311	-112 ± 132
ND	111	-112 ± 273
	200	466 ± 254
	220	128 ± 114
	311	-25 ± 136
TD	111	-34 ± 244
	200	135 ± 189
	220	-199 ± 148
	311	-53 ± 108

PXM (Figure 3.2) had observed compressive ϵ_{xx} strains for most orientations, while the normal strains measured from the four planes parallel to the RD in neutron results are all compressive. Thus, the PXM result is confirmed by neutron diffraction from a qualitative point of view. For a more precise comparison between specific neutron measurements and the Laue measurements for individual grains, crystal rotation matrices were used to determine the angular relationships between specific $\langle hkl \rangle$ directions in the grains and the measurement directions used in neutron diffraction. Five grains were selected for comparison with the neutron diffraction results (numbered 1 to 5 in the Figure 3.2). The principal strains ϵ_{xx} , ϵ_{yy} , and ϵ_{zz} , correspond to the RD, TD, and ND of the sample respectively. Table 3.3 gives the averaged strain values from the five grains identified in Figure 3.2. Directions of planes with a low angle to one of the principal directions were used for comparison. These directions for each of the five selected grains are underlined in Table 3.4. For these five grains, the appropriately oriented principal deviatoric strain component values from PXM, averaged over the grain, were compared to neutron diffraction strain measurements, averaged over many

grains, with one direction in common. For example, if a particular plane direction (from all measured plane directions) from PXM shows the lowest angle to the ND, the neutron diffraction strain measurement for that plane direction oriented in the ND is compared to the principal strain component measurement, ϵ_{zz} , for that grain. The results are shown in Table 3.5. The uncertainties for PXM strain data were calculated as the standard deviation of the strain values from all the data points within the corresponding grain used for the average strain calculation.

Table 3.3 Averaged strain values from the whole grain for the 5 selected grains in the 2D PXM map.

Whole grain($\mu\epsilon$)	G1	G2	G3	G4	G5
ϵ_{xx}	-1038 \pm 285	-1225 \pm 464	-715 \pm 218	-1224 \pm 223	-1073 \pm 333
ϵ_{yy}	426 \pm 415	834 \pm 784	-180 \pm 376	263 \pm 341	457 \pm 402
ϵ_{zz}	614 \pm 421	394 \pm 361	896 \pm 188	962 \pm 225	618 \pm 180

Table 3.4 Calculated orientations for Grains 1-5 of the end-bar sample from 2D PXM data to RD, TD, ND.

Grain	Direction	RD	TD	ND
1	$\langle 200 \rangle$	59.8	30.4	86.7
	$\langle 220 \rangle$	79.7	80.2	<u>14.3</u>
	$\langle 111 \rangle$	81.7	50.5	40.7
	$\langle 311 \rangle$	67.8	31.5	68.8
2	$\langle 200 \rangle$	56.4	36.3	77.8
	$\langle 220 \rangle$	67.2	88.6	<u>22.8</u>
	$\langle 111 \rangle$	89.8	61.0	29.0
	$\langle 311 \rangle$	61.4	58.9	44.7
3	$\langle 200 \rangle$	67.1	84.3	23.6
	$\langle 220 \rangle$	89.8	<u>6.3</u>	83.7
	$\langle 111 \rangle$	58.2	84.6	32.4
	$\langle 311 \rangle$	48.2	60.4	56.0
4	$\langle 200 \rangle$	74.8	61.8	32.7
	$\langle 220 \rangle$	81.2	81.0	<u>12.7</u>
	$\langle 111 \rangle$	52.5	79.2	39.6
	$\langle 311 \rangle$	34.6	64.8	67.9
5	$\langle 200 \rangle$	83.2	27.5	63.5
	$\langle 220 \rangle$	67.9	72.1	29.0
	$\langle 111 \rangle$	77.6	78.6	<u>17.0</u>
	$\langle 311 \rangle$	87.7	50.3	39.8

Table 3.5 Strain from the 5 selected regions from 2D PXM and neutron results for the end-bar sample.

Region	Strain direction	Measured neutron strain($\mu\epsilon$)	Measured Laue strain($\mu\epsilon$)
1	ND $\langle 220 \rangle$	128 \pm 114	$\epsilon_{zz} = 614 \pm 421$
2	ND $\langle 220 \rangle$	128 \pm 114	$\epsilon_{zz} = 394 \pm 361$
3	TD $\langle 220 \rangle$	-199 \pm 148	$\epsilon_{yy} = -180 \pm 376$
4	ND $\langle 220 \rangle$	128 \pm 114	$\epsilon_{zz} = 962 \pm 225$
5	ND $\langle 111 \rangle$	-112 \pm 273	$\epsilon_{zz} = 618 \pm 180$

Grains 1, 2 and 4 exhibit similar strain patterns (all tensile in z direction or ND). The neutron diffraction measurements indicate that the tensile strain in ND occurs for grains with $\langle 220 \rangle$ oriented to ND. Grain 1, 2 and 4, in fact, have a $\langle 220 \rangle$ that is close to the ND (14, 23 and 13 degrees off respectively) and the principal deviatoric strain component in the z direction from PXM does in fact show tensile strain. However, the neutron diffraction and PXM strain results from Grain 4 do not fall within the uncertainty. Grain 3 has the lowest angle with the $\langle 220 \rangle$ in the TD (6 degrees). Neutron results indicate that the $\langle 220 \rangle$ is compressive in the TD and the PXM results indicate compressive strain in the principal y direction. Grain 5 has the lowest angle in the principle z direction with $\langle 111 \rangle$, which seems not to correlate with the neutron result. Neutron results indicate that grains with $\langle 111 \rangle$ parallel to ND show compressive strain and the PXM results indicate tensile strain in z direction. 2D PXM results thus correlate well with the neutron results in 3 of the 5 cases described above.

3.2.3 3D PXM Comparison with Neutron Diffraction

The levels of strain from neutron diffraction were on the order of 100×10^{-6} ($100 \mu\epsilon$) and agree with the levels of strain measured by 3D PXM (Figure 3.3). Neutron diffraction results indicated compressive strain in the RD for the measured specific lattice strains (see Table 3.2). Inspection of the principal deviatoric strain component map (Figure 3.3) in the tensile or x-direction (ϵ_{xx}) reveals largely compressive strain across many grains. Again, the same comparison as the 2D PXM has been done for 3D PXM in the grains and the measurement directions used in neutron diffraction (refer to Figure 2.4 for comparison of reference coordinate systems). Five grains from the 3D PXM results exhibiting higher levels of strain were selected for comparison with the neutron results. These 5 grains are labeled in the PXM orientation map shown in Figure 3.3. Calculated orientations of the four directions (111, 200, 220, 311) for the 5 selected grains from the 3D PXM measurements (refer to Figure 3.3) to RD, TD and ND are shown in Table 3.6.

Directions of planes with a low angle to one of the principal directions were used for comparison. These directions are highlighted in red in Table 3.6. For these 5 grains,

the appropriately oriented principal deviatoric strain component values from PXM, averaged over the grain, were compared to the neutron diffraction strain measurements, averaged over many grains, with one direction in common. Large variations in strain values across the grains were noted during the PXM measurements which are reflected in the uncertainties. The results are shown in Table 3.7.

Table 3.6 Calculated orientations for Grains 1-5 from 3D PXM data to RD, TD, ND system.

Grain	Direction	RD	TD	ND
1	$\langle 200 \rangle$	75.6	66.2	28.2
	$\langle 220 \rangle$	63.8	48.3	53.0
	$\langle 111 \rangle$	89.8	62.9	27.0
	$\langle 311 \rangle$	70.2	43.1	53.6
2	$\langle 200 \rangle$	88.3	9.1	81.0
	$\langle 220 \rangle$	77.9	53.1	39.5
	$\langle 111 \rangle$	68.0	63.6	35.6
	$\langle 311 \rangle$	77.7	34.1	58.7
3	$\langle 200 \rangle$	60.8	75.1	33.5
	$\langle 220 \rangle$	42.4	67.2	56.6
	$\langle 111 \rangle$	71.3	80.4	21.2
	$\langle 311 \rangle$	47.1	82.8	43.8
4	$\langle 200 \rangle$	45.9	45.1	45.6
	$\langle 220 \rangle$	74.2	84.7	16.7
	$\langle 111 \rangle$	79.7	61.1	31.0
	$\langle 311 \rangle$	59.1	47.3	58.2
5	$\langle 200 \rangle$	66.2	26.8	78.4
	$\langle 220 \rangle$	73.3	36.4	58.7
	$\langle 111 \rangle$	89.3	64.1	26.0
	$\langle 311 \rangle$	75.6	39.9	53.8

Table 3.7 Strain from Grains 1-5 from the 3D PXM and neutron results for the end-bar sample.

Grain	Strain direction	Measured neutron strain($\mu\epsilon$)	Measured Laue strain($\mu\epsilon$)
1	ND $\langle 200 \rangle$	466 ± 254	$\epsilon_{zz} = 936 \pm 1045$
	ND $\langle 111 \rangle$	-112 ± 273	
2	TD $\langle 200 \rangle$	135 ± 189	$\epsilon_{yy} = 556 \pm 1677$
3	ND $\langle 200 \rangle$	466 ± 254	$\epsilon_{zz} = 1134 \pm 1123$
	ND $\langle 111 \rangle$	-112 ± 273	
4	ND $\langle 220 \rangle$	128 ± 114	$\epsilon_{zz} = 619 \pm 691$
5	TD $\langle 200 \rangle$	135 ± 189	$\epsilon_{yy} = 906 \pm 646$
	ND $\langle 111 \rangle$	-112 ± 273	$\epsilon_{zz} = 40 \pm 468$

Grains 1 and 3 are oriented similarly and exhibit similar strain patterns. In the table, ND has almost the same angles with both $\langle 200 \rangle$ and $\langle 111 \rangle$. Neutron results indicate that grains with $\langle 200 \rangle$ parallel to ND show very high tensile strain ($466\mu\epsilon \pm 254$), while grains with $\langle 111 \rangle$ show compressive strain ($-112\mu\epsilon \pm 273$). In total, if grains

are oriented between these two directions, they should still show tensile strain ($466 > 112$).

Grain 2 exhibits high tensile strain in the y or TD direction, which correlates with the neutron diffraction results. The neutron diffraction measurements indicate that the high tensile strain in TD should occur when grains with $\langle 200 \rangle$ oriented to TD. Grain 2, in fact, has $\langle 200 \rangle$ that is close to the TD (9 degrees off) and the principal deviatoric strain component in the y direction from PXM does in fact show tensile strain.

Grain 4 has the lowest angle with the $\langle 220 \rangle$ in the ND. Neutron diffraction results indicate that the $\langle 220 \rangle$ is tensile in the ND and the PXM results indicate tensile strain in the principal z direction.

Grain 5 shows tensile strain in the y or TD direction, and compressive strain in the z or ND direction (Figure 3.3). From the angle conversion shown in Table 3.6, TD has the lowest angle with $\langle 200 \rangle$ and ND has a similar low angle with $\langle 111 \rangle$. Neutron diffraction results indicate tensile strain of $\langle 200 \rangle$ in the TD and compressive strain of $\langle 111 \rangle$ in the ND.

The neutron diffraction and 3D PXM strain measurements agree within uncertainty. It should also be recalled that Laue measures only deviatoric strain while neutron diffraction measures total strain.

3.2.4 PXM Comparison with EBSD

The comparison between PXM and EBSD was made on the mid-bar strained sample. In Figure 3.5, the orientation maps obtained by PXM and EBSD are compared. Grain boundary patterns obtained are, at first glance, quite similar although the spatial resolution of EBSD is superior. However, some small differences between the orientation maps (OMs) are noted. Some of the small, thin grains shown in the EBSD orientation map are not visible in the PXM orientation map; this is likely due to differences between the spatial resolutions of the two techniques. As well, the large grain on the left of the PXM orientation map (pink grain) exhibits features (regions in blue color) which are not observed seen in the orientation map from EBSD. It should again be

mentioned that PXM detects material to much greater depths than EBSD and these blue regions most likely arise from an underlying grain.

Composite strain maps of the above-mentioned region, obtained by PXM and EBSD, are compared in Figure 3.6. For PXM, composite elastic strain is calculated from all elastic strain component values using the VM formula; for EBSD the composite strain is determined from the measured area density of low angle lattice mis-orientations relative to those measured in standard strained samples- effectively measure of plastic, not elastic strain. From a close inspection of both images, it is not possible to see much similarity. Some high strain features appear common to both, such as in regions A, B, C, and D. Other high strain regions do not coincide in both images. While some of the disaccord may result from differences in depths sampled by the two techniques, the main difference likely stems from the fact that the strains mapped by PXM are largely residual elastic while those from EBSD are completely plastic.

PXM data were also used to assess qualitatively the range of local plastic deformation within region A in the upper left hand corner of the image field in Figure 3.7, Laue patterns are shown for locations having (a) high elastic strain (24×10^{-3}), (b) low elastic strain (3.4×10^{-3}), (c) near the grain boundary (3.8×10^{-3}) and at the grain boundary (3.7×10^{-3}). Some dislocation walls are detected in the high elastic strain and none in the adjacent low elastic strain region. However, most of the plastic deformation is found in the vicinity of the grain boundary, as also can be seen in the EBSD map.

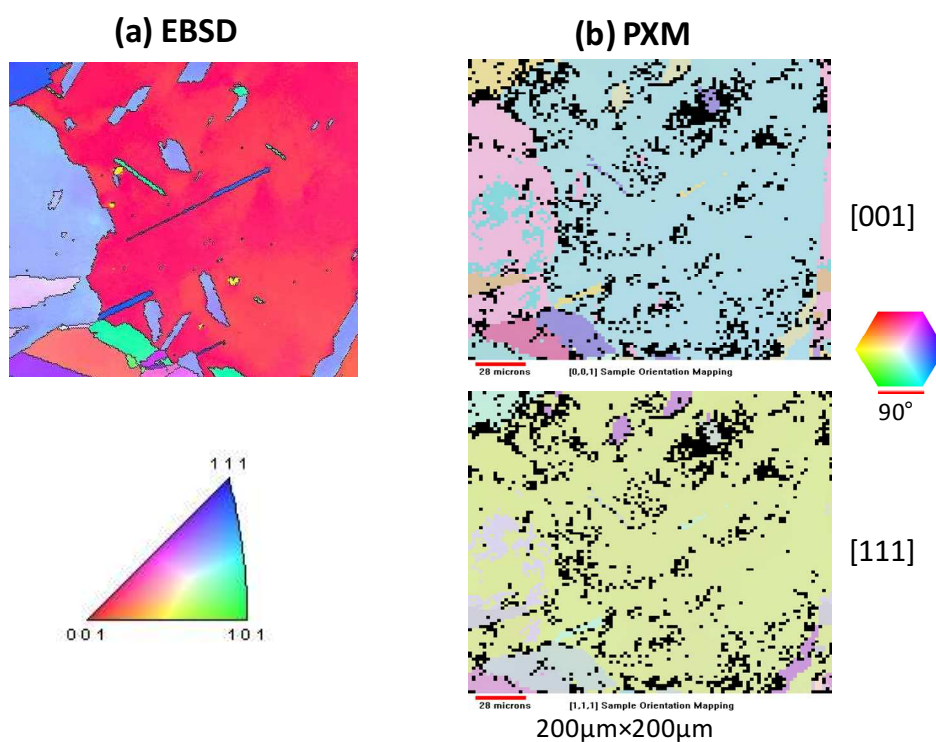


Figure 3.5 Comparison of (a) EBSD and (b) PXM orientation maps for the mid-bar sample. The PXM results are plotted for two different directions. The pole figure grain orientation is denoted by color and the orientation can be determined from the color legend.

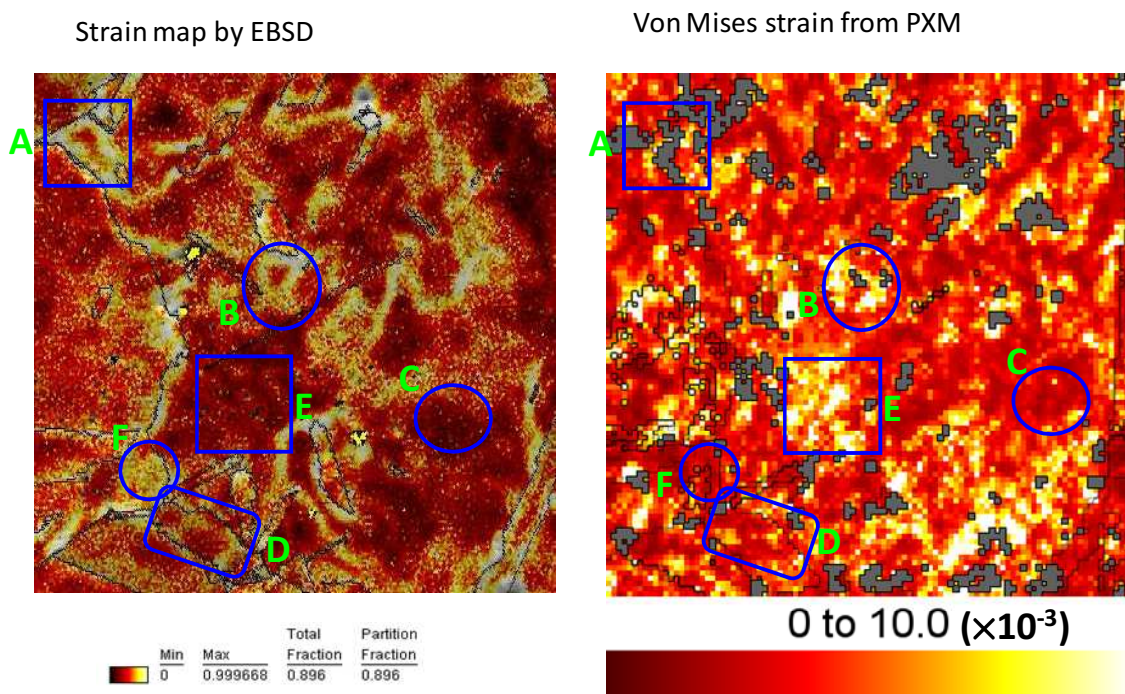


Figure 3.6 Comparison of PXM and EBSD composite strains for the mid-bar sample.

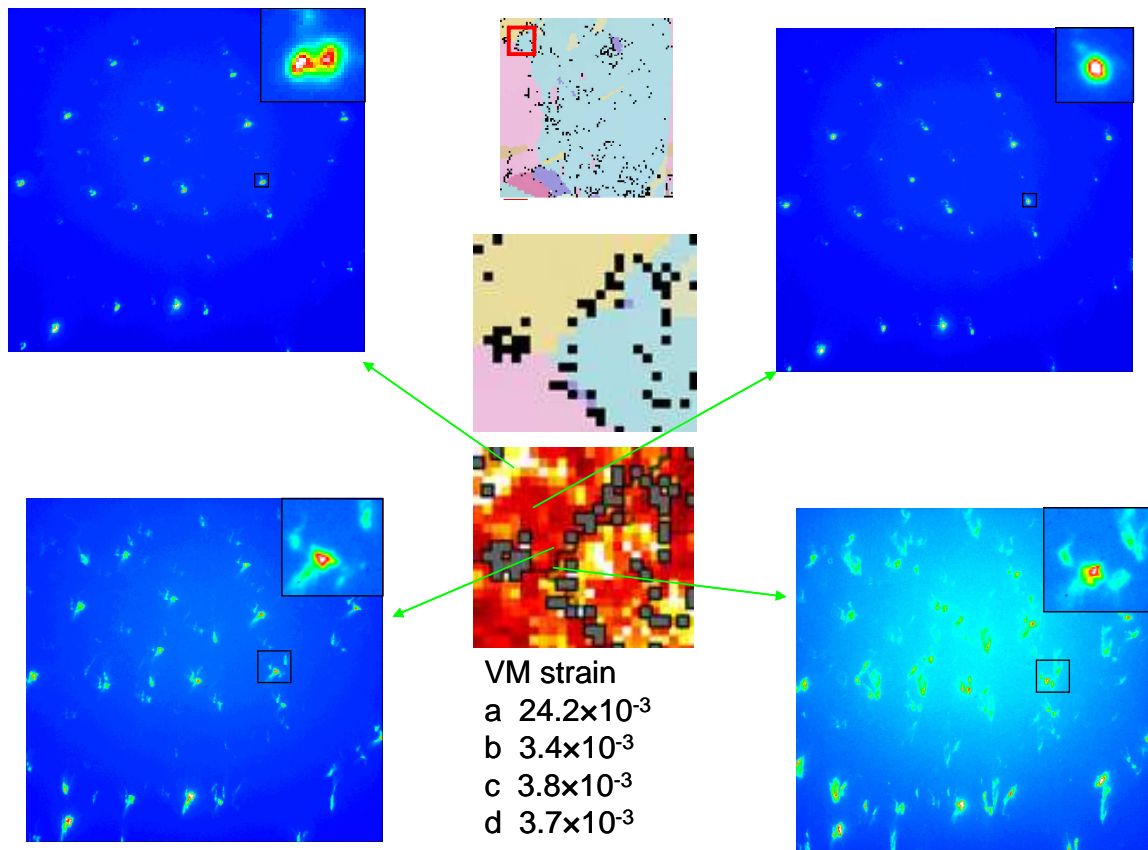


Figure 3.7 Laue patterns for four different pixels from the same grain within the map for the mid-bar sample: (a) pixel from an area of high elastic strain; (b) pixel from an area of low elastic strain; (c) pixel close to the grain boundary; (d) pixel on the grain boundary.

3.3 Summary

Both 2D and 3D PXM strain information for a 0.5% plastically strained sample (end-bar sample) has been compared to that obtained using neutron diffraction. The principal strain directions in the alloy were determined to have mostly compressive strains that were on the order of 100×10^{-6} ($100\mu\epsilon$); this agrees with the levels of strain measured in individual grains by PXM. The comparison between neutron diffraction results and PXM involved an identification of grains in the PXM strain maps whose directions come closest to the directions measured by neutron diffraction. It must be realized that the neutron diffraction results are an average strain for thousands of grains in the sample while the PXM results are for single grain. Even for a single grain, strain varies across the grain and must be averaged. With these differences in mind and with

the uncertainties in both PXM and neutron diffraction measurements, the agreement of strain magnitude and sign (often within 100%) are acceptably good.

PXM and EBSD measurements were also compared for another region of the 0.5% plastically strained sample (mid-bar sample). The elastic strain distribution, determined by PXM, had some areas that corresponded to the strain distribution measured by EBSD, but most areas did not correspond. This discrepancy results from the origin of the strain data; EBSD derives its information from plastic strain information, while PXM measures the elastic strain directly from lattice parameters.

In short, the results from the PXM are consistent with measurements made by the well-established neutron diffraction and EBSD. Besides, it displays advantages over the two traditional techniques as detailed in Chapter 1.

Chapter 4

4. PXM Results from Tensile Bar Samples

In Chapter 3, the PXM method has been validated for the microstrain measurements of Alloy 600, by comparing with other methods - neutron diffraction and EBSD. To fully understand the capability of the PXM method, this chapter presents the detailed analysis of PXM results from uniaxially stressed samples. The elastic strain study has already been discussed in Chapter 3, so this chapter will focus on plastic deformation analysis. The present content is extracted mainly from a previous written progress report [84].

4.1 Brief Review of Experimental (Samples & Techniques)

Two tensile samples, the mid-bar and end-bar samples, as well as the control sample were studied by PXM at APS. Sample preparation and the experimental setup were described in section 3.1. Note that the mid-bar sample is from the middle part of the tensile stretched bar, while the end-bar sample was cut from the end of the gauge part of the tensile bar. The two samples were electropolished in different ways; details are shown in section 2.2.4.

4.2 Results and Discussions

4.2.1 Elastic Strain Study

2D PXM scans were collected from the control and two tensile samples. The resulting orientation and strain maps have been shown in Chapter 3 (Figures 3.1 - 3.3). As discussed in Chapter 3, the composite (von Mises) strains from the two tensile samples are obviously bigger than that from the control sample (see Table 3.1). Another point we made in Chapter 3 is that the mid-bar sample shows a generally higher strain than that of the end-bar sample; this is likely due to the decreased intensity over which the stress is expressed.

However, there is an indication from the color maps that the strain is somewhat different in different grains and that there is a grain-orientation dependence of the strain. In the mid-bar sample (Figure 3.4), the large grain centered in the OM image shows atypically high tensile strain compared to the mildly compressive strain in the surrounding grains.

4.2.2 Plastic Deformation Study

We have examined the local elastic and plastic strains adjacent to grain boundaries within the end-bar sample. The GB mis-orientation angles between some of the boundaries have been measured and are indicated in Figure 4.1.

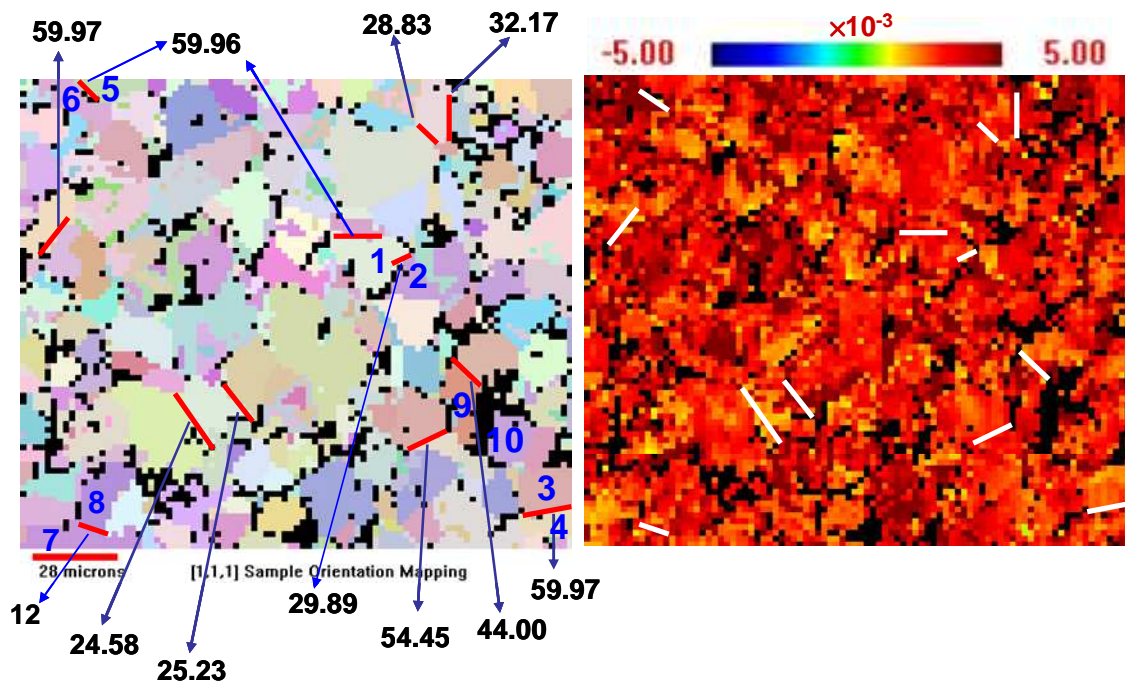


Figure 4.1 Orientation map and von Mises strain map for the end-bar sample. Angular mis-orientations are shown across some of the grain boundaries.

Then, we have looked for relationships between the mis-orientation angles, the elastic strain found on each side of the boundaries, and evidence for dislocations within either grain. The elastic strains are represented as VM strains averaged over the entire grain. The evidence for dislocations and dislocation walls comes from any streaking of the diffraction spots and splitting in the case of dislocation walls [68, 86]. If there happens to be more than one slip system in play the streaks can curl. Splitting of a streak

is evidence of the presence of dislocation walls. The formation of dislocation walls is energetically favored because of the need to minimize the line energy of the dislocations.

In Figure 4.1, a number of different boundary mis-orientations are shown. Five cases are present below in which the diffraction spot shapes in adjacent grains are evaluated with respect to the mis-orientation of the grain boundary and the elastic strain gradients.

Case 1 (see Figure 4.2 below) has a $\Sigma 13b$ ($27.79^\circ \langle 111 \rangle$) CSL grain boundary, according to Brandon's criterion ($\Delta\theta \cong \theta_0 \Sigma^{-1/2}$, where $\theta_0 \cong 15^\circ$) [19]. Grain 1 shows more evidence of dislocations than Grain 2 as indicated by the increased elongation and clear splitting of the diffraction spot particularly near the grain boundary. With very little streaking of the diffraction spots in Grain 2, it appears that dislocations do not pass through this boundary.

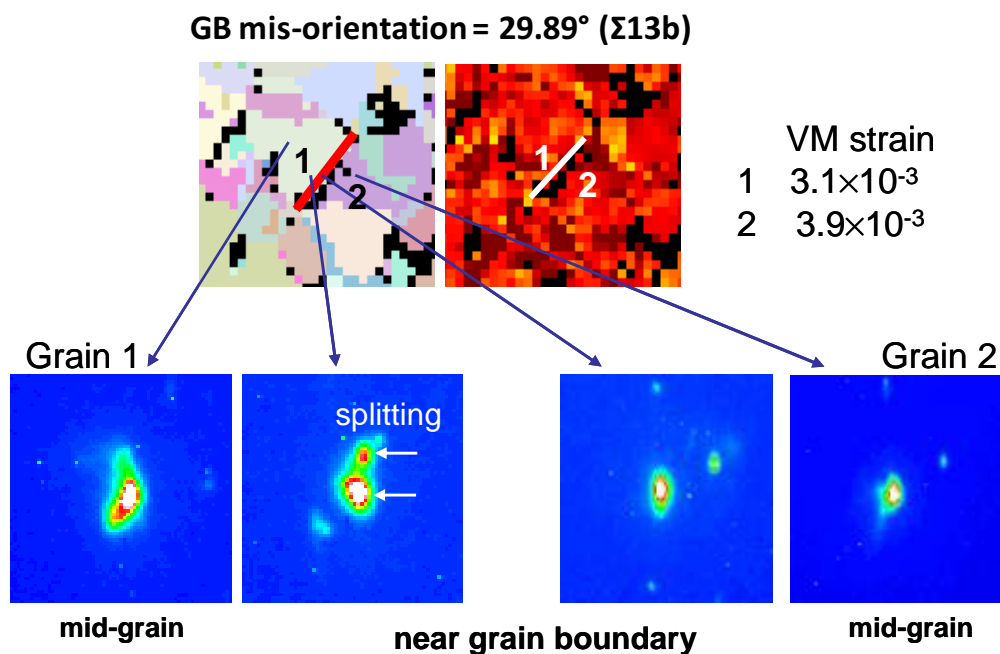


Figure 4.2 Case 1: A $\Sigma 13b$ GB from the end-bar sample. Diffraction spots are streaked in Grain 1 indicating plastic strain, particularly near the GB where the presence of dislocation walls is indicated by the splitting. Grain 2, although having higher elastic strain, shows little evidence of plastic strain.

Case 2 (see Figure 4.3 below) involves a 60 degree ($\Sigma 3$) mis-orientation twin boundary based on Brandon's criterion. In this case, slight streaking is found through both grains; dislocation walls are seen on the Grain 4 side and at least two separate slip systems on the Grain 3 side are seen from curling of the streak. Thus both sides of the twin appear to have comparable densities of dislocations.

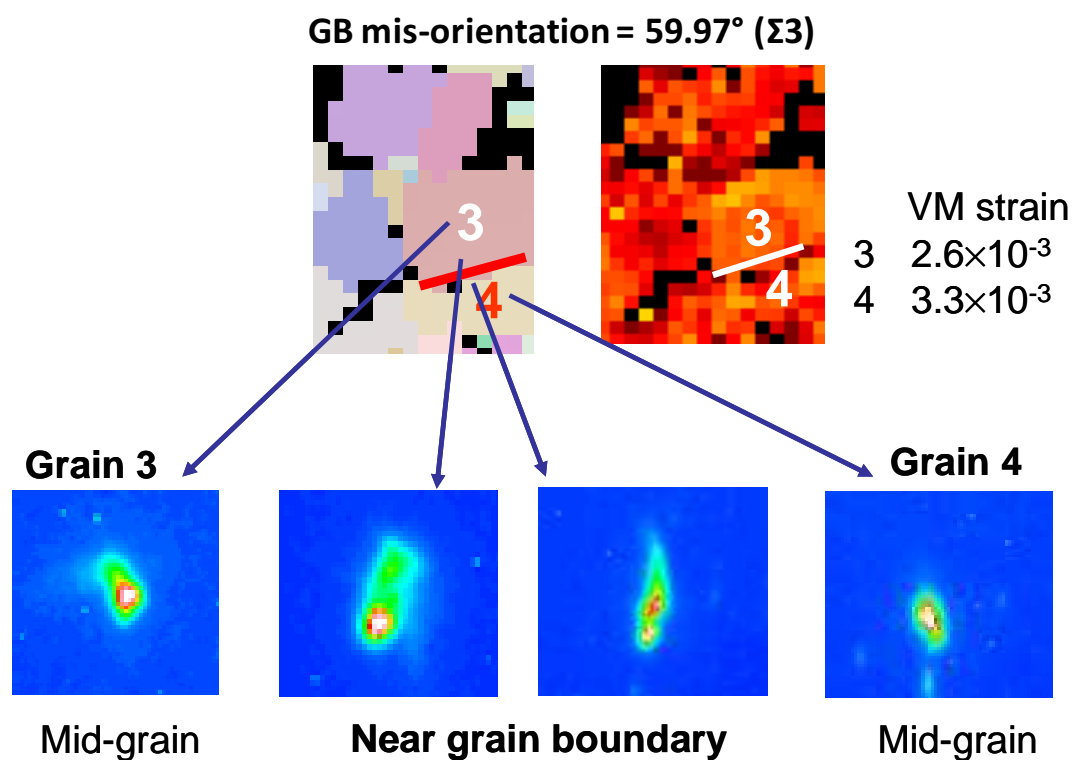


Figure 4.3 Case 2: A 60 degree mis-orientation ($\Sigma 3$) from the 2D PXM data of the end-bar sample. Streaked diffraction spots are found close to the twin boundary on either side, but not near the grain centres.

Case 3 (Figure 4.4 below) also involves 60 degrees ($\Sigma 3$) angular mis-orientation. VM (mostly elastic) strain is twice as great on grain 6 compared to grain 5. Also, splitting of the streaks in both grains on either side of the grain boundary is evident. Streaking occurs in different directions and this indicates that the lattices are bending in different directions in the two grains. Based on the shape of the diffraction spots, it can be qualitatively mentioned that there appears to be no big difference in plastic strain distribution on both grains. Therefore dislocations appear to pass through this boundary.

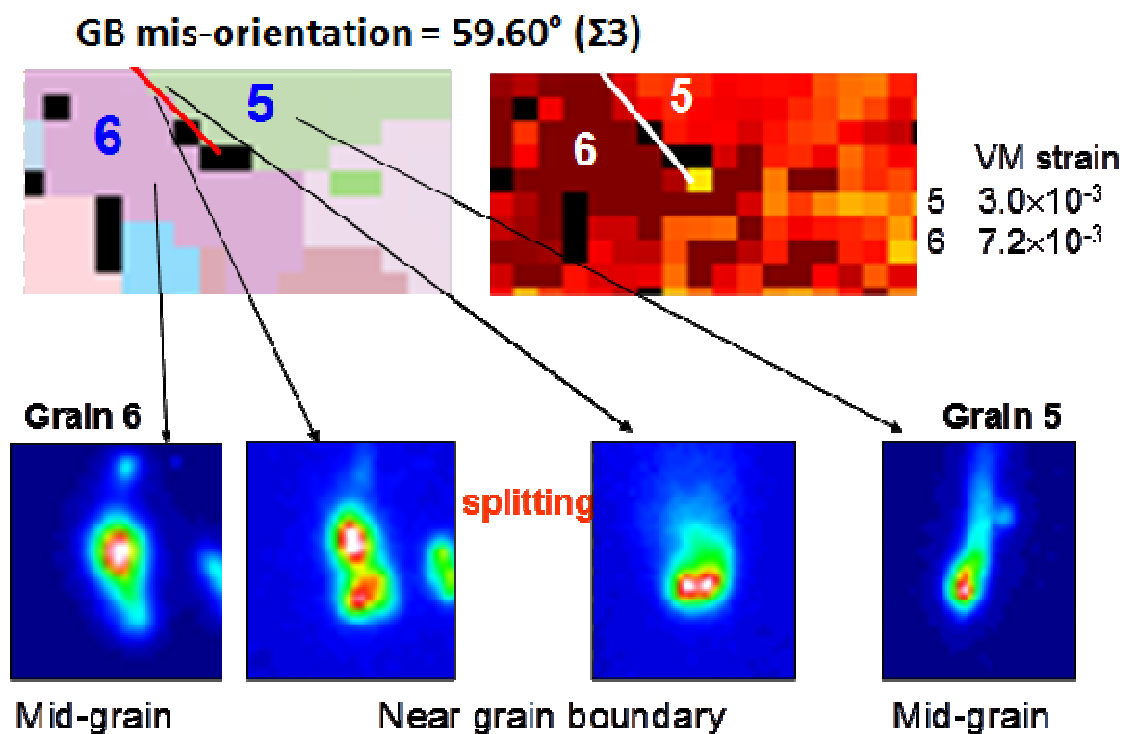


Figure 4.4 Case 3: A 60 degree mis-orientation ($\Sigma 3$). Dislocations are found on both sides of the twin boundary.

Finally, in Case 5 (Figure 4.6 below), the nature of dislocations was investigated in the vicinity of the sample where the high dislocation density resulted in heavily distorted diffraction patterns that were difficult to index. It is not possible to determine the angular mis-orientation between the Grain 9 and 10 due to the heavily distorted crystal structure at the boundary. Although the elastic strains in the two grains are similar, as indicated by the similar magnitudes of VM strain, there is a major difference in the degree of elongation of the diffraction spots on either side of the boundary. Grain 10 has significantly more elongation and splitting (see image d in particular) indicating the formation of significant dislocation cell walls than Grain 9. This situation probably occurs because the mis-orientation between the two grains suppresses the nucleation of geometrically necessary dislocations in Grain 9. The situation depicted in Figure 4.6 illustrates the considerable lattice bending that results from local dislocation build up with a “soft” grain that is favorably oriented for slip. The high local dislocation density at certain high angle grain boundaries is thought to be the primary precursor for the initiation of intergranular stress corrosion cracking in Alloy 600 during service in a high temperature aqueous environment. In this particular case it appears as if grain 10 appears close to yielding.

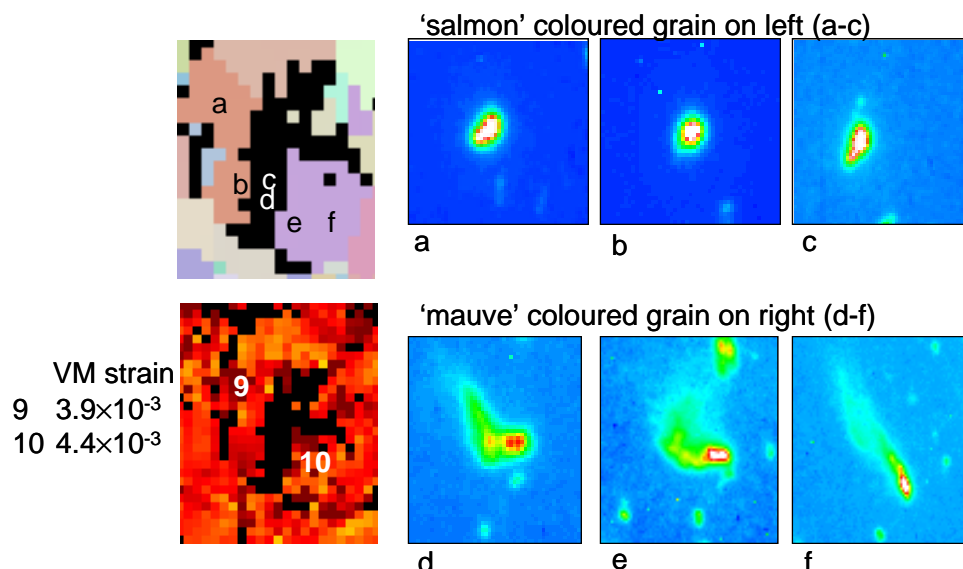


Figure 4.6 Case 5: A boundary whose mis-orientation is not able to be determined. Diffraction spots from the two grains, mid-grain and near the grain boundary are presented. Grain 10 shows significantly more elongation and splitting, indicating the formation of significant cell walls.

It is possible to model the direction of the slip systems associated with the diffraction streaks from grain 10. Seven streaked diffraction spots from Grain 10 were simulated by Dr. R. Barabash of ORNL, shown in Figure 4.7. The simulation modeled the displacement of all atoms in a self-consistent field [68, 86]. The resultant simulation showed that the observed pattern could be well fitted by a plastic flow model with dislocations that glide along two slip systems having the same Burgers vector $\bar{b} = [1\ \bar{1}\ 0]$ and dislocation lines: $\tau_1 = [\bar{1}\ \bar{1}\ \bar{2}]$ and $\tau_2 = [\bar{1}\ \bar{1}\ 2]$ that results in an overall rotation around the $[\bar{1}\ \bar{1}\ 0]$ axes.

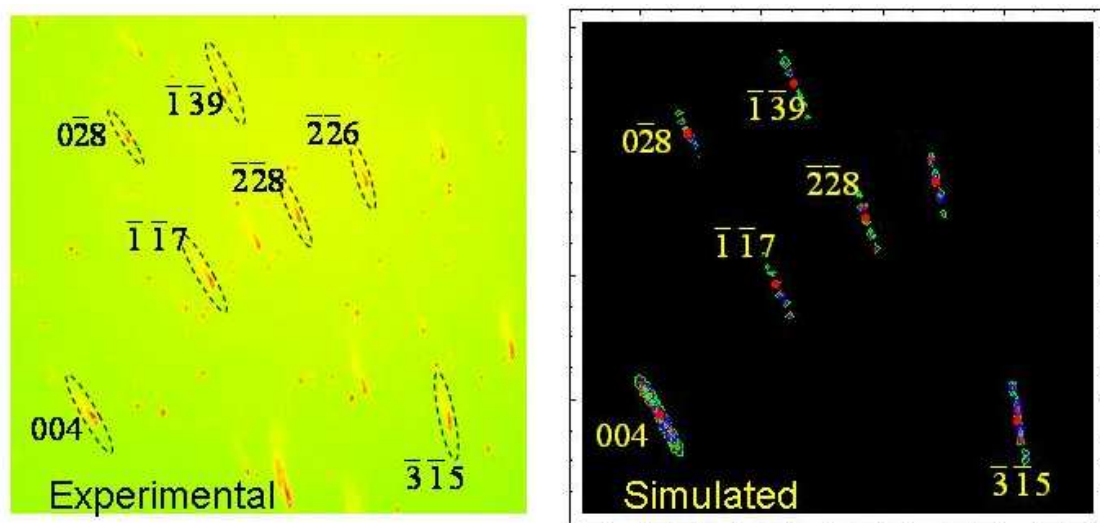


Figure 4.7 Comparison between the experimental pattern and simulated pattern for an area in the 2D map shown in Figure 4.6.

Case 5 shown in Figure 4.6 is a particularly useful working example of PXM abilities to measure the intimate microscopic properties of dislocations in a complex stress field: dislocation directions, dislocation density, the presence of dislocation walls, rotation axes and Burgers vectors can all be determined by a careful assessment of the diffraction spots. EBSD can also identify regions of high dislocations, and from this infer the presence of local plastic strains [87]. However, the strain information available from EBSD is limited to a measure of the dislocation density (with some calibration necessary), and not more intimate properties of the structure that can lead to a complete modeling of systems during crack initiation and propagation.

Cases 1-4 (Figures 4.2 - 4.5) illustrate less strong interactions between grains. Case 1 (Figure 4.2) is a $\Sigma 13b$ boundary with some dislocations within one grain, but not in the adjacent one. According to the theory of Palumbo and Aust [16] the coincident site lattice (CSL) at the boundary for this angle is sufficiently small (low sigma) that it is energetically difficult for dislocations to glide across the boundary. On the other hand, the 60 degree angles between the grains in Cases 2 (Figure 4.3) and 3 (Figure 4.4) could be construed as a $\Sigma 3$ boundary across which dislocations glide with relative ease. This seems to be the case here: streaks with the same general direction are found throughout both grains. This localization in the GB region could be tied to a finite but low energy barrier that slows dislocation glide at the grain boundary, but does not arrest it completely. In Case 3 (Figure 4.4), there is also presumably the same CSL between grains that permits dislocation glide at the boundary, but with a greater differential in elastic strain, the dislocations are more generally distributed throughout the grains. Case 4 (Figure 4.5) is a very low angle boundary that is commonly treated as $\Sigma 1$ CSL GB and a high probability of dislocation glide. This appears to be the case since the streak patterns on both sides of the boundary seem identical. Dislocations further into the grain appear to be different, both to each other and to those observed near the boundary.

Comparisons were also made between strain measured from the PXM patterns from regions located near the free surface and regions located up to 60 μm below the free surface of the 1% strained sample. Figure 4.8 shows the orientation map obtained at depths from less than 10 μm to over 60 μm below the free surface. Diffraction spots from regions at several depths from the free surface are also shown in Figure 4.8. The degree of elongation of the diffraction spots is significantly greater (indicating higher dislocation density) in the regions near the free surface compared to the regions far below the free surface. This is attributed to the effect of mechanical polishing on increasing the amount of plastic strain in the region extending several micrometers beneath the sample surface.

The fact that PXM allows significant plastic strain differences to be detected between surface and bulk of the material is an important and useful observation. Strains produced by any form of surface preparation will have an important influence on the

propagation of cracks and it is important that these be able to be distinguished from bulk effects. This is a major advantage of PXM compared to neutron diffraction which is bulk sensitive and to EBSD which is so surface sensitive that exacting preparative protocols to remove damaged material from the outermost surface. PXM 2D maps are less affected by surface preparation than are these by EBSD, because the information depth is greater (see Table 1.4). PXM in-depth measurements are even more effective in removing surface effects.

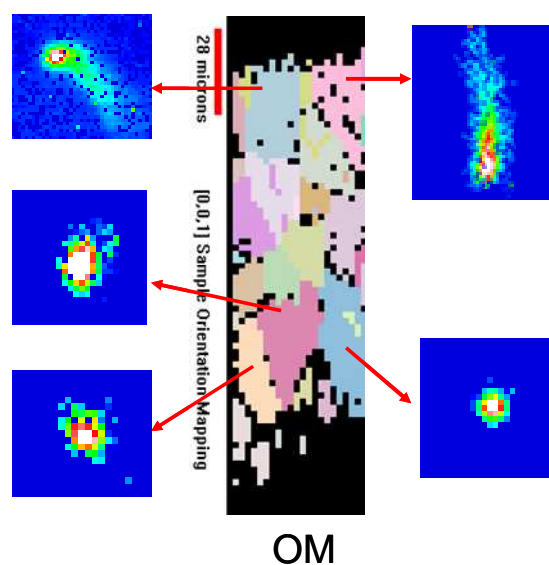


Figure 4.8 In-depth orientation map with diffraction patterns from different sample depths.

4.3 Summary

Polychromatic x-ray micro-diffraction (PXM) has shown its capability of detecting the strain distribution (elastic and plastic) introduced to Alloy 600 sample by a low uniaxial tensile stress (nominal 1% strain).

The elongation and splitting of PXM spots was compared for grains separated by grain boundaries of several angular mis-orientations. Similar dislocation densities, operating on the similar slip systems, were found on both sides of $\Sigma 3$ boundaries while considerable differences in the degree of elongation and splitting of diffraction spots occurred between grains that were separated by boundaries with other angles. This has important implications for predicting local regions in the microstructure that are susceptible to the initiation of intergranular stress corrosion cracking in the Alloy 600.

Elongation of the PXM diffraction spots from regions at several depths from the free surface of the end-bar sample indicates that the degree of plastic strain, and hence the local dislocation density, is significantly greater in the region extending less than 10 μm below the free surface compared to the regions far below the free surface. The elongation of the diffraction spots can be modeled by using simple simulation of two dislocation systems. This is attributed to the effect of mechanical polishing on increasing the amount of plastic strain in the region extending several micrometers beneath the sample surface. The fact that PXM can detect significant differences in the plastic strain between surface and bulk of the material is an important and useful observation for helping us understand the depth beneath a polished surface of a ductile metal that is affected by the metallographic preparation process. The plastic strain produced by any form of surface preparation will have an important influence on the propagation of cracks and it is important that these be able to be distinguished these affects from those of other metallurgical factors. This is a major advantage of PXM compared to the neutron diffraction technique.

The PXM technique appears to have the latitude and accuracy necessary to measure strain patterns caused before and during stress corrosion cracking (SCC): the ability to distinguish compressive and tensile strains is a particularly important advantage over EBSD which has no such capability.

Chapter 5

5. PXM Study of Unstressed and Stressed C-rings

C-rings are commonly-used specimens for determining the susceptibility to SCC of alloys in different product forms, such as tubing, rods and bars. In contrast to the relatively simple stress pattern in the uniaxial tensile samples, local mechanical stresses in SCC-cracked C-rings arise from many sources. Some of these are introduced by the action of the external force of the SCC on surface irregularities and the chemical energy released during reaction between solution and metal. Others come from rolling and swaging processes used in tube preparation. Before undertaking studies of strain distribution in samples cracked by SCC similar studies were carried out on an "as received" C-ring. Two such studies were done: one (unstressed C-ring) where the C-ring contained only those elements of strain that were caused during manufacture of the Alloy 600 tubing; a second one (stressed C-ring), immediately following the application of a torsional stress that was produced by the tightening of clamp surrounding the C-ring. This chapter presents the analysis of PXM results from these two samples: before and after stress application. This material has been previously published [88].

5.1 Brief Review of Experimental (Samples & Techniques)

C-ring samples were prepared from mill-annealed Alloy 600 tubing according to ASTM standard G-38, as described in section 2.2.2. The same area (refer to Figure 2.3) from the cross-section of the C-ring before and after applying strain was studied using PXM at ALS.

5.2 Results and Discussions

The beam spot size was approximately one micron, and a step size of one micron was used to take PXM measurements over a sample area of 40×70 points (microns) for the analyses, before and after stress. Care was taken to analyze the same area on the sample before and after stress, although the correspondence is likely not accurate to a micron. The resulting orientation maps (OM) and von Mises equivalent strain maps

(VM) for the C-ring sample before and after stress are presented in Figures 5.1 (b) and (c) respectively. In Figure 5.1(a), the sample positioning in the beamline and its coordinate system are also presented. The tensile stress direction is along the y direction as labeled, which should theoretically yield a tensile deviatoric strain in y direction (that is, $\epsilon_{yy} > 0$). The sample outer edge of the apex is located to the right hand side of the OM and VM maps. The black areas within the maps are a result of failure to index the Laue images either due to the existence of extreme plastic deformation or lack of Laue spots if the analyzed area is beyond the sample edge.

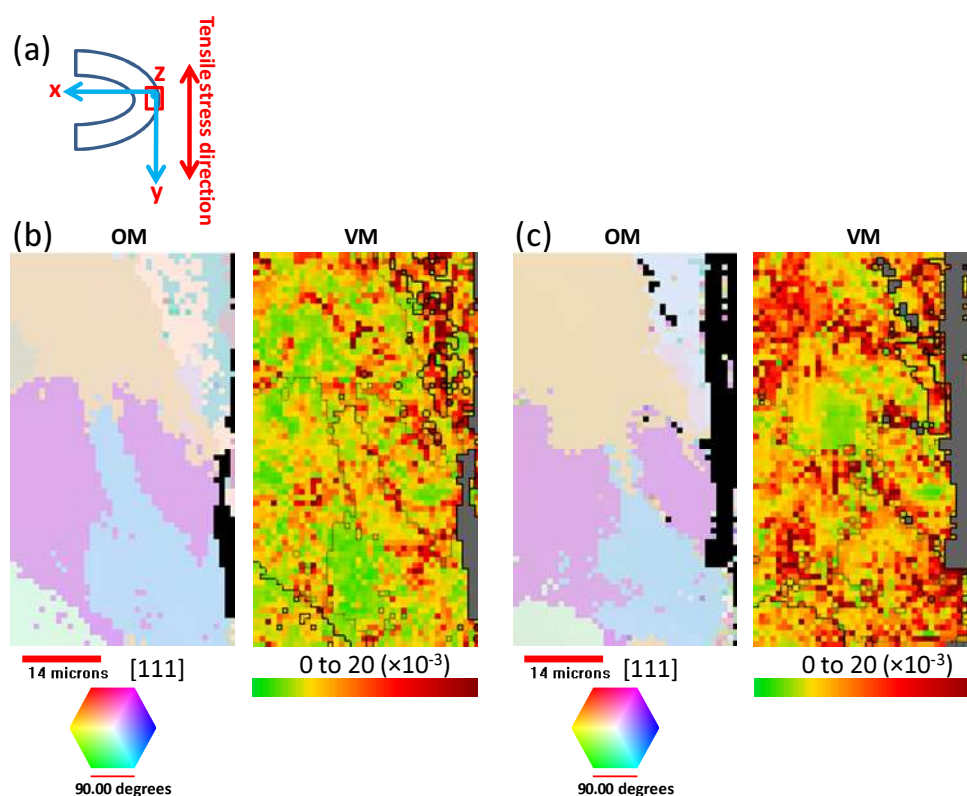


Figure 5.1 (a) Schematic of the analysis area, tensile stress direction, sample positioning in the beamline and the sample coordinate system; Laue XRD orientation maps (OM) and von Mises equivalent strain maps (VM) for the C-ring sample: (b) before and (c) after stress.

5.2.1 Elastic Strain Study

In Figure 5.1, the OM maps before and after stress showing the crystallographic direction of each grain with respect to the [111] pole, indicate similar grain structure,

however changes are apparent after the application of the stress. These changes were studied in detail and will be described in the next section.

According to the scale used in the VM maps (Figures 5.1 (b) and (c)), regions of low VM strain are characterized by green while the highest strain regions for the applied scale are indicated by red. Comparison of the VM maps before and after the application of stress, indicates an increase in VM strain after stressing as more red areas were obviously observed in VM map of the stressed C-ring.

The deviatoric strain component maps were also obtained for the C-ring sample before and after stress, these are presented in Figure 5.2 (a) and (b), respectively. The C-ring stress loading direction and the sample coordinate system (see Figure 5.1(a)) predict that the principal deviatoric strain component, ϵ_{yy} , should show tensile strain. Indeed the principal deviatoric strain component, ϵ_{yy} , does show high tensile strain throughout much of the analysis area. The ϵ_{xx} and ϵ_{zz} both show mainly compressive strain with a few regions of tensile strain, so to balance the ϵ_{yy} tensile strain. All principal deviatoric strain component maps show higher magnitude of strain after the application of the stress.

The deviatoric shear strain component map, ϵ_{xz} , exhibits highly strained areas before strain application, and somewhat elevated strain after the applied stress. The other two deviatoric shear strain component maps of ϵ_{xy} and ϵ_{yz} are more difficult to interpret in terms of strain levels, however, it appears that the highly strained areas in the maps before stress application have shifted to other areas after the stress application.

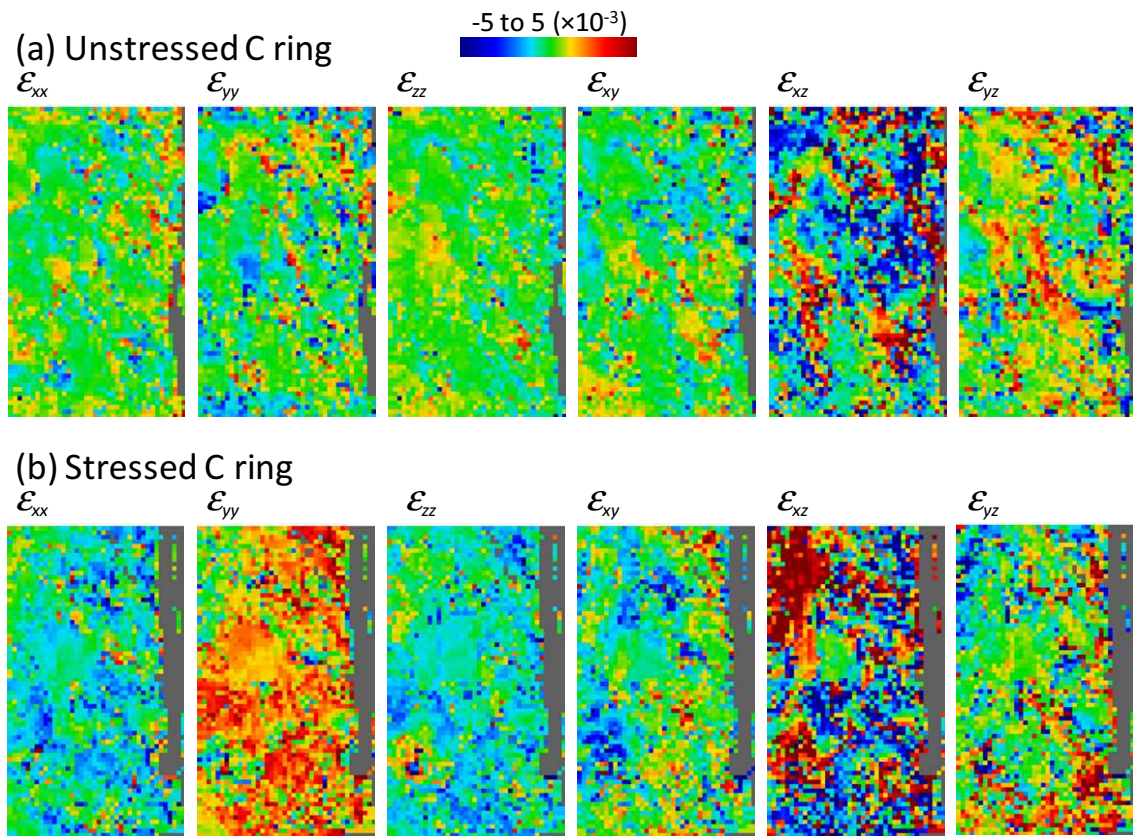


Figure 5.2 The deviatoric strain component maps for the C-ring samples: (a) before and (b) after stress. The same color scale was used for both samples, as shown at the top of the figure.

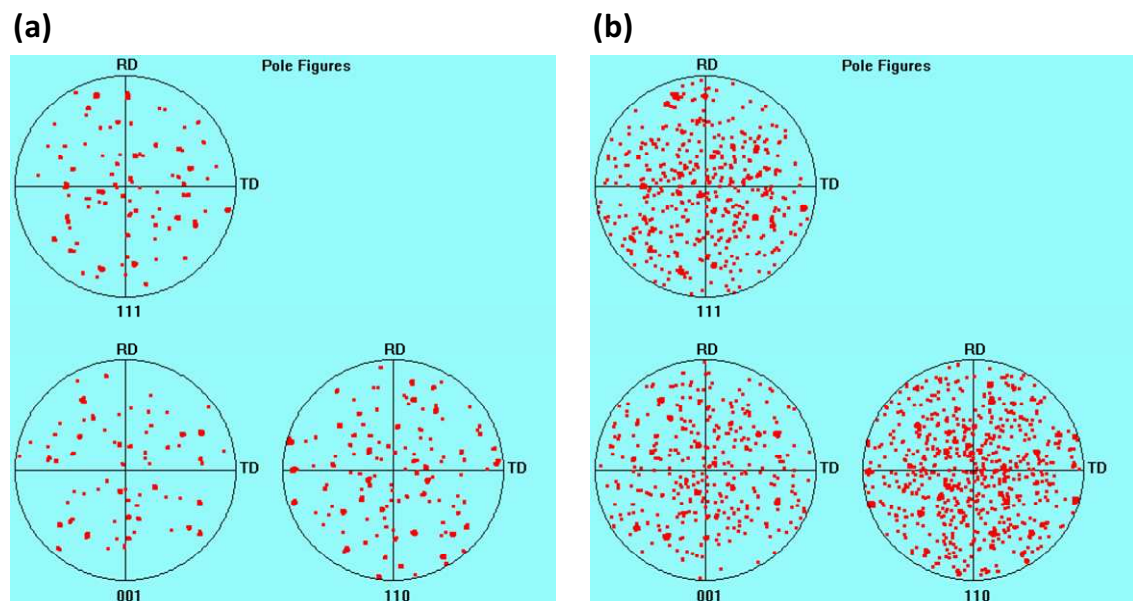


Figure 5.3 The pole figures for the C-ring samples: (a) before and (b) after stress.

5.2.2 Study of Pole Figures

The pole figures for the C-ring sample, before and after stress application, are presented in Figures 5.3 (a) and (b), respectively. Comparison of the pole figures reveals an apparent higher density of spots in the pole figures after the application of stress. A more correct interpretation is that the spots are more widely distributed in the pole figures after stress application. The same general sample area (similar grain structure) and the same map size (40×70 data points) was collected in both cases, therefore the same number of spots would be arranged in the respective pole figures. Thus, comparison of the pole figures indicates that the sample has plastically deformed or undergone significant lattice rotation due to the stress application.

To investigate this further, ThreeDimX-RayMicroscopy was used to zoom in on the [111] pole figure in order to investigate the extent of lattice rotation through one of the grains. The results from this exercise for the C-ring sample, before and after stress application, are presented in Figures 5.4 (a) and (b), respectively, showing the (i) OMs for the grain, and the accompanying (ii) zoomed-in pole figures and (iii) color scales.

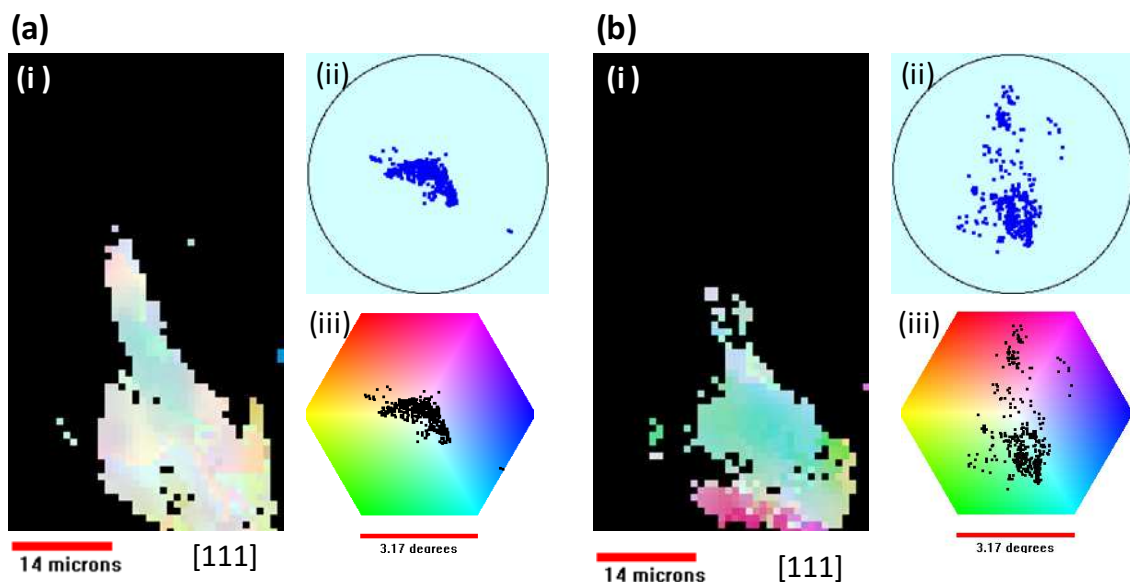


Figure 5.4 The zoomed-in pole figures for the C-ring sample: (a) before and (b) after stress.

The same zoomed scale was applied to both pole figures. It is clear that the spots in the pole figure for the grain shown after the stress application (Figure 5.4(b), i and ii) are more widely dispersed than in that before stress application (Figure 5.4(a), i and ii). The grain has undergone significant lattice rotation due to the stress application and this is further highlighted in the respective OMs for the grain before and after stress. There is a larger color gradient exhibited in the grain after stress application. Grain rotation increases from approximately 2° to 5° after stress application, according to interpretation using the color scale.

5.2.3 Peak Study

Comparison of the OMs before and after stress application revealed differences (Figure 5.1). It appears that some of the grain structure has been disrupted due to the applied stress. The grains which will be discussed are labeled in letters (see OMs represented in Figures 5.5 (a) and (b)). The grain labeled as P appears to have been disrupted in some regions and replaced with grain structure belonging to grains T or S depending on the region. It is important to note that these Laue measurements are not depth resolved and that we are getting information from depths up to $60\ \mu\text{m}$. Keeping in mind that the analysis depth is approximately $60\ \mu\text{m}$ for this Ni alloy and that the average grain size is approximately $20\ \mu\text{m}$, we are likely sampling more than one grain for each measurement or data point.

Laue patterns are very sensitive to the presence of dislocations. The density of dislocations and the way in which they are organized can be determined from the Laue patterns [57, 68, 86, 89]. GNDs can cause lattice rotation which gives rise to streaking of the Laue patterns. In later stages of plastic deformation, the dislocations will organize themselves into walls in order to lower the stored energy. As discussed in section 1.1.1, the regions between dislocation walls are referred to as cells and they are relatively dislocation free. The formation of dislocation walls and cells will cause the streaks to appear discontinuous or split.

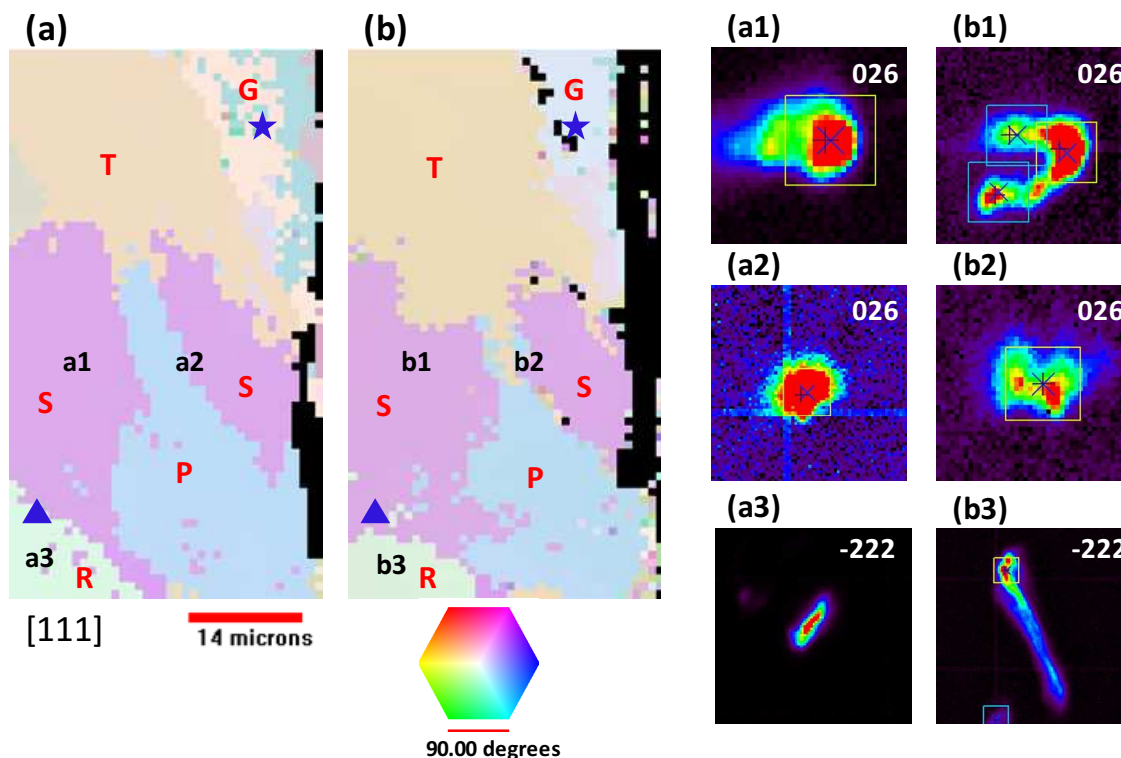


Figure 5.5 Comparison of the peak shape from the same locations of the (a) unstressed C-ring and (b) stressed C-ring samples. Panels a1, a2, a3 show selected peaks from each of these locations in the unstressed C-ring, while panels b1, b2, b3 represent peak patterns from the corresponding locations in the stressed C-ring. The numbers on the peak images are the Miller indices of the chosen peak.

The Laue images in selected sample analysis areas were examined for evidence of plastic deformation after the application of the stress. The (026) reflections from indexed Grain S are enlarged in Figures 5.5 (a1), (a2), and (b1), (b2), and the approximate origins in the analysis areas are indicated by a1, a2, and b1, b2, in the OMs in Figures 5.5 (a) and (b). Although some plastic deformation is evident in the (026) reflection before stress, the reflections are markedly deformed after the applied stress, displaying streaking and splitting. The (026) reflection shown in (b1) exhibits very complex streaking and splitting, with at least 3 changes in the streaking direction, implying at least 3 activated slip systems. Laue measurements are not depth resolved; therefore these slip systems are likely active at different depths within the grain at this location. The splitting of the streaks indicates the formation of dislocation cells and walls [57].

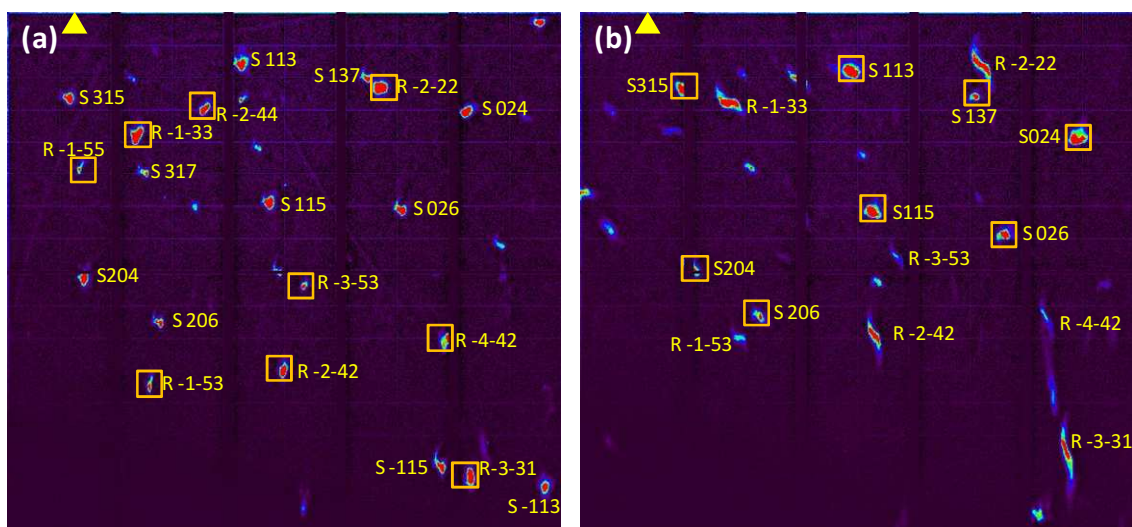


Figure 5.6 Laue XRD images for the C-ring sample from a location denoted by the blue triangle in the OMs shown in Figure 5.5: (a) before and (b) after stress.

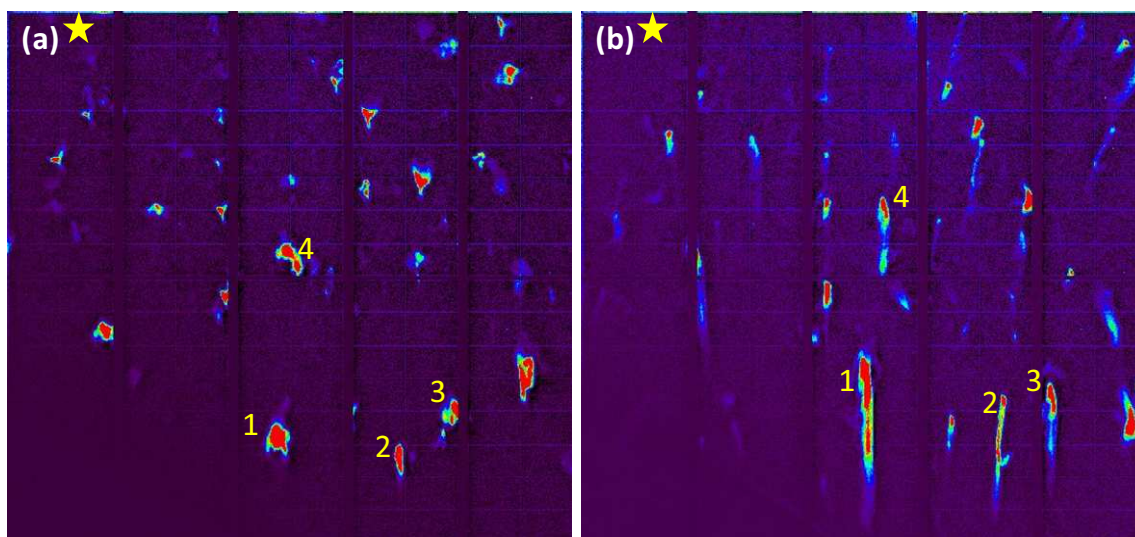


Figure 5.7 Laue XRD images for the C-ring sample near the sample outer surface, denoted by the blue star in the OMs shown in Figure 5.5: (a) before and (b) after stress.

Laue images in Grain R were also examined for evidence of plastic deformation. The (-222) reflections from indexed Grain R are enlarged in Figures 5.5 (a3) and (b3), and the approximate origins in the analysis areas are indicated by a3 and b3 in the OMs in Figures 5.5 (a) and (b), respectively. Although the (-222) reflection shows moderate streaking (Figure 5.5 (a3)), this reflection is markedly streaked and also exhibits splitting (Figure 5.5 (b3)) after the applied stress.

Laue images from an area in which the grain structure of Grain R appears to have been disrupted after stress application, are presented in Figure 5.6. The approximate sample analysis area from which these Laue images originate, is represented by a blue triangle in the OMs in Figure 5.5. The Laue image shown in Figure 5.6 (a), before stress application, is indexed as grain R. The indexed reflections for grain R are encased by yellow boxes in the image, and the reflection hkls are specified after the letter R. The remaining reflections in the image are consistent with reflections from Grain S (comparison with an indexed image from Grain S) and the reflection hkls are also specified in the image.

The Laue image shown in Figure 5.6 (b) (from approximately the same sample area as the image shown in Figure 5.6 (a)), after stress application, is indexed as grain S rather than grain R. The indexed reflections for grain S are encased by yellow boxes in the image, and the reflection hkls are specified after the letter S. The reflections consistent with grain R are very streaked and have moved vertically upwards in the Laue image from their original position before stress application, indicating marked lattice rotation or plastic deformation due to the applied stress. The reflection contributions from Grain R are too deformed for the software to index, and because there is contribution from Grain S, this Laue image gets indexed as belonging to Grain S rather than R.

Laue images from the near surface of the sample were also examined and are presented in Figure 5.7. The approximate sample analysis area (Grain G), from which these Laue images originate, is represented by a blue star in the OMs in Figure 5.5. Four of the Laue spots indexed for grain G are labeled 1-4 for demonstration in Figure 5.7. These Laue spots are severely streaked after the stress application indicating marked plastic deformation.

5.3 Summary

PXM measurements were performed on the same cross sectional area of a C-ring specimen before and after applying stress. Compared to the unstressed C-ring, a significant tensile strain was observed in the y direction - the main stress axis direction

from the stressed C-ring as expected, as was a higher composite (von Mises) strain. This is very important information as a tensile stress/strain is usually an essential element for SCC to occur. In another words, one can predict that a crack would preferentially propagate along a direction within the xz plane, a direction perpendicular to the stress axis for this C-ring specimen when in a susceptible environment.

Significant grain lattice rotation and pronounced plastic strain was noted. Similar grain structures were observed in OMs before and after stress, however, changes are noticeable, indicating lattice rotation. The application of pole figures were found very useful in this case where the same sized area was studied. The higher density of spots in the stressed C-ring sample indicates the sample has undergone high plastic deformation or significant lattice rotation due to the stress application. The zoomed-in pole figure study of a single grain also confirmed this. Shape changes of the Laue peaks from the same locations before and after stress were also investigated. Lattice rotation or high plastic deformation was demonstrated again as pronounced streaking and/or split Laue spots from the stressed C-ring.

Chapter 6

6. PXM Study of 6h and 18h SCC-cracked C-rings

A major objective of our work with PXM has been the study of strain distributions near cracks in Alloy 600 C-rings that were instigated by stress corrosion cracking (SCC). This chapter presents an assessment of the strain tensors and dislocation distributions around small cracks in Alloy 600 tubing that had been induced during electrochemically accelerated caustic corrosion in a high temperature autoclave. The content present is mainly extracted from previous published paper [88].

6.1 Brief Review of Experimental (Samples & Techniques)

The C-rings used for the investigation in this chapter were prepared by the same protocols as that used for the C-rings in Chapter 5. The methods used to cause SCC were described in section 2.2.3. Two examples of SCC-initiated cracks are discussed: one, a sample corroded for 6h (6h SCC-cracked C-ring) and a second corroded for 18h (18h SCC-cracked C-ring). After exposure cracks were identified in both 6h and 18h C-rings. The samples after exposure were embedded in Bakelite for mechanical polishing followed by electropolishing until a crack was observed on the cross section. Then the cross sectional area covering the cracks were FIB polished and cuts with Pt lines were made on both sides of the FIB polished area as marking. All studies were performed on these cross sectional cracks. It was observed that SCC was mainly happening within a narrow band around the apex of the C-ring samples, in which multiple crack initiation sites were observed. A typical crack from the 6h sample is about 15 μ m in length, while the crack for 18h sample is about 30 μ m. SEM images of these are shown in Figure 6.1. Both cracks are seen to propagate along grain boundaries, (intergranular SCC (IGSCC)), and mainly propagate along the C-ring thickness, a direction perpendicular to the main stress axis as predicted in the last chapter. Areas covering these cracks were selected to perform the PXM studies.

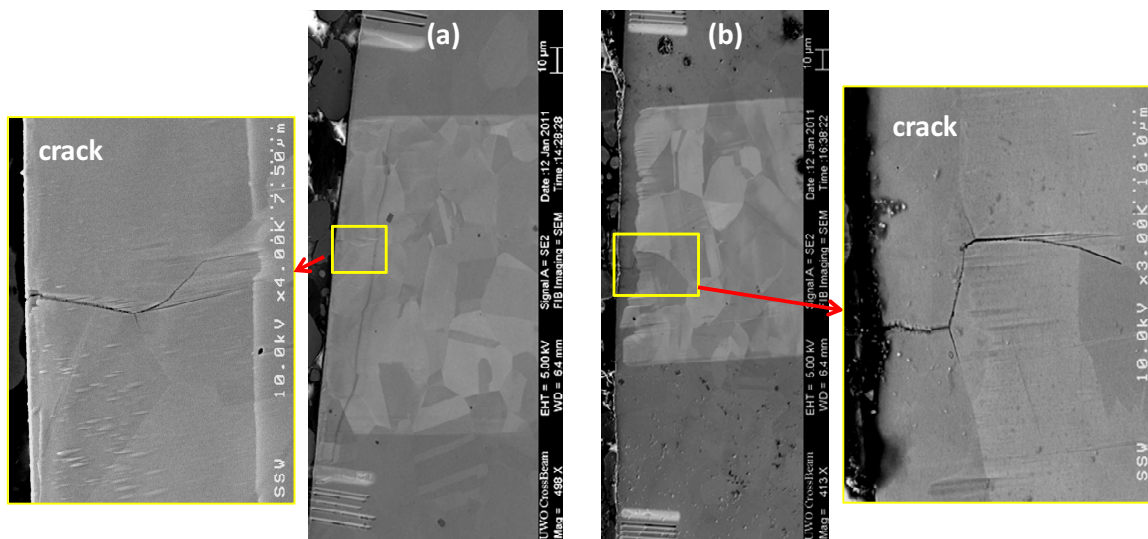


Figure 6.1 SEM images from the cross sectional surface of: (a) the 6h cracked C ring and (b) 18h cracked C ring samples showing the area covering cracks after FIB polishing. SEM images with higher magnification of the cracks are also shown here. Note the line within the FIB polished area and tiny scratches around both crack tips; these are defects from FIB polishing.

6.2 Results and Discussions

6.2.1 Elastic Strain

Total areas of $70 \times 162 \mu\text{m}^2$ for the 6h sample and $76 \times 232 \mu\text{m}^2$ for the 18h sample covering the cracks shown in Figure 6.1 were scanned by PXM. The orientation maps and strain maps, along with their positioning in the beamline and their coordinate systems for both samples are presented in Figures 6.2 and 6.3, respectively. The crack path in the PXM orientation map (OM) was located by inspecting the SEM images of the crack area. The crack path was determined to be intergranular. The PXM OM was compared to the SEM image, and the grains along the crack path in the PXM OM map were identified. The grain dimensions in the two maps do not match exactly. This is likely due to the differences in analysis depths between the two techniques. The analysis depth of PXM for the Ni alloy is greater ($\sim 60 \mu\text{m}$) than that of SEM (1-2 μm). As well, the sample is at a 45° tilt to the incoming x-ray beam during the PXM analysis. As a result, subsequent indexing of the Laue images may give slight differences in the grain boundary locations, as compared to those in the SEM images.

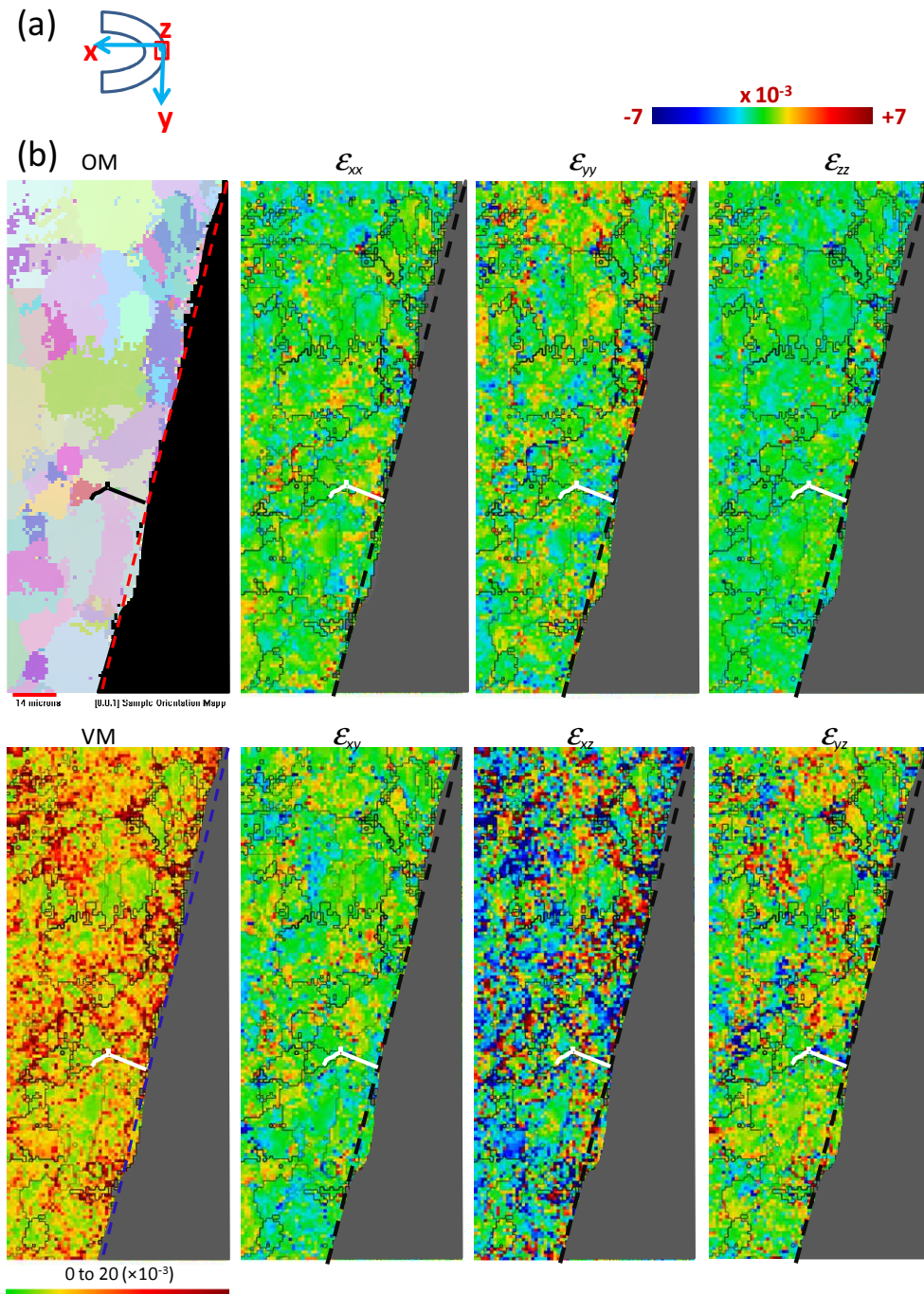


Figure 6.2 (a) Schematic of the analysis area, sample positioning in the beamline and the sample coordinate system; (b) Orientation and strain maps for the scanned area from the 6h SCC-cracked C-ring sample. The color legend for the deviatoric strain maps is shown above the maps, with a scale of -7 to $+7$ ($\times 10^{-3}$). A unique color legend was used for the VM strain map, shown below the VM map. The dashed lines in the maps indicate the sample edges, while the black/white filled lines show the locus of the crack by overlaying the SEM images.

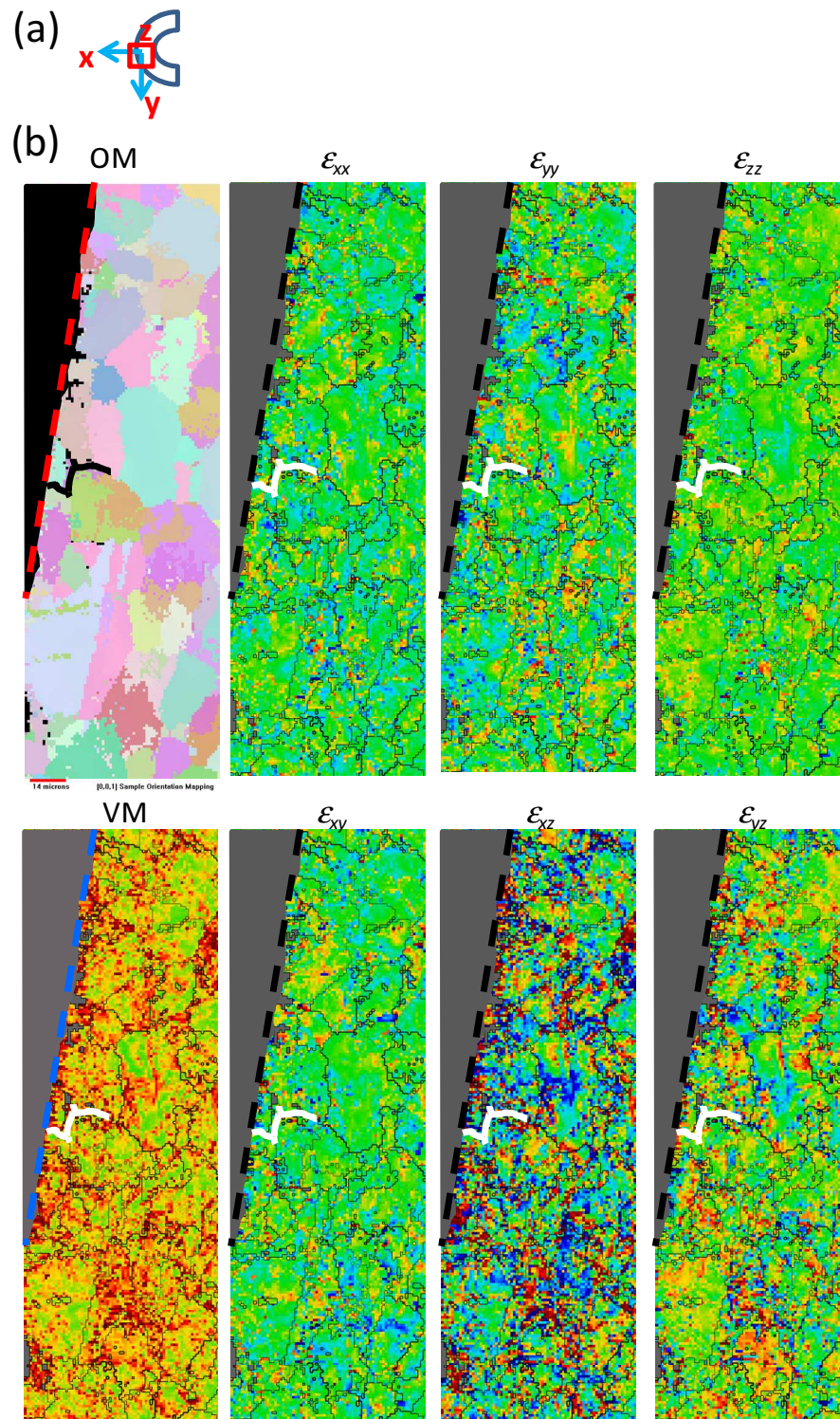


Figure 6.3 (a) Schematic of the analysis area, sample positioning in the beamline and the sample coordinate system; (b) Orientation and strain maps for the scanned area from the 18h SCC-cracked C-ring sample. Refer to Figure 6.2 for the color legend for strain maps. The dashed lines in the maps indicate the sample edges, while the black/white filled lines show the locus of the crack by overlaying the SEM images.

In Table 6.1, average strains are compiled for the entire areas measured by PXM. Average ϵ_{yy} and VM strain are seen to have increased significantly from the unstressed to the stressed C-ring. After crack initiation, the average strain, particularly the ϵ_{yy} , decreases with the energy released as the crack opens and more branching occurs, and with the strain relaxation due to the heat in autoclave. ϵ_{xx} and ϵ_{zz} from 6h and 18h samples are both lower than those from the stressed C-ring sample as well.

Table 6.1 Average strain values calculated over the detected areas for all four C-ring samples*.

$\times 10^{-3}$	Unstressed	Stressed	6h-Crack	18h-Crack
ϵ_{xx}	0.1	-0.7	0.1	-0.1
ϵ_{yy}	-0.1	1.5	0.1	-0.05
ϵ_{zz}	0.03	-0.7	-0.2	0.2
VM	5.8	7.9	6.5	7.1

*The values for the unstressed and stressed C-rings were obtained from the PXM results presented in Chapter 5. Unstressed and stressed values are for the same original sample while 6h and 18h values are for different original sample.

Of particular interest in the analysis below are the common patterns of strain found in both these examples in regions within and near the cracks. Figures 6.4 (a) and (b) show strain and orientation maps for the crack region (part of the surveyed area) for the 6h and 18h samples, respectively. The measurement of strain in the y direction (tensile stress axis direction) is particularly important, because it provides the best possible measure of strain direction as a result of crack opening and propagation. Tensile strains (shown as shades of red in the ϵ_{yy} map in Figure 6.4) would be expected for those regions that precede the crack, while strain direction(s) in the opened crack could be susceptible to several factors and thus less predictable. In fact, in Figure 6.4(a) (see inset above the ϵ_{yy} map) the deviatoric strain component ϵ_{yy} at the crack tip for the 6h specimen (arrow 'a') is somewhat tensile. Ahead of the crack tip, at the triple point (arrow 'b'), the (tensile) strain is higher, reaching a maximum of about 2×10^{-3} . Such measurements are rendered approximate by the depth of the crack and the uncertainty of the position of the actual tip. The area near the tip of the branch crack is also tensile. Within the crack itself, and particularly at the crack mouth, the strains are found to be compressive (blue). In the case of the 18h specimen, Figure 6.4(b), a tensile strain is also seen at the crack tip with a magnitude near 5×10^{-3} . This strain value is averaged over a

volume of several cubic microns; localized strain near the actual tip could be orders of magnitude higher.

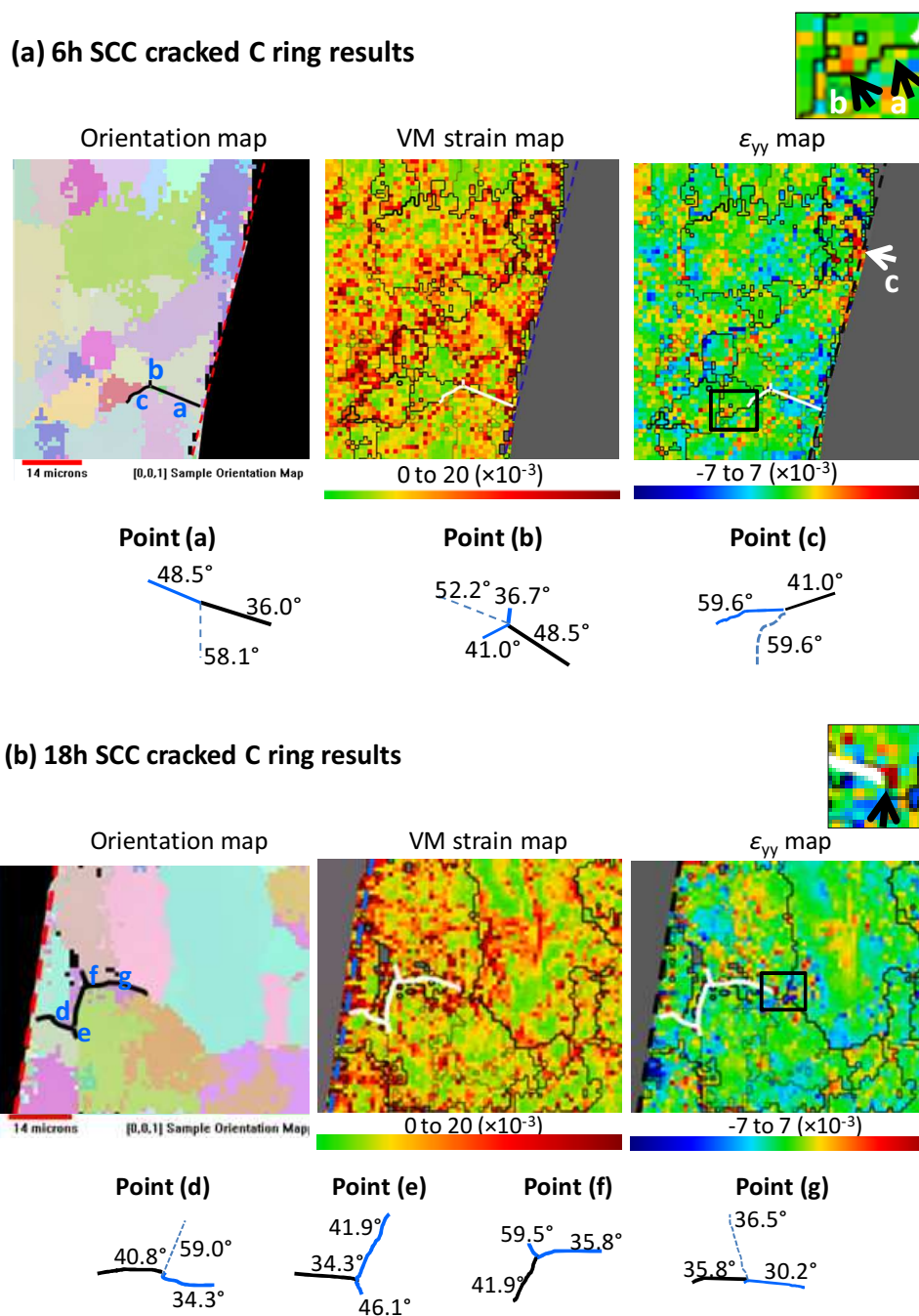


Figure 6.4 OMs, VM map and the y principal deviatoric strain ϵ_{yy} map with the mis-orientation angles shown between grains around cracks for the (a) 6h and (b) 18h SCC cracked C-ring samples. Enlarged maps from the square in the ϵ_{yy} map are shown at the top right corner of 6h and 18h results. The white arrow 'c' in 6h shows a tensile area which indicates a potential crack initiation site.

Statistically, the occurrence of tensile elastic strain in the grain boundary region is considered to be significant but not necessarily absolute. There are some other regions within Figure 6.4 (a) and (b) where high tensile strain is evident; however, most of these do not occur along grain boundaries. One exception to this is seen at point 'c' in the 6h sample: a region of high tensile strain extends along a grain boundary, beginning at the outer surface. Such a strain condition could have resulted from localized corrosion attack at the boundary followed by an accumulation of corrosion product oxides within the reacted boundary [90]. This will be discussed further below. Maps of composite (von Mises) strain are also shown in Figures 6.4 (a) and (b). While regions of high composite strain do occur along several of the boundaries, few of these exhibit a high ϵ_{yy} and are therefore not considered to have a significant bearing on the cracking process.

6.2.2 Grain Boundary Study

For both 6h and 18h cracks, the grain boundary mis-orientation angles along the crack paths were determined, along with the mis-orientation of grain boundaries that intersect the crack at triple points. It should be noted that the mis-orientation between the grains which had been adjoining along the crack boundary is slightly changed after the crack opened. The results are shown in Figures 6.4(a) and (b) for three triple points along each crack. The grain boundary angles fall between 34° and 60° . In every case, the main path of the crack is seen to follow the boundary with the lowest mis-orientation, although at some triple points, a short branch crack did follow a grain boundary with a higher mis-orientation. This is an observation never reported before, however, it doesn't conflict with the previous findings. Commonly, the low Σ grain boundaries are believed to be more resistant to SCC, which have relatively low energy. The energy of the random high angle grain boundaries ($>15^\circ$) doesn't show much differences, as seen in Figure 9 from [29]. Lin et al. [31] found that an increase in the special grain boundary ($\Sigma \leq 29$) frequency in Alloy 600, resulted in decreased susceptibility to intergranular corrosion. Gertsman and Bruemmer [29] studied the grain boundary character along IGSCC and at crack arrest points. While low angle boundaries (LABs $< 15^\circ$) and coincident site lattice (CSL)-related boundaries are generally considered to be crack-resistant, they found that

LABs may be susceptible to cracking. Only $\Sigma 3$ boundaries were found to be crack resistant and they were not completely immune to intergranular SCC [29].

One $\Sigma 3$ boundary was identified along the crack paths of the 18h sample. This $\Sigma 3$ boundary is located at ‘triple point f’ along the 18h crack in Figure 6.4(b), and the crack only follows this boundary at the triple point for a short distance, preferring instead to follow the 35.8° grain boundary. The $\Sigma 3$ grain boundary angle of 59.5° falls within Brandon’s criterion ($\Delta\theta \cong \theta_0 \Sigma^{-1/2}$, where $\theta_0 \cong 15^\circ$) [19].

The distribution of dislocations within each grain adjacent to each crack locus was studied. Of particular interest was the “hard” and “soft” natures of each adjacent grain with the likelihood that dislocations present in one grain would migrate across a grain boundary to the adjacent grain as discussed in Chapter 4. In the case that migration does not occur, dislocations could pile up at the boundary and could potentially contribute to brittle fracture [91]. In the case of the 6h crack, the shapes of the indexed diffraction spots for a number of grains were followed from grain centre to edge and into an adjacent grain. In Figure 6.5(a2) the relationships of dislocations in Grains 4 and 5 are followed along a transgranular path just ahead of the crack tip. Within Grain 4, the indexed spots are consistently small and round, while in Grain 5 spots are streaked with the extent of streaking increasing as the grain boundary is approached. Grain 4 is thus regarded as “hard” and dislocations from “soft” Grain 5 would be likely to pile up at the boundary. This could be viewed as another factor contributing to the path taken by the main crack. Grains 1 and 2 are both considered “soft” (see page 56 in Chapter 4 for the detailed discussion about soft-hard nature of grains). Relatively similar streaked indexed spots are found on both sides of the boundary: this suggests that dislocations are able to be transmitted through the boundary and the possibility of pile up at the boundary is relatively less than for that between Grains 4 and 5. In fact, although some cracking along this boundary did occur, the process was truncated in favor of crack propagation along an adjacent hard-soft boundary. Another reason that the crack did not continue to follow the grain boundary between G1 and G2 is that this path is parallel to the stress axis and thus, follows an unfavorable direction with respect to crack propagation. Lehockey *et al.* [87] used Orientation Imaging Microscopy (OIM) to study the plastic

zones along an inner diameter (ID) crack in Alloy 600 steam generator tubing. They found that large stresses and therefore plastic zones must develop before the crack can propagate in directions towards the stress axis. Gertsman and Bruemmer [29] found that in some instances, a crack did not propagate even when it was favorably oriented with the stress axis.

The dislocation distribution in the strained grain boundary c (in Figure 6.4(a)) was also examined. Along a line across the grain boundary the shapes of diffraction spots were examined for grains on each side of the grain boundary (not shown). These were found to be uniformly unstreaked and therefore provide evidence that dislocation pileup is low in the vicinity of the strained boundary. Thus, although the boundary is locally strained in an appropriate direction for cracking, the lack of dislocation pile up may have delayed or prevented crack initiation.

In the vicinity of the 18h crack, similar studies of dislocation distributions between adjacent grains were also conducted. The crack initiated on the sample surface between G1 and G7, and then encountered a triple point after propagating between G1 and G3. At this triple point between G1/G3/G2, the crack had two directional choices, both along unfavorable paths, parallel to the stress axis. In Figure 6.5(b), the hard-soft nature of a number of grains along the crack locus was determined. The shapes of diffraction spots across two important boundaries near the crack are shown. In Grain 3, long curved streaks are characteristic, with the streak length increasing near the boundary. In Grain 2, the spot shape is more rounded. Thus, along this line, it appears that dislocations are quite different on each side of the boundary, and this would suggest a boundary where dislocation pileup could occur. For the line that crosses the boundary just ahead of the branch crack (G1-G2), streaks of similar shape and direction are found: This suggests that there should be fewer dislocations to pileup at the grain boundary. Thus, on this basis, one would predict that cracking would be more favorable along the GG2-G3 boundary, while it goes a short distance along G1-G2 boundary. So, the presence of hard-soft boundaries may be one factor in determining the direction of the cracking.

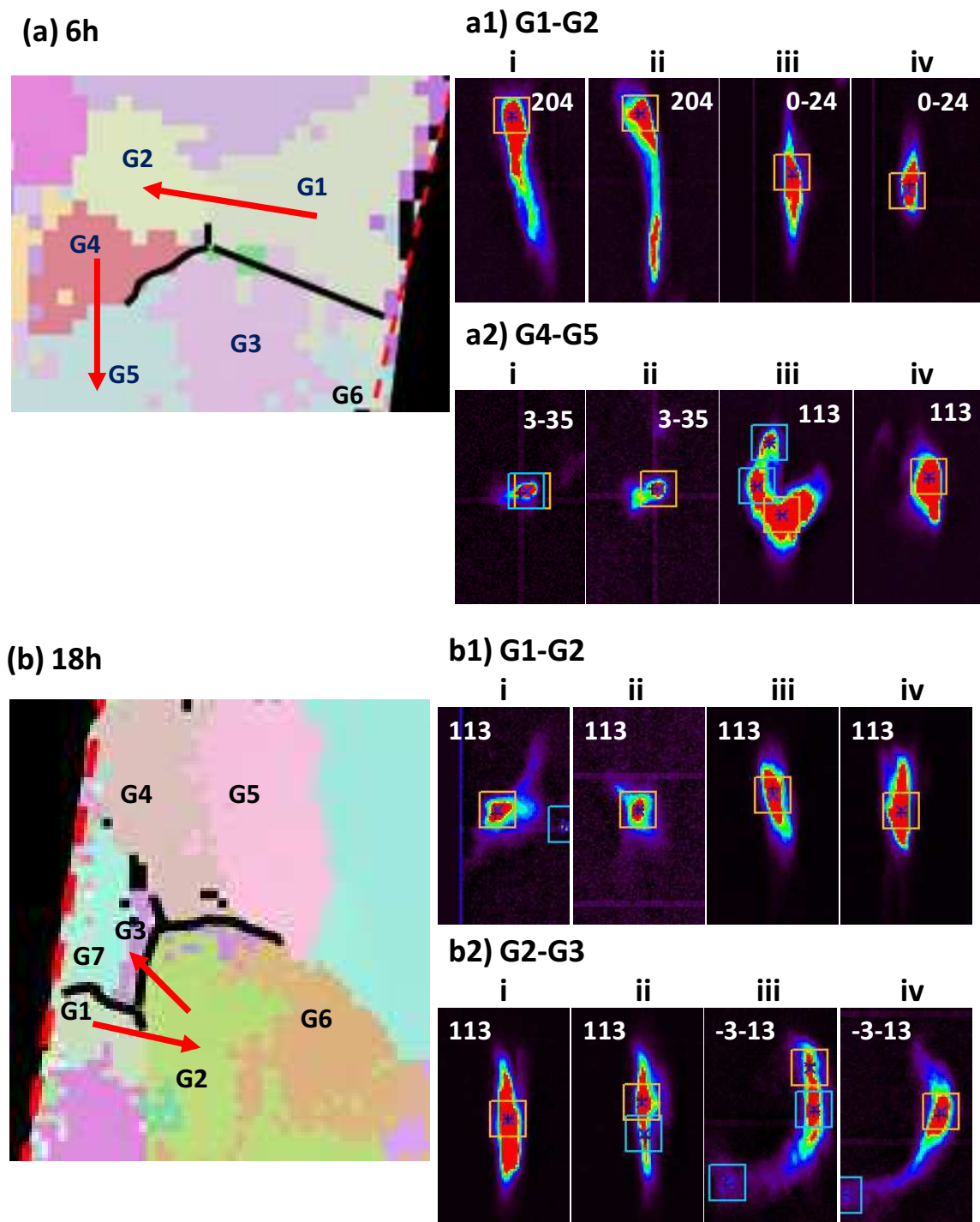


Figure 6.5 Peak patterns collected from adjacent grains around the cracks formed on the (a) 6h and (b) 18h SCC cracked C-ring samples. For each sample, peaks are shown from four locations along the colored arrows crossing two adjacent grains. For (a1) G1-G2, peaks from mid-grain G1 to mid-grain G2 following the arrow are displayed. Peak (i) is from the mid-grain G1 and peak (ii) is from the G1 side of the grain boundary, while peak (iii) is from the G2 side of the grain boundary and peak (iv) is from the mid-grain G2. The peaks in all the following examples are arranged similarly to that in (a1) G1-G2. The numbers on images of the peaks are the Miller indices of the chosen reflection.

The mis-orientation angles between grains is another factor to consider. It was observed (Figure 6.4) that the cracks tended to propagate along grain boundaries with the lower mis-orientation angle. Figure 6.4 (b, Point (e)), indicates that the grain boundary mis-orientation angle between G2-G3 is less than that between G1-G2. Thus, several factors need to be considered in determining the path of crack propagation, including the mis-orientation angle at the grain boundary, the direction of the stress axis and the hard-soft nature of the adjacent grains. Guertsman and Bruemmer [29] also came to the conclusion that factors other than grain boundary crystallography must be considered in determining IGSCC susceptibility. They felt that chemical parameters must also be considered, along with the geometrical parameters.

6.2.3 Schmid Factor

The Schmid factors of grains on either side of the cracks were also calculated for the 6h and 18h SCC-cracked samples, and these are presented in Table 2. Schmid factor is a measure of the ease with which could become a slip system activated in a grain under a stress from a given direction. Generally, the slip system with the highest Schmid factor would be more likely to be the operating slip system in the material. West et al. [32] found that cracks occurred preferentially along grain boundaries with trace inclinations perpendicular to the stress axis and adjacent to grains with a low Schmid Factor. They stated that their model is more applicable to the study of crack initiation than propagation. The orientation maps of the 6h and 18h corroded and cracked samples in Figures 6.5 (a, b) do indicate that the crack is initiated at grain boundaries which are oriented more perpendicularly towards the stress axis. Table 2 presents Schmid factors for only those grains along the crack pathway. Schmid factors were also calculated for a number of surface grains within the sample analysis areas, away from crack initiation sites, in the 6h and 18h samples. The Schmid factors for 6 surface grains in the 6h sample ranged from 0.41972 to a high of 0.4860, with the lowest being that for the Grain 6 (see Table 2) adjacent to the crack initiation site. The Schmid factors for 9 surface grains in the 18h sample ranged from 0.37817 to a high of 0.45796, with the lowest being that for Grain 7 adjacent to the crack initiation site. Thus, the Schmid factor of one of the grains adjacent to the crack at the 6h and 18h initiation sites was found to be the

lowest, compared to Schmid factors calculated for surface grains away from the initiation site, and also along the crack path into the bulk. While the results are barely statistically relevant, they are consistent with the model put forth by West *et al.* [32].

Table 6.2 Schmid factors calculated for the grains around cracks of both 6h and 18h SCC cracked C-ring samples. Refer to Figure 6.5 for the grain number locations. Note that only the maximum value of Schmid factors calculated from the 12 slip systems was reported for the grain.

Schmid Factor	G1	G2	G3	G4	G5	G6	G7
6h crack	0.48605	0.49514	0.43546	0.42785	0.42204	0.41972	
18h crack	0.44746	0.42138	0.49295	0.45542	0.42339	0.43725	0.37817

6.2.4 Local Mis-orientation (Plastic Strain) Study

Measurements of plastic strain present in the microstructure were also conducted near the crack tip. In Figures 6.6 and 6.7, the magnitude of pixel-to-pixel crystallographic mis-orientation (local mis-orientation) is mapped with respect to the locus of the crack for both 6h and 18h C-rings, noting that only the area around the crack is enlarged and shown here. In Figure 6.6, the highest magnitude in local pixel-to-pixel angular mis-orientation (1.0-1.5 degrees) occurs along the crack path between G5 and G6, as well as ahead of the crack at the triple point G5/G6/G8. In Figure 6.7, the same phenomenon has been observed for the 6h sample. That is, the highest local mis-orientation is found around the crack path and ahead of the crack tip, however, with a lower magnitude (0.5-1.0 degrees). The γ tensors of the elastic strain reported in section 6.2.1 (Figure 6.4) were also found to be elevated in the region ahead of the crack tip; however, the information provided by the local pixel-to-pixel mis-orientation seems to be more detailed and well-defined.

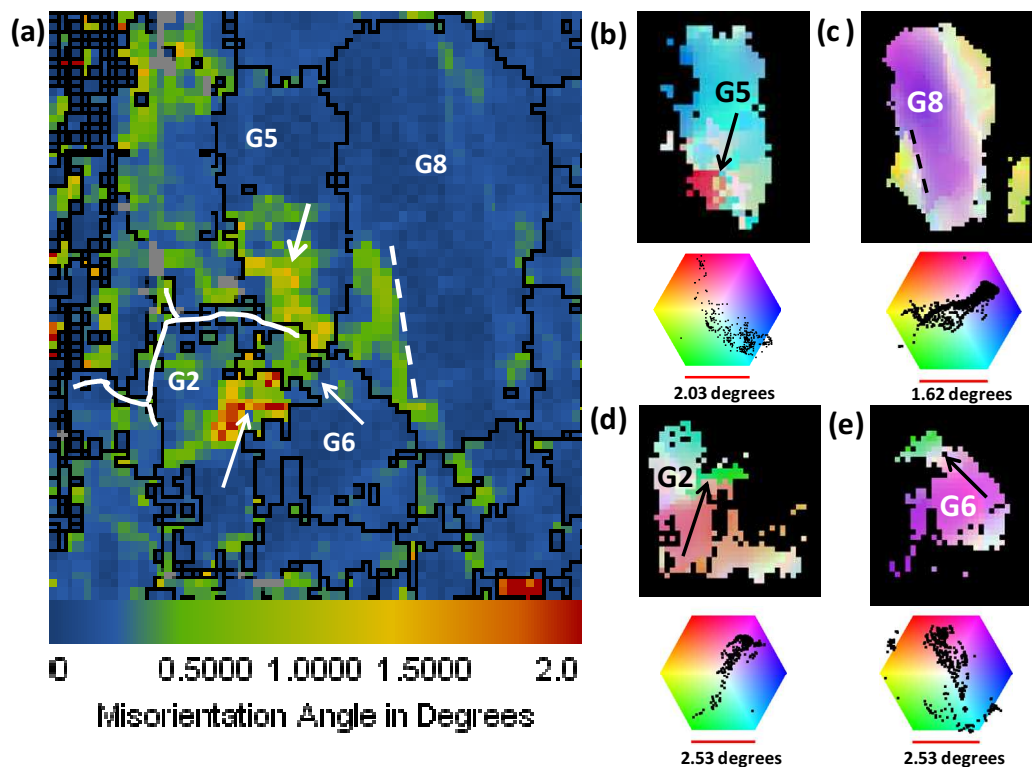


Figure 6.6 (a) Magnification of the mis-orientation map in the region of the crack tip for the 18h sample; (b-e) the zoomed-in pole figures for 4 individual grains surrounding the crack tip along with point to point orientations within each of these four grains.

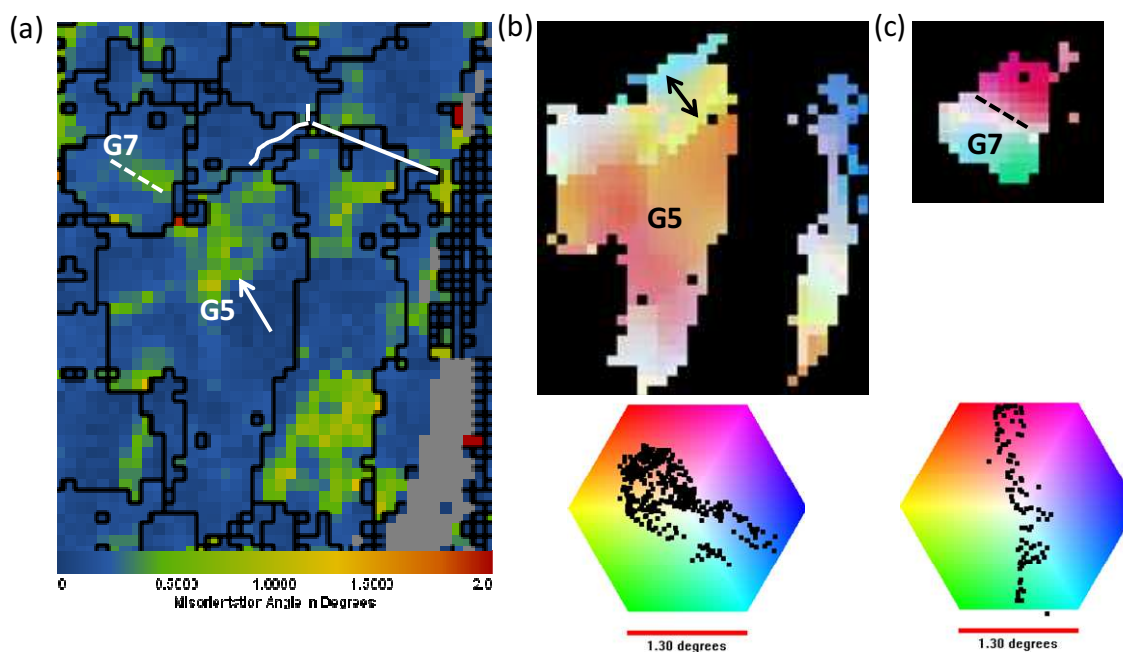


Figure 6.7 (a) Magnification of the mis-orientation map in the region of the crack tip for the 6h sample; (b-c) the zoomed-in pole figures for 2 individual grains surrounding the crack tip along with point to point orientations within each of these two grains.

In Figure 6.6 for 18h sample, the zoomed-in [001] pole figures of G5, G6, and G8 (Figures 6.6(b-f), respectively) were also investigated and compared to the respective grains in the local mis-orientation angle map (Figure 6.6(a)), and corroborate the findings from the mis-orientation angle map. An abrupt color change from purple on the right side of the dashed line in G8 (Figure 6.6(c)), to yellow to the left of the dashed line, at the triple point, indicates an approximate lattice rotation of 2.6 degrees, using the corresponding color scale. The dramatic color change in G6, from red-purple to green, towards the triple point, also indicates significant lattice rotation around the triple point. The red-colored region in G5 at the grain boundary with G6 (Figure 6.6(b); highlighted by arrow) corresponds to high pixel-to-pixel mis-orientation region in the mis-orientation angle map (Figure 6.6(a)). There is also significant lattice rotation towards the triple point. Grain G2 (Figure 6.6(e)) was also investigated as the mis-orientation angle map indicates a high degree of mis-orientation next to G6, near the triple point. The color change from red to green corresponds to an approximate lattice rotation of 4.5 degrees. In Figure 6.7 for 6h sample, the zoomed-in [001] pole figures of G5 and G7 (Figures 6.7b-c) ahead of the crack tip were also studied. The color change in G5, from light blue to golden yellow, towards the grain boundary, indicates an approximate lattice rotation of 1.4 degrees, while an lattice rotation of ~ 2.1 degrees was found in G7 as the color changes from red on one side of the dashed line to green to the other side, using the corresponding color scale. From both cases, there is evidence of crystal rotations in the regions surrounding and ahead of the crack tip, which might result from the dislocation pile-ups in these areas. These localized strain fields coincide with the triple junction where crack arrest occurs and re-initiation requires a buildup of strains at the crack front.

6.2.5 Ellipticity

The direction of major dislocation systems in the crystal is reflected in the angle of the streaking of the diffraction spots. We have devised a color scale that reflects the change in direction from the "vertical" streaks that are most normally observed in Laue pattern streaking in PXM measurements, owing to the dominating effect of the beam direction [68, 86]. This direction is assigned a red coloration: inclination of the streaking in one direction away from vertical (counter clockwise) is represented by a purple to blue

coloration, while streaking in the other direction (clockwise) results in a yellow to green coloration. The intensity of the color reflects the extent to which the streak is elongated (ellipticity). This ‘ellipticity’ map for the 18h sample is compared in Figure 6.8(c), with the orientation and local mis-orientation maps in Figures 6.8 (a) and (b), respectively.

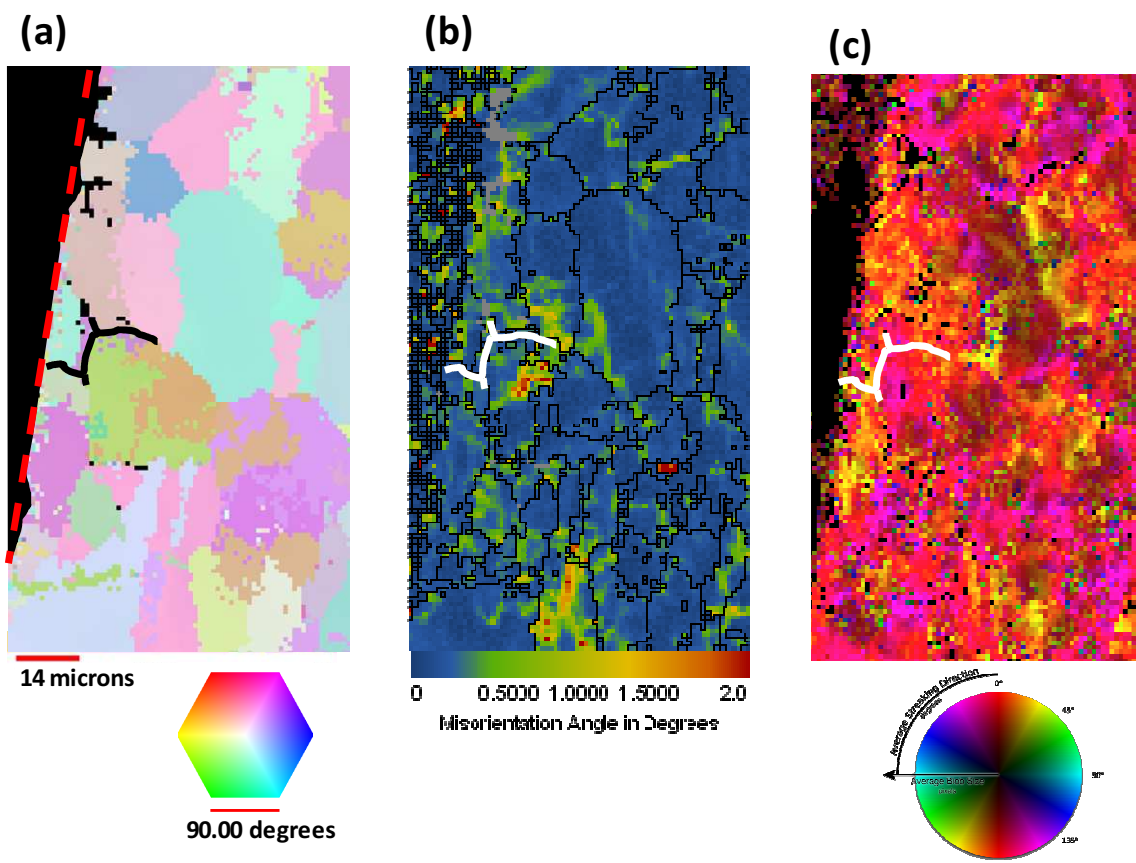


Figure 6.8 [001] Orientation map (a), local misorientation map (b) and ellipticity map (c) from the selected region of the 18h cracked C-ring sample. Color legends are located below the corresponding maps.

The area surrounding the crack in the 18h sample ellipticity map is enlarged in Figure 6.9(a), and examples of streaked Laue spots are shown in Figures 6.9(b-c). Of note in Figure 6.9(a) is the pink region at the first and second deviations in the crack path, and the yellow region in G2 at the triple point just ahead of the crack tip. These are regions where the dislocation systems are likely to be most complex (high plastic deformation) and thus might be expected to respond in a different manner to the stresses associated with crack propagation. A Laue spot from one of the indexed Laue images from the ‘pink’ region is highlighted in Figure 6.9(b), and is consistent with a tilt of

approximately 30° from the vertical in the counterclockwise direction, as indicated by the color scale. A Laue spot from the yellow region is highlighted in Figure 6.9(d), and is consistent with a tilt of approximately 30° in the clockwise direction. A Laue spot from a dark red region (region c in Figure 6.9(a)) which does not exhibit much streaking is shown in Figure 6.9c, and is consistent with the color wheel.

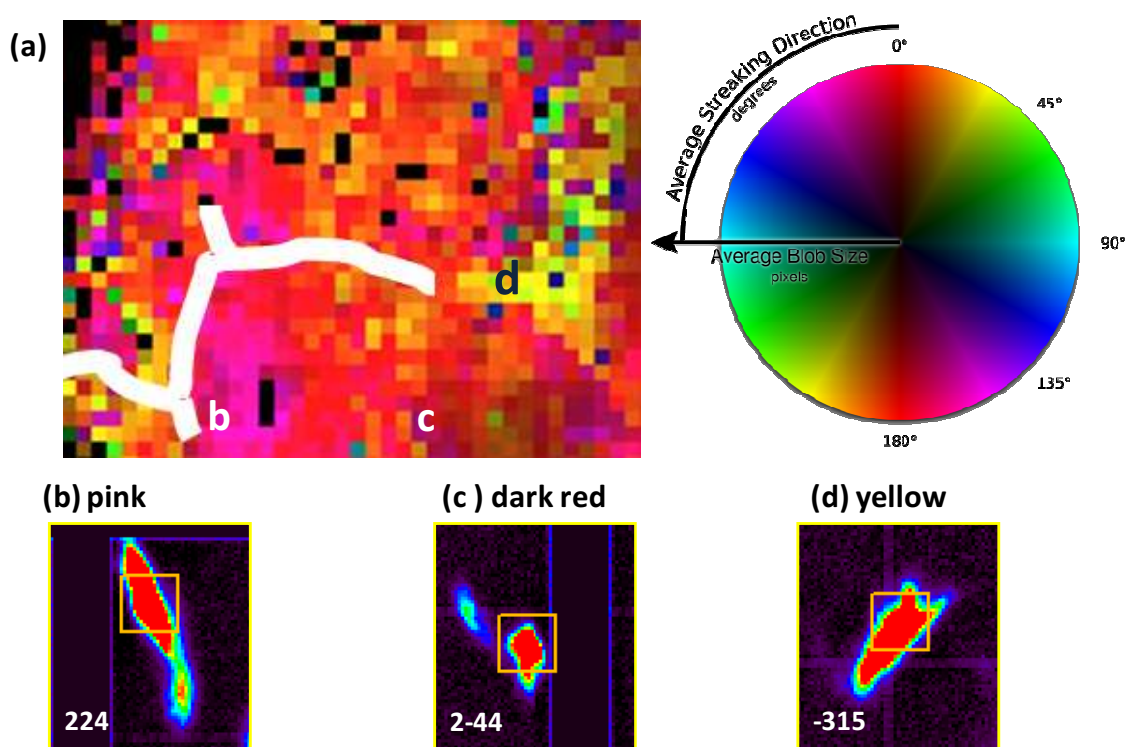


Figure 6.9 (a) Magnification of the ellipticity map in Figure 6.8 in the region of the crack tip; (b-d) show the shapes and inclinations of diffraction spots from different regions indicated in (a).

6.2.6 Slip System Modeling

An attempt was also made to model the dislocation system(s) present using a function recently implemented in XMAS. Compared to the modeling presented in Chapter 3, this is simplified modeling, without considering the splitting of the streaks, the density of GNDs, or the existence of multiple slip systems, but only the direction and the length of the streaks with one slip system. Therefore, the results from this modeling is far from satisfying the need to fit dislocations in a high stress area. However, it can still serve as an evaluation for degree of plastic deformation in the material. The modeling was applied to several Laue images from the 18h sample, but this was not

successful for most of them, presumably owing to the complexity of the Laue spots. By contrast, the streaking in the interior of G2 was able to be modeled by a single screw dislocation system in the $(-1-11)$ plane moving along a $\langle -110 \rangle$ direction, showing in Figure 6.10.

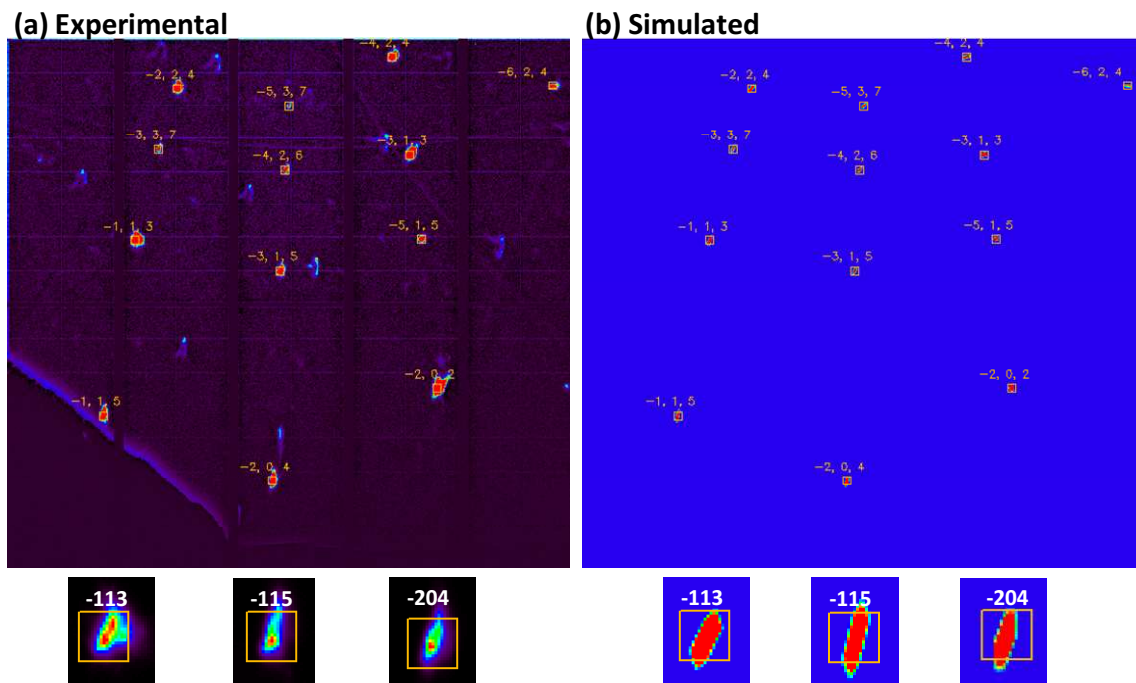


Figure 6.10 The Laue diffraction image from the interior of Grain 5 in the 18h sample. (a) experimental; (b) simulated pattern using XMAS for a single screw dislocation $(-1-11)\langle -110 \rangle$. Three indexed peaks were enlarged under the image.

6.3 Summary

Accelerated corrosion of Alloy 600 C-ring test specimens produced intergranular stress corrosion cracking (IGSCC). Tensile strains with respect to the stress axis could be identified in regions ahead of the crack tip. The crack was found to have followed grain boundaries with the lowest possible angles of mis-orientation. The direction of crack propagation may also be affected by the stress axis direction and by the accumulation of dislocations between hard and soft grains. The Schmid factor of one of the grains adjacent to the crack at the 6h and 18h initiation sites was found to be the lowest, compared to Schmid factors calculated for surface grains away from the initiation site, and also along the crack path into the bulk.

The use of the modified software – FOXMAS has significantly enhanced the information available on the crystal structure during the SCC process. First, the use of the mis-orientation information with PXM data provides a detailed measurement of plastic strains. From the local mis-orientation map of both 6h and 18h samples, a well defined region of plastic deformation is found at the triple point just ahead of the crack tip. Using the zoomed-in pole figures, the degree of the grain rotation was also estimated, which matches the change observed from the local mis-orientation. Second, the utility of the spatial mapping (ellipticity map) of changes to the shapes of diffraction spots has been demonstrated. Abrupt changes to the inclination of diffraction streaks within a particular region can signal a change in the operative dislocation systems, as shown by the pink and yellow colors around the crack and ahead of the crack tip in the 18h sample.

A simplified modeling method by XMAS was also used to simulate the Laue diffraction from the cracked samples. However, only diffraction from the interior of a relatively big grain in the 18h sample has been successfully simulated by a screw dislocation system in the (-1-11) plane moving along a $\langle -110 \rangle$ direction. This is probably due to the complexity of the diffraction peaks around grain boundaries.

In addition to strains identified with crack growth, other regions of high strain can appear as a result of the previous mechanical history of the sample. When more exacting studies of strain changes are required, it will be necessary to use pre-characterized samples, so that only incremental strain effects are measured.

Chapter 7

7. PXM and EBSD Study of the 24h SCC-cracked C-ring

A major objective of our work with PXM has been the study of strain distributions near cracks in Alloy 600 C-rings that were instigated by stress corrosion cracking (SCC). In last Chapter, two C-ring samples with small cracks ($\sim 15 \mu\text{m}$ for 6h sample and $\sim 30 \mu\text{m}$ for 18h sample) from the C-ring cross section were studied. This chapter presents studies around a massive crack ($\sim 500 \mu\text{m}$ in length) from a free surface in Alloy 600 C-ring that had been induced during electrochemically accelerated caustic corrosion in a high temperature autoclave. The content present is partly extracted from a recently accepted paper [92].

7.1 Brief Review of Experimental (Samples & Techniques)

The C-ring used for the investigation in this chapter was prepared by the same protocols as that used for the C-ring in Chapter 5. One of the flat end surface was then mechanically polished and FIB polishing was then conducted on a small area around the apex of the C-ring. Cuts and Pt lines using the ion beam were made on both sides of the polished area as markers of features in the microstructure where cracking was noticeable (see Figure 2.3 as a reference). The SCC test was then carried out on this C-ring according to the method described in section 2.2.3. After the exposure, multiple cracks were also found around the apex of the C-ring, as the 6h and 18h samples studied in Chapter 6. However, the length of the cracks observed in this sample is exceedingly bigger than those from 6h and 18h samples. Shown in Figure 7.1 is an SEM image of the cracks from the flat end surface of the 24h C-ring. Two massive cracks were observed with length of $\sim 200 \mu\text{m}$ and $\sim 500 \mu\text{m}$, respectively. PXM studies have been done on both cracks, but only results from the $\sim 500 \mu\text{m}$ were presented in this thesis. EBSD measurements were also performed on this same crack. Note that this SCC-cracked C-ring sample is different from the ones in Chapter 6, because this crack is directly on the flat end surface – a free surface, not a cross-section.

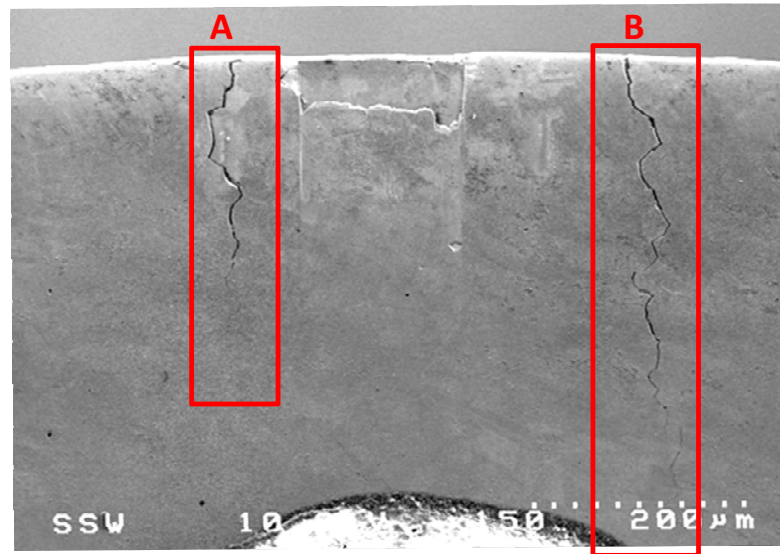


Figure 7.1 SEM image of the cracks found around the apex of the flat end surface of the 24h C-ring. Site A is a crack with length of $\sim 200 \mu\text{m}$, while site B is a crack with length of $\sim 500 \mu\text{m}$. More cracks were observed within a certain distance from the apex besides the two shown.

7.2 Results and Discussions

7.2.1 SEM Characterization

As described above, the crack on 24h sample studied is from the flat end surface (free surface) without any further treatment after SCC test. This is probably one of the major reasons that the crack size is remarkably longer than those from the 6h and 18h samples (hundreds compared to tens of microns), as the crack grew on free surface with less constraint and a more direct corrosive environment compared to the 6h and 18h cracks, which were from the cross section of the C-ring. One other possible explanation for such long crack would be that cracks were initiated at multiple sites and then linked together to form a single main crack, which was proposed by Brisson *et al.* [93]. In Figure 7.2, SEM images of the whole crack and with a higher magnification from selected locations of the 24h crack were shown. The crack propagated along a main path, but a lot of branches were also observed. Meanwhile, some isolated crack segments were displayed on the surface (as indicated by circle in Figure 7.2), which might indicate unseen crack branches below the surface. From the magnified SEM in Figure 7.2, large oxide nodules and small oxides can be seen on the surface, which are believed to be the

duplex-layer oxide as often observed by others [40, 94]. Combrade *et al.* [40] concluded that the oxide formed on Alloy 600 in primary PWR water at 360 °C was made up of two layers: (i) an external loose layer made of nickel ferrite, and (ii) an inner compact layer composed of two sublayers – an intermediate layer of a spinel-type, Cr-rich oxide and an internal layer of pure Cr₂O₃. Kim *et al.* [94] also observed the duplex-layer oxide on Alloy 600 in high temperature caustic solution. Thin oxide layer was also found along the side of the crack path, some of which was dried out and detached from the side of the crack.

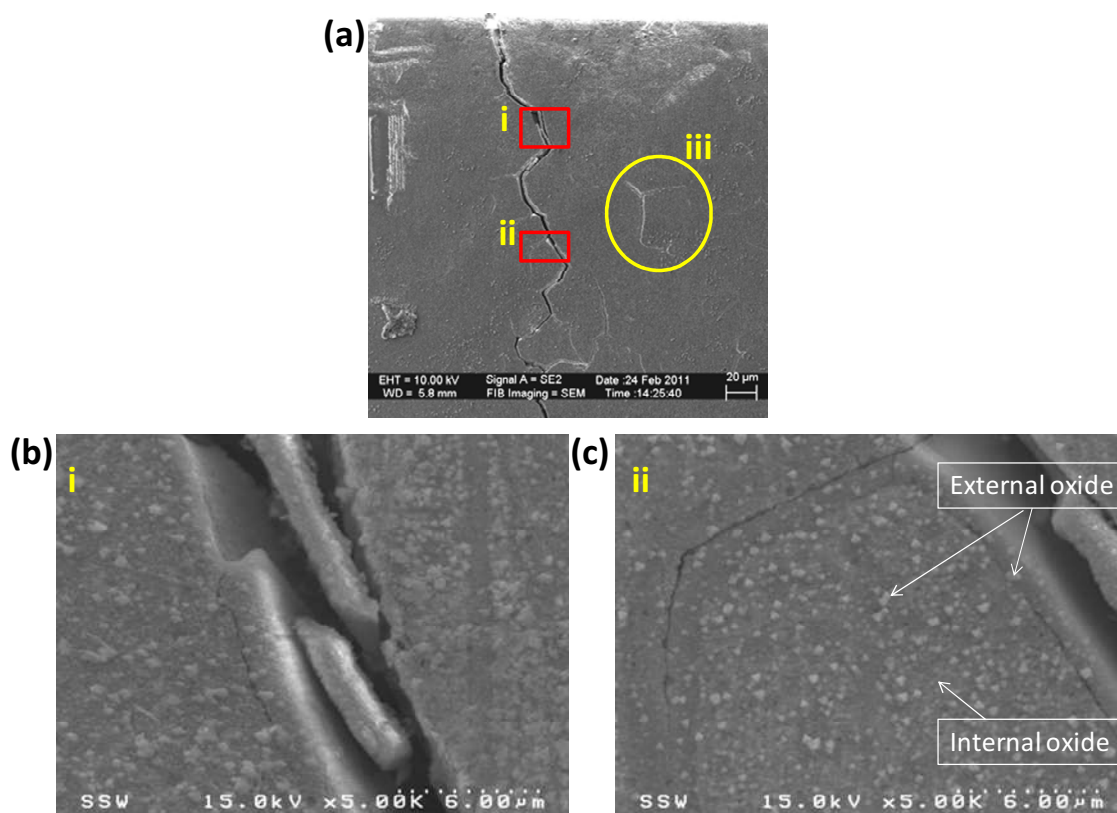


Figure 7.2 (a) SEM image of the whole crack and (b-c) enlarged SEM images from locations (i) and (ii) as outlined by red boxes in (a). Yellow circle on the image in (a) indicates an area with isolated crack segment.

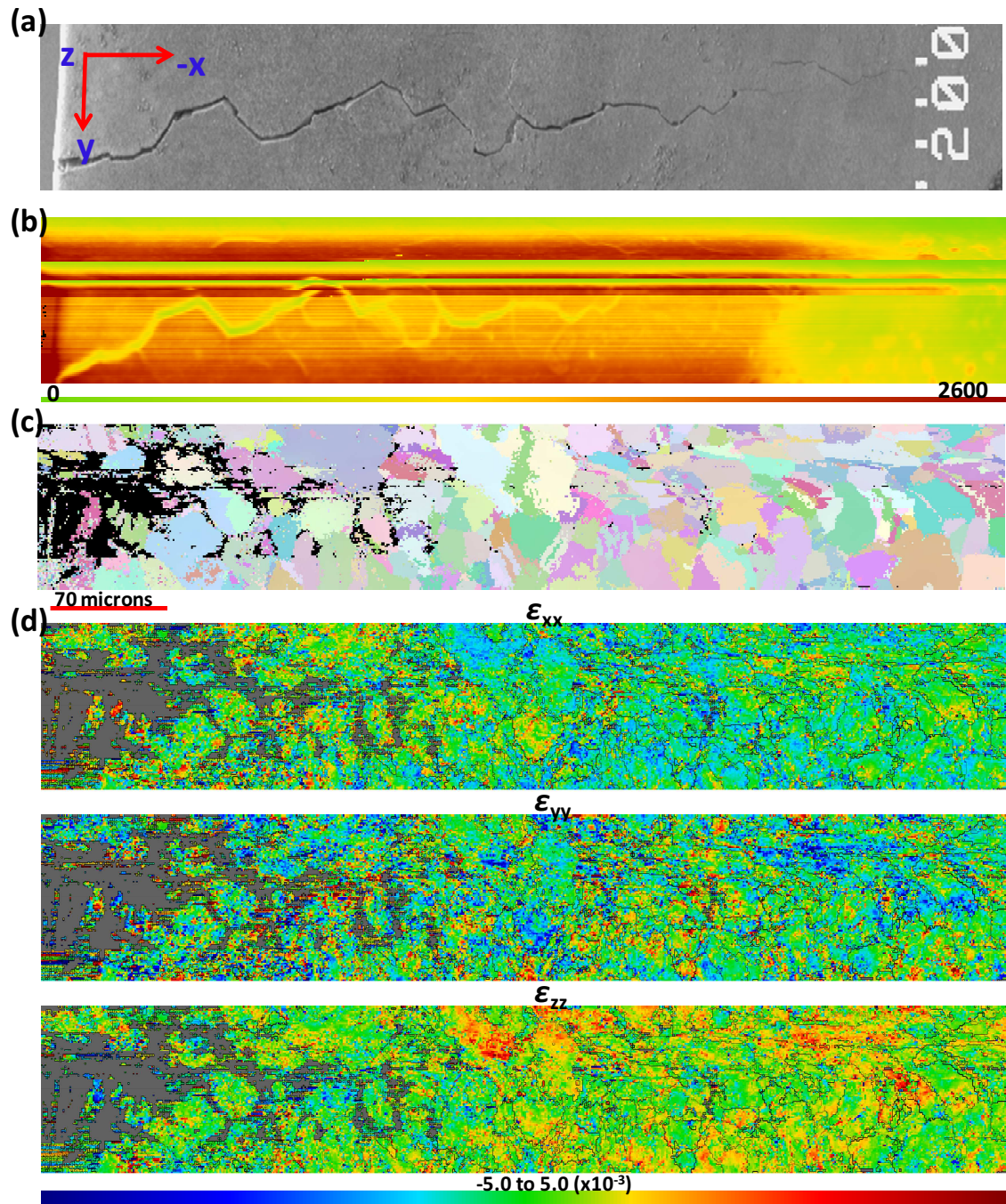


Figure 7.3 (a) SEM image of the crack area studied by PXM. The sample coordinate system is also shown on the image. The y direction is the main stress axis. (b) x-ray absorption map of the above region. A color scale with green being the lowest to red the highest absorption intensity is used. The green trail shown indicates the location of the crack path. (c) [001] orientation map and (d) the three principal deviatoric strain maps of the area covering crack from the PXM scan. A scale of -5 to $5 (\times 10^{-3})$ with color changing from blue (compressive) to red (tensile) is used.

7.2.2 PXM Measurement

An area of $580 \times 100 \mu\text{m}^2$ covering the big crack ($\sim 500 \mu\text{m}$ in length) from the crack mouth to the tips of most branches of the crack shown in the SEM image (Figure 7.3(a)) was scanned by PXM at ALS with a $1 \mu\text{m}$ step size. The sample coordinates with respect to the beam station was also shown on the SEM image in Figure 7.3(a). Since PXM detects the most intense crystalline feature within the outermost ~ 60 microns of the nickel alloy, the correlation of the crack pathway shown in the SEM image and the PXM based information, also required another confirming image of the crack path provided by the x-ray absorption image (see Figure 7.3(b)). Thus the path of the crack for most of its length could be superimposed on the remaining diffraction maps in Figure 7.3 with a high degree of confidence for at least the outer 50% of the crack length.

The [001] orientation map and the three principal deviatoric strain component maps are presented in Figure 7.3(c-d). For the most part, the main crack and its branches follow intergranular pathways. ϵ_{xx} and ϵ_{yy} show a combination of tensile and compressive strain all over the scanned area. High tensile strain was observed surrounding the big crack in ϵ_{zz} . No clear connection between this 24h crack and the deviatoric strain pattern is observed in contrast to the 6h and 18h samples (in Chapter 6). This is probably because of the high complexity of this crack.

The orientation image shows that grains near the mouth of the crack are not indexed as completely as those in the sample interior; the black patches indicate regions that could not be indexed, which is usually because of the high plastic deformation. As shown in Figure 7.4, Laue images a - c are from locations of the black areas at sample surface towards the bulk. Image a at the very surface around the crack mouth showed a totally diffuse pattern without any noticeable diffraction peaks indicating that the material in this area is nano-crystalline. From Laue images b to c, there are very few Laue spots and the ones that are present are very large and fuzzy. This indicates that the crack mouth area is poorly crystalline (reduced long range order). As a comparison, the indexed Laue image d is showing more peaks and the spots are noticeably brighter. The streaking of the spots indicates the lattice rotation.

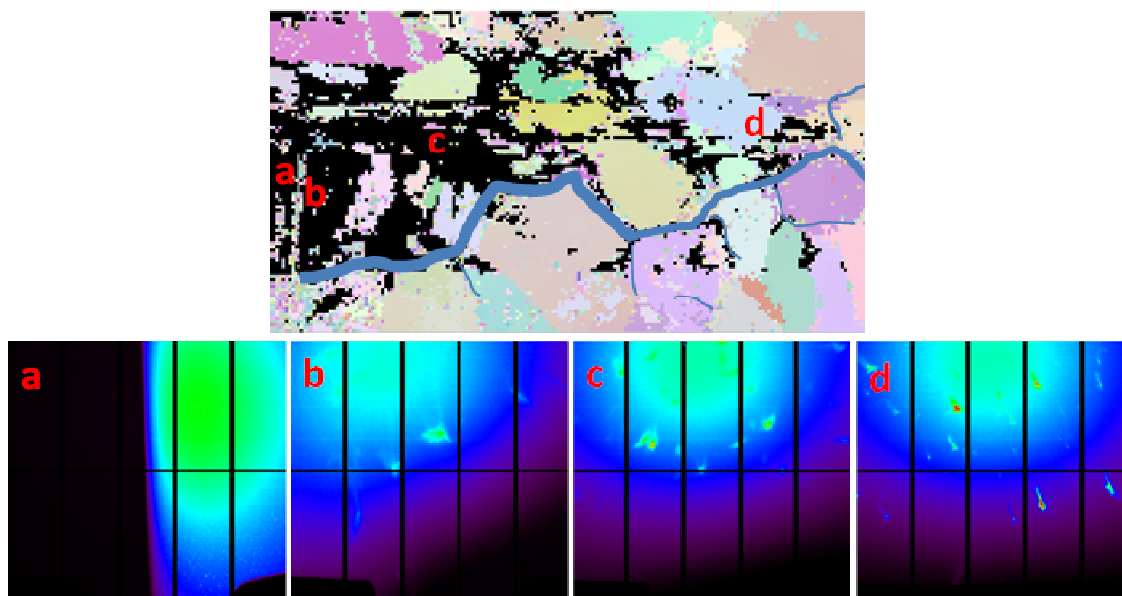


Figure 7.4 Laue diffraction images from the black areas close to the sample edge and an example of an indexed pattern further into the bulk.

A better measure of the reduced degree of crystalline order in the crack mouth area can be obtained from the index quality map in Figure 7.5(a). The index quality map was also produced by FOXMAS, which maps the number of indexed spots for each Laue pattern. Grains near the crack mouth with green and yellow colorations were indexed using 7-8 diffraction spots. By contrast, at greater depths in the sample the number of diffracting spots was generally higher, with significant variance from grain to grain. Some grains (dark red) were indexed by as many as 15 spots. Near the crack mouth local degradation of the crystalline order may result from mechanical stresses during SCC, perhaps introducing point defects and dislocations, in addition to causing the complete loss of long range order in the black areas shown in Figure 7.4.

The index quality map in Figure 7.5(a) also illuminates the grain to grain variations in crystal integrity. A grain that is able to be indexed with many spots (red) is more likely than not to have fewer dislocation systems and it may be more resistant to their transmission from neighbouring grains, i.e. "hard" [87].

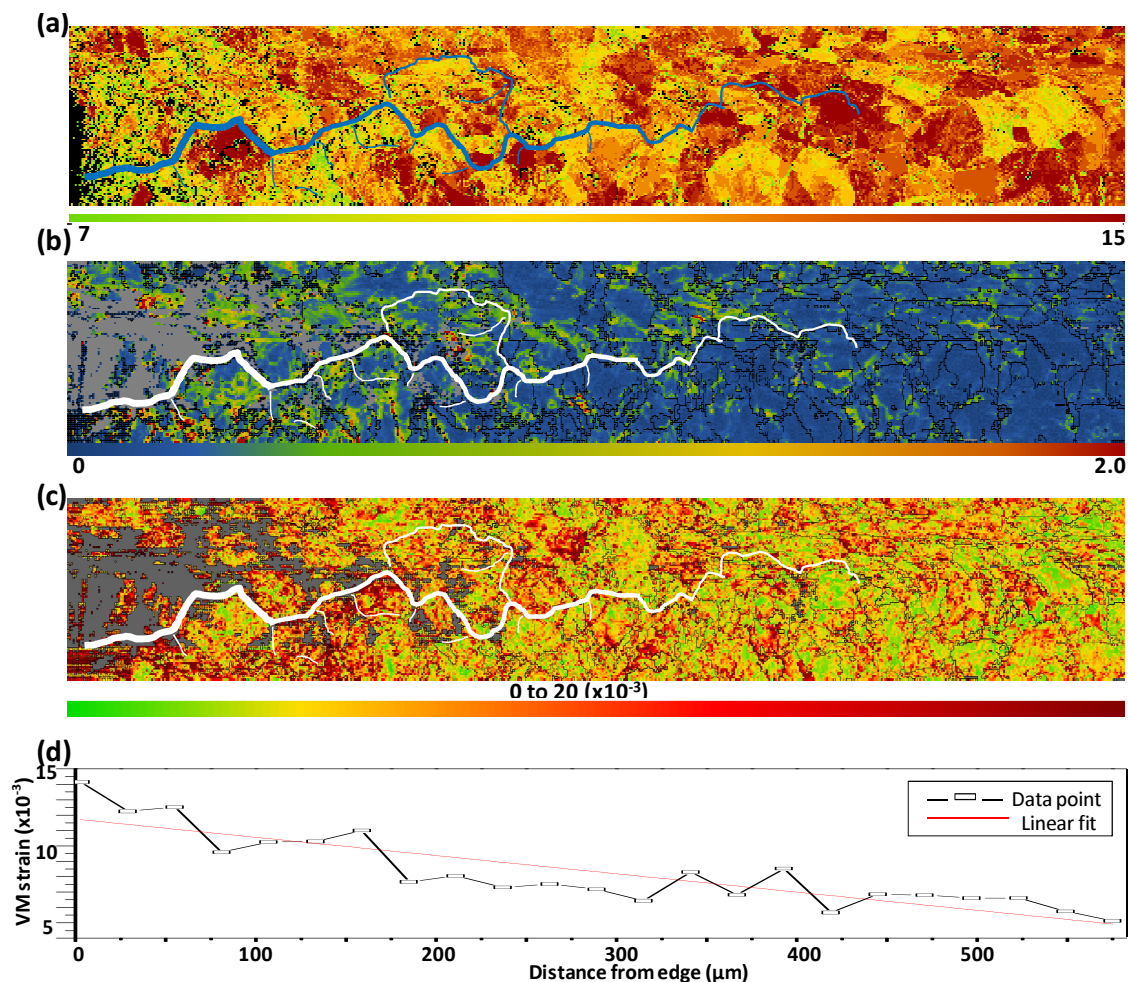


Figure 7.5 (a) Index quality map which shows number of indexed diffraction spots for each Laue pattern; (b) local mis-orientation map, an angular scale of 0-2 degrees was used; (c) von Mises strain map and (d) a plot of the average von Mises strain changing with the distance from the C-ring OD.

The local mis-orientation map and the von Mises (VM) strain map were also presented in Figure 7.5(b-c). A magnitude of 0 – 20 x 10⁻³ with color scale from green to red was used for the VM strain, while the local mis-orientation map adopted a color scale from blue to red indicating an angular magnitude of 0 – 2 degree. As described in Chapter 2, the local mis-orientation is a measure of plastic strain. A higher density of the relatively high mis-orientation angles usually indicates higher plastic strain. High plastic strain (high local mis-orientation) appears to correlate closely with the outlines of certain grain boundaries and not with others. Of particular note is a collection of bands of plastic strain in the upper left corner that extend from the surface to a depth of many tens of microns. Another prominent band extends inward from near the crack mouth. Such

bands may have resulted from the mechanical damage prior to or during the cracking event. No correlation can be discerned between the locus of the crack and the incidence of plastic stain. The composite (von Mises) elastic stain also showed higher strain around crack mouth. Although some correlation with the plastic strain in the region of the crack mouth, there are few other coincidences with each other or with the crack pathway, including areas near the tips of the crack network.

However, judging from the color scale, a general decrease of VM strain and the plastic strain from the C-ring OD (outer dimension) towards the midplane was noticed, which is likely resulting from the torsional stressing of the C-ring. It is known that the stress through the thickness in such a C-ring sample changes from a maximum tension on outer surface to a maximum compression on the inner surface. There is a stress free axis (neutral axis) in between, which is more or less around the midplane of the C-ring. In Figure 7.5(d), the average VM strain at each depth was also calculated and plotted with the distance from C-ring OD, which again showed this decrease.

7.2.3 EBSD Measurement

In Figure 7.6, the EBSD orientation map and local mis-orientation map are presented along with those from the PXM measurement. EBSD measurements were performed in such a way that as much of the same area from the PXM scan would be measured. However, only a portion of the same area around the inner portion of the crack region was able to be obtained from EBSD measurements, mainly due to the highly plastically deformed area around the crack mouth, although electropolishing was applied once again before the scan. This is one of the advantages of PXM over EBSD, as discussed previously.

For EBSD maps, the crack pathway is clearly delineated (as white) because the depth range sampled by the electron beam is only a few tenths of microns. Also, similar but not exactly the same grain structures were observed from the orientation maps of EBSD and PXM. In Figure 7.5(b), mis-orientation approaching 1 degree can be mapped along some of the grain boundaries by EBSD. As well, some mis-orientation appears to be associated with the crack itself, either as a result of local strains or from surface

roughness at the crack edge. In the case of the PXM map of plastic strain (mis-orientation), the intensities shown result from an average of reflections coming from depths of several microns. Therefore, they are thought to be less affected by surface preparation.

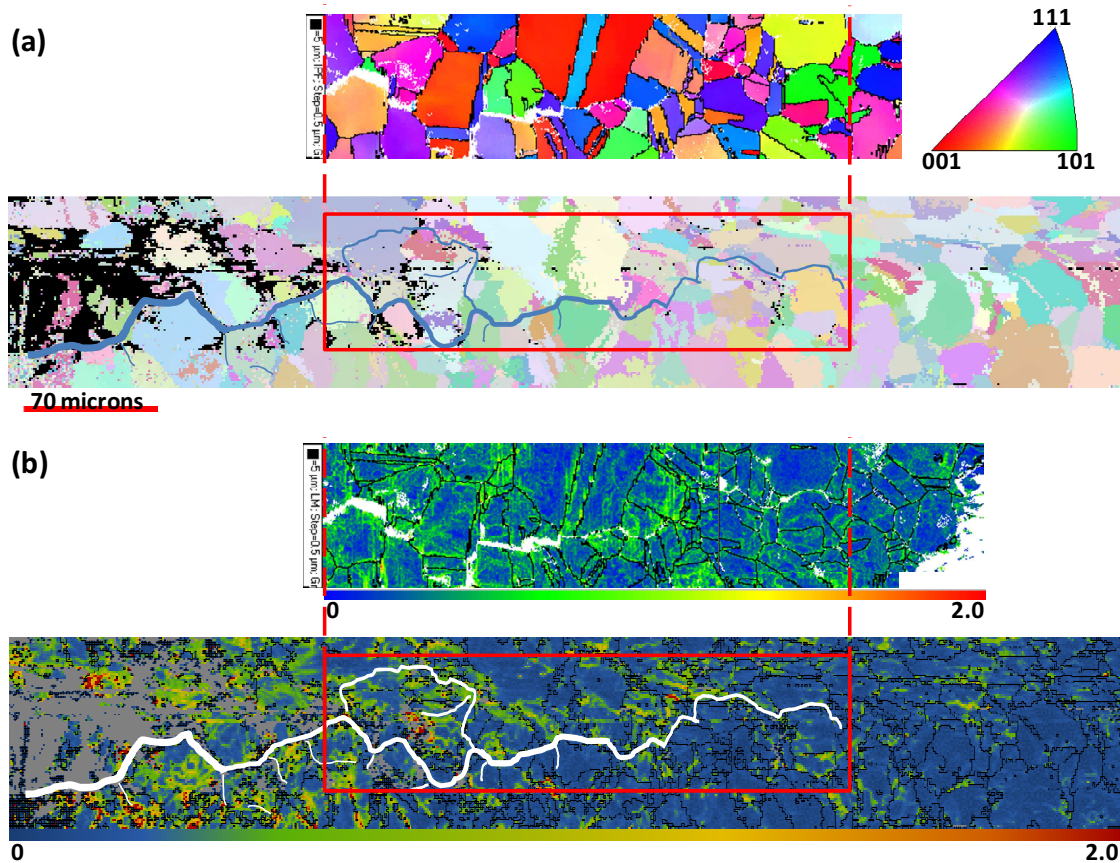


Figure 7.6 (a) Orientation maps of the large crack using EBSD and PXM. The triangle color scale for OM in EBSD is also shown; (b) local mis-orientation maps of the crack area using EBSD and PXM. The same scale 0 to 2 degrees was used. The red boxes outline the portion from which the EBSD scan was taken.

7.3 Summary

Intergranular cracks with remarkable length were produced by accelerated corrosion of Alloy 600 C-ring test specimen on the free surface. Such big cracks may be due to lower constraint and/or more corrosive environment of the free surface compared to the cross sectional cracks. Alternatively, multiple small cracks might be linked together to form a main crack with a considerable size. Duplex-layer oxides were observed on the surface.

From both PXM and EBSD studies of this crack, no obvious elastic strain or plastic deformation can be identified near any of the tips of the crack network, which is perhaps because the mechanisms of stress resolution were more complex for this crack. Another possible reason would be that the crack studied was covered by a thick oxide film, therefore the crack tips we determined from the SEM image might not be accurate, which in turn lead us to wrong locations for the expected high strain. In other words, a better way to study cracks would be fresh polished surfaces other than a surface covered with thick oxides.

Though no connection between strain and crack tips were observed, the crack mouth did show very high loss of crystallinity, probably resulting from the defects caused by mechanical stress during SCC or the concentration of chemical activity. In addition, both elastic and plastic strain were found to decrease with the depth towards the midplane of the C-ring, which reflects the result from torsional stressing of the C-ring. The index quality map generated by FOXMAS was also found to be quite useful on differentiating the crystal integrity. Higher numbers of indexed spots indicate a harder grain with higher degree of crystalline order.

Chapter 8

8. Conclusions and Future Work

8.1 Conclusions

In this thesis, the relatively new technique polychromatic x-ray microdiffraction (PXM) was used to determine the microstructure and microstrain in Alloy 600 prior to or during the stress corrosion cracking (SCC) initiation. Two main objectives were set up. First, it was necessary to assess the reliability and limits of this relatively new technique for determining the magnitude and distribution of microscopic strains in Alloy 600. Second, the changes in microstructure and microstrain distribution needed to be studied before and after SCC crack initiation. These should contribute to a better understanding of the SCC mechanisms.

8.1.1 Evaluation of PXM

This first objective was accomplished by comparing the PXM data to those from more traditional techniques – neutron diffraction and EBSD. PXM, neutron diffraction and EBSD measurements were made on tensile bar specimens uniaxially stressed to 1% nominal strain, and were presented in Chapters 3 and 4. An unstrained control specimen was also measured by these techniques.

PXM has been shown capable of detecting the strain patterns introduced to Alloy 600 specimen by a low (1%) uniaxial tensile strain. These strains were also detectable by neutron diffraction and this well-calibrated method was used to validate the PXM technique. The principal strain direction in the alloy was determined to be mostly compressive that were on the order of 100×10^{-6} ($100 \mu\epsilon$); this agrees with the strain levels measured by PXM. A more precise comparison was done by identifying grains in PXM strain maps whose directions are closest to the directions measured by neutron diffraction. The strain direction and magnitude were found to be comparable to those measured by neutron diffraction. A comparison between PXM and EBSD mapping for the same alloy was less definitive; these two techniques measure different properties.

EBSD measures plastic strain which is deducted from local mis-orientation. At this point in our use of PXM no capability for such measurements existed; only elastic strains could be measured.

PXM did show promise in its ability to detect some contributions to local plastic strains through the measurement of the distribution of dislocations. This was done by studying the elongation and splitting of PXM spots. Of particular interest was the behavior of dislocations in adjacent grains across grain boundaries of differing angular orientations. Dislocations of similar densities and directions were found on both sides of low sigma and low angle boundaries. At other boundaries there was a sharp divide with complex dislocations appearing to be blocked by the boundary, causing structural damage in the “softer” grain. This could help to predict those regions in the microstructure that may support crack propagation.

The 3D PXM was found to be particular useful in detecting differences in the plastic strain between surface and bulk of the material. This capability of 3D PXM is rather important as the plastic strain produced by any form of surface preparation will have an influence on the propagation of cracks, which is important to be distinguished from those of other metallurgical factors.

PXM has three advantages over EBSD techniques. First, using PXM, the strain resulting from both residual elastic and some level of plastic strain can be measured on a quantitative basis using changes to the lattice parameters; a separate measure of plastic strain information is obtained from any streaking of the diffraction spots and the local mis-orientation angles. Second, the information volume achieved by the x-ray beam is particularly appropriate for detecting strain information from intergranular interactions under typical stress corrosion conditions encountered by alloys used in heat transport. The PXM technique is able to measure strain directions; therefore compressive and tensile strains that occur during SCC are distinguishable and appropriate conclusions concerning the likelihood of failure can be reached.

PXM also has advantages over neutron diffraction. Firstly PXM elasto-plastic measurements are specific to a microscopic region of a metal such as particular grain or

boundary; neutron diffraction involves the measurement of thousands of grains and therefore is an averaging measurement. As well, specific information concerning plastic deformation is not available from neutron diffraction.

In short, the PXM technique appears to have the latitude and accuracy necessary to measure strain patterns caused before and during stress corrosion cracking (SCC). However, one should keep in mind that PXM is not a replacement for any other technique, as it is not as accessible due to the use of synchrotron radiation and very time-consuming. This is also the main reason that the authors have not repeated the measurements on a same sample to check the reproducibility of the PXM data, which would be a good future work if enough beam time is available. Additionally, as one of the thesis examiners pointed out that a better way to evaluate the true accuracy of the PXM, would be using single or bicrystals to verify the true local strains instead of comparing PXM with other techniques.

8.1.2 SCC Study

The SCC study was performed on C-ring samples for the second objective, as C-rings are versatile specimens for SCC test of all kinds of alloys in different forms.

The effects of stress application to C-ring sample were first discussed in Chapter 5. Compared to the unstressed C-ring, a significant higher tensile strain was observed in y direction – the main stress axis direction of the stressed C-ring as expected, so was a higher composite (von Mises) strain. Significant lattice rotation and pronounced plastic strain were also noted after stress, which were demonstrated by the study of pole figures and the peak shape changes of Laue images from the same locations of the C-ring specimen before and after stress. The confirmation of the tensile strain in y direction is rather important, as one can thus predict the preferential propagation direction of the SCC, that is, x direction when only considering the crack path on the cross sectional surface. Indeed, the cracks were found to propagate mainly along x direction in the SCC-cracked C-ring samples studied in the following chapters.

Ideally, the same stressed C-ring should be used for the subsequent SCC study. However, different C-rings were used for the SCC test with different corroding time for this study, due to the limited access to the synchrotron radiation facility.

In Chapter 6, two short intergranular cracks from the cross sectional surface of the C-rings induced by respectively 6h and 18h electrochemically accelerated corrosion in high temperature caustic solution were studied carefully by PXM. Tensile strains with respect to the stress axis were identified in regions ahead of the crack tip, so was the plastic deformation. The direction of the crack propagation was found to be mainly affected by three factors:

- (i) The grain boundary mis-orientation. The cracks were generally going along GB with the lowest possible angle of mis-orientation.
- (ii) The stress axis direction. The GBs perpendicular to the stress axis would be the ones favorably oriented for cracking. However, cracks along GBs parallel to the stress axis, the unfavorable direction were also observed, which usually require large stresses or plastic.
- (iii) The last but not the least is the accumulation of dislocations between hard and soft grains.

In addition, the Schmid factor seems to play a role in the initiation of SCC. One of the grains adjacent to the crack initiation site was found to have the lowest Schmid factor compared to those calculated for surface grains and grains along the crack path.

In Chapter 7, a massive crack on the free surface of a C-ring sample with 24h corroding time was studied by both PXM and EBSD. In comparison with the cracks studied in Chapter 6, this crack is different not just because of longer corroding time, but more importantly its location. Being on a free surface with lower constraint and/or more corrosive environment was believed to be the main reason for such a big size crack. The other explanation would be that multiple small cracks were linked together and formed a main crack with considerable size. The strain study around the crack tip was less definitive than those for 6h and 18h cracks. No obvious elastic strain or plastic deformation can be identified near any of the tips of the crack network from both PXM

and EBSD measurements. This might result from the complexity of this crack itself or the ambiguity in the location of the crack tips due to the coverage of the oxide film.

8.2.3 Use of FOXMAS

Towards the end of this project, another task was established – to test and investigate the use of the under developing PXM data processing software FOXMAS. Besides the conventional orientation maps and strain maps, local mis-orientation maps, ellipticity maps and the index quality map generated by FOXMAS were found very useful.

The local mis-orientation maps were produced with the same convention as those used in EBSD. They provide an intuitional view of the distribution of plastic deformation. The ellipticity maps assess the direction and length of streaks in a Laue image. Abrupt changes to the inclination of diffraction streaks within a particular region can signal a change in the operative dislocation systems, which can be easily discovered by the color in the ellipticity maps. The index quality maps provide information about numbers of indexed spots within each Laue image. They were found to be quite useful on differentiating the crystal integrity. Higher numbers of indexed spots indicate a harder grain with higher degree of crystalline order.

Generally, FOXMAS has shown its capabilities on strain studies in Alloy 600 C-rings. It is a comparable software for processing Laue images to XMAS, but with more than an order of magnitude faster speed.

8.2 Value and Implication

The major objective of this research program is to determine the microstrain distribution prior to or during the SCC initiation with the relatively new technique PXM. The work outlined in this study has shown that the local strains measured by PXM are quantitatively consistent with those from the more traditional technique neutron diffraction, while some qualitative correspondence was observed between PXM and EBSD. Moreover, the PXM has also presented its ability to access local plastic

deformation by assessing the streaking/splitting of the Laue peaks and the local mis-orientation.

The work presented in this thesis also exploited the PXM to the study of SCC in C-ring samples. From the study of two short cracks at the cross-sectional surface of the C-ring samples, local elastic strain as well as local plastic deformation were observed around and ahead of the crack tip, which agrees with the observations from previous studies. These localized strain fields coincide with the triple junctions where crack arrest occurs and re-initiation requires a buildup of strains at the crack front. As a comparison, the PXM study on the massive crack from a free surface of the C-ring sample was more difficult to interpret, presumably due to the complexity of the crack itself.

Overall, the PXM has shown great promise in its ability to detect either elastic or plastic strains in uniaxially tensile samples and C-ring samples, as well as the changes of microstructure and microstrain induced by SCC. Indeed, the PXM has advantages over neutron diffraction and EBSD in SCC study, however, it should be only used as a complementary method to others because of its low accessibility.

8.3 Future Work

This thesis has shown the promise of PXM in studying the SCC in Alloy 600. Future works based on the studies undertaken in this thesis are described below.

First, the 3D PXM measurements could be applied to the C-ring samples, especially around the crack tip area. As discussed before, the 2D PXM is able to give enough information about the microstructure and microstrain, however, it does show the effects of the accumulation from both surface and lower grains as the x-ray penetrates up to $\sim 60 \mu\text{m}$ into Alloy 600 samples. Therefore, it is worth to apply 3D PXM at regions of interest (crack tip and the triple point ahead) to get a clearer view of the origin and distribution of the microstructure and strain, though fair amount of time would be required.

Second, as mentioned before, the best way to study the SCC is to use a pre-characterized sample, so no effects other than those from SCC will stand out. The

stressed C-ring studied in Chapter 5 is a good candidate for this purpose. However, to catch the moment for crack initiation, the C-rings are not good choices, as they were found to easily be cracked with length at tens microns even within 6h. A better candidate is a sample with very low residual strain before cracking, so it can be subjected to successive SCC test until a crack is found and characterize the sample at a same area between each exposure to follow the changes. A control bar sample with 12h the same SCC test as the C-rings was studied at the same time at ALS, for which the results were not shown in this thesis. No cracks were found with even 12h SCC test. From the maps shown in Figure 8.1, very low elastic strain and plastic deformation were observed. This sample is therefore a good one for the SCC initiation study.

Third, a more careful study can be carried out on the 24h C-ring sample presented in Chapter 7. As discussed previously, the oxide film on the surface might be shielding the real crack tip, so what can be done is to remove the oxide film and relocate the crack tip. Then examine the PXM results with the new location of crack tip. The next step is to embed this C-ring and polish it until a cross-sectional crack is revealed, as the same procedure for the 6h and 18h C-ring. Then study this cross-sectional crack with PXM, to clarify the differences observed from the free surface crack of the 24h C-ring and other cross-sectional cracks.

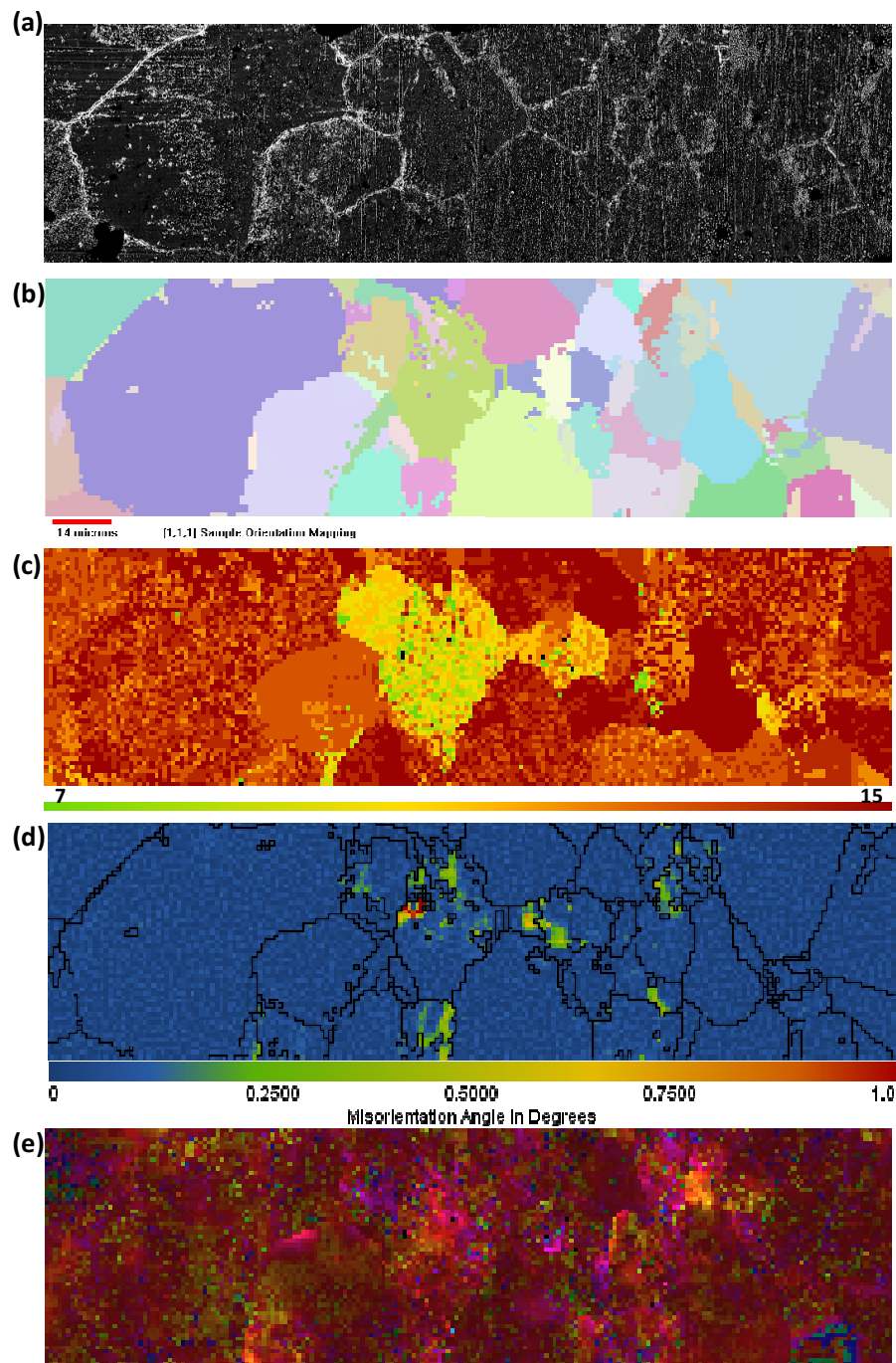


Figure 8.1 (a) SEM image of the bar sample surface after a 12h SCC test; (b-e) OM, index quality map, local mis-orientation map and ellipticity map of the area shown in the SEM image obtained from PXM.

References

1. G. H. Koch, M. P. H. Brongers, N. G. Thompson, Y. P. Virmani, J. H. Payer, "Corrosion Costs and Preventive Strategies in the United States" U.S. Rep. No. *FHWA-RD-01-156* (2002).
2. L. S. V. Delinder, Ed., *Corrosion Basics: An Introduction*, (National Association of Corrosion Engineers, ed. 1, 1984).
3. P. A. Schweitzer, *Fundamentals of Corrosion: Mechanisms, Causes, and Preventative Methods*. (CRC Press, 2009).
4. B. F. Brown, in *Stress Corrosion Cracking of Metals - a State of the Art*, H. L. Craig, Ed. (ASTM International, 1972), vol. 518, pp. 3-15.
5. U. C. Kim, K. M. Kim, E. H. Lee, *J. Nucl. Mater.* **341**, 169-174 (2005).
6. F. Meng, J. Wang, E.-H. Han, W. Ke, *Corros. Sci.* **51**, 2761-2769 (2009).
7. A. Mignone, M. F. Maday, A. Borello, M. Vittori, *Corrosion* **46**, 57-65 (1990).
8. I.-G. Park, C.-S. Lee, S.-S. Hwang, H.-P. Kim, J.-S. Kim, *Met. Mater. Int.* **11**, 401-409 (2005).
9. Y. S. Park, J. R. Galvele, A. K. Agrawal, R. W. Staehle, *Corrosion* **34**, 413-418 (1978).
10. G. Sui, J. M. Titchmarsh, G. B. Heys, J. Congleton, *Corros. Sci.* **39**, 565-587 (1997).
11. F. C. Campbell, in *Elements of Metallurgy and Engineering Alloys*, F. C. Campbell, Ed. (ASM International, 2008), Chap. 29, pp. 547-562.
12. M. F. Ashby, *Philos. Mag.* **21**, 399-424 (1970).
13. L. P. Kubin, A. Mortensen, *Scripta Mater.* **48**, 119-125 (2003).
14. D. Hull, D. J. Bacon, in *Introduction to Dislocations*. (Elsevier, 2001), Chap. 1, pp. 1-20.
15. T. Ohashi, R. I. Barabash, J. W. L. Pang, G. E. Ice, O. M. Barabash, *Int. J. Plasticity* **25**, 920-941 (2009).
16. G. Palumbo, K. T. Aust, in *Materials Interfaces : Atomic-Level Structure and Properties*, D. Wolf, S. Yip, Eds. (Springer, London, 1992), Chap. 5, pp. 190-211.

17. V. Randle, *The Role of the Coincidence Site Lattice in Grain Boundary Engineering*. (Institute of Materials, 1996).
18. V. Randle, *Mater. Charact.* **47**, 411-416 (2001).
19. D. G. Brandon, *Acta Metall.* **14**, 1479-1484 (1966).
20. G. Palumbo, K. T. Aust, E. M. Lehockey, U. Erb, P. Lin, *Scripta Mater.* **38**, 1685-1690 (1998).
21. O. Engler, V. Randle, *Introduction to Texture Analysis: Macrotecture, Microtexture, and Orientation Mapping*. (CRC Press, 2009).
22. S. S. Hwang, D. H. Hur, J. H. Han, J. S. Kim, *Nucl. Eng. Des.* **217**, 237-245 (2002).
23. K. Stiller, J.-O. Nilsson, K. Norring, *Metall. Mater. Trans. A* **27**, 327-341 (1996).
24. M.-C. Tsai, W.-T. Tsai, J.-T. Lee, *Corros. Sci.* **34**, 741-757 (1993).
25. G. Was, H. Tischner, R. Latanision, *Metall. Mater. Trans. A* **12**, 1397-1408 (1981).
26. G. S. Was, *Corrosion* **46**, 319-330 (1990).
27. C. M. Younes, F. H. Morrissey, G. C. Allen, P. McIntyre, *Brit. Corros. J.* **32**, 185-192 (1997).
28. D. Crawford, G. Was, *Metall. Mater. Trans. A* **23**, 1195-1206 (1992).
29. V. Y. Gertsman, S. M. Bruemmer, *Acta Mater.* **49**, 1589-1598 (2001).
30. S. H. Kim, U. Erb, K. T. Aust, *Scripta Mater.* **44**, 835-839 (2001).
31. P. Lin, K. T. Aust, G. Palumbo, U. Erb, *Scripta Metall. Mater.* **33**, 1387-1392 (1995).
32. E. A. West, G. S. Was, *J. Nucl. Mater.* **408**, 142-152 (2011).
33. R. Rios, T. Magnin, D. Noel, O. de Bouvier, *Metall. Mater. Trans. A* **26**, 925-939 (1995).
34. R. W. Smith, *Model. Simul. Mater. Sci. Eng.* **8**, 629 (2000).
35. S. L. Hong, *Corrosion* **57**, 323-333 (2001).
36. J. Hou, Q. J. Peng, Z. P. Lu, T. Shoji, J. Q. Wang, E. H. Han, W. Ke, *Corros. Sci.* **53**, 1137-1142 (2011).

37. S. Yamazaki, Z. Lu, Y. Ito, Y. Takeda, T. Shoji, *Corros. Sci.* **50**, 835-846 (2008).
38. A. Pakravan, thesis, University of Toronto (2010).
39. J. Panter, B. Viguiet, J. M. Clou, M. Foucault, P. Combrade, E. Andrieu, *J. Nucl. Mater.* **348**, 213-221 (2006).
40. P. Combrade, P. M. Scott, M. Foucault, E. Andrieu, P. Marcus, paper presented at the 12th International Conference on Environmental Degradation of Materials in Nuclear Power System - Water Reactors, T. R. Allen, P. J. King, L. Nelson, Eds. (TMS, 2005), pp. 883-890.
41. W. T. Tsai, M. J. Sheu, J. T. Lee, *Corros. Sci.* **38**, 33-45 (1996).
42. D.-J. Kim, H. Kim, S. Hwang, J. Kim, J. Park, *Met. Mater. Int.* **16**, 259-266 (2010).
43. R. W. Staehle, paper presented at the 12th International Conference on Environmental Degradation of Materials in Nuclear Power System - Water Reactors, T. R. Allen, P. J. King, L. Nelson, Eds. (TMS, 2005), pp. 1163-1209.
44. R. Bandy, D. Vanrooyen, *J. Mater. Eng.* **7**, 237-245 (1985).
45. F. H. Hua, R. B. Rebak, in *Environment-Induced Cracking of Materials*. (Elsevier, 2008), pp. 123-141.
46. D. A. Jones, *Corros. Sci.* **52**, 356-362 (1996).
47. R. C. Newman, in *Corrosion Mechanisms in Theory and Practice*, P. Marcus, Ed. (CRC Press, 2002), Chap. 11, pp. 399-450.
48. R. B. Rebak, Z. Szklarska-Smialowska, *Corros. Sci.* **38**, 971-988 (1996).
49. P. M. Scott, paper presented at the 9th International Symposium on Environmental Degradation of Materials in Nuclear Power Systems - Water Reactors, F.P. Ford, S.M. Bruemmer, G.S. Was, Eds. (TMS, 1999), pp. 3-12.
50. P. M. Scott, M. L. Calvar, paper presented at the Sixth International Symposium on Environmental Degradation of Materials in Nuclear Power Systems--Water Reactors, R. E. Gold, E. P. Simonen, Eds. (TMS, 1993), pp. 657-665.
51. T. M. Angeliu, D. J. Paraventi, G. S. Was, *Corrosion* **51**, 837-848 (1995).
52. G. Was, J. Sung, T. Angeliu, *Metall.Mater. Trans. A* **23**, 3343-3359 (1992).
53. C. Cheung, U. Erb, G. Palumbo, *Mater. Sci. Eng. A* **185**, 39-43 (1994).
54. G. Was, V. Thaveeprungsriporn, D. Crawford, *J. O. M.* **50**, 44-49 (1998).

55. T. Sham, M. Rivers, *Rev. Mineral. Geochem.* **49**, 117-147 (2002).
56. <http://www.synchrotron.org.au/index.php/synchrotron-science/how-is-synchrotron-light-created>.
57. R. Barabash, G. E. Ice, B. C. Larson, G. M. Pharr, K. S. Chung, W. Yang, *Appl. Phys. Lett.* **79**, 749-751 (2001).
58. R. I. Barabash, G. E. Ice, B. C. Larson, W. G. Yang, *Rev. Sci. Instrum.* **73**, 1652-1654 (2002).
59. G. S. Cargill, *Nature* **415**, 844-845 (2002).
60. A. Lee, W. Liu, C. E. Ho, K. N. Subramanian, *J. Appl. Phys.* **102**, (2007).
61. M. L. Suominen Fuller, R. J. Klassen, N. S. McIntyre, A. R. Gerson, S. Ramamurthy, P. J. King, W. Liu, *J. Nucl. Mater.* **374**, 482-487 (2008).
62. N. Tamura, R. S. Celestre, A. A. MacDowell, H. A. Padmore, R. Spolenak, B. C. Valek, N. M. Chang, A. Manceau, J. R. Patel, *Rev. Sci. Instrum.* **73**, 1369-1372 (2002).
63. W. Yang, B. C. Larson, J. Z. Tischler, G. E. Ice, J. D. Budai, W. Liu, *Micron* **35**, 431-439 (2004).
64. J. S. Chung, G. E. Ice, *J. Appl. Phys.* **86**, 5249-5255 (1999).
65. G. E. Ice, B. C. Larson, W. Yang, J. D. Budai, J. Z. Tischler, J. W. L. Pang, R. I. Barabash, W. Liu, *J. Synchrotron Radiat.* **12**, 155-162 (2005).
66. G. E. Ice, J. W. L. Pang, *Mater. Charact.* **60**, 1191-1201 (2009).
67. N. Tamura, A. A. MacDowell, R. Spolenak, B. C. Valek, J. C. Bravman, W. L. Brown, R. S. Celestre, H. A. Padmore, B. W. Batterman, J. R. Patel, *J. Synchrotron Radiat.* **10**, 137-143 (2003).
68. R. I. Barabash, G. E. Ice, in *Encyclopedia of Materials: Science and Technology* K. H. J. Buschow *et al.*, Eds. (Elsevier, Oxford, 2005), pp. 1-18.
69. R. I. Barabash, G. E. Ice, J. W. L. Pang, *Mater. Sci. Eng. A* **400**, 125-131 (2005).
70. S. I. Wright, M. M. Nowell, D. P. Field, *Microsc. Microanal.* **17**, 316-329 (2011).
71. L. N. Brewer, M. A. Othon, L. M. Young, T. M. Angeliu, *Microsc. Microanal.* **12**, 85-91 (2006).
72. M. Kamaya, *Mater. Charact.* **60**, 125-132 (2009).
73. M. Kamaya, A. J. Wilkinson, J. M. Titchmarsh, *Acta Mater.* **54**, 539-548 (2006).

74. Z. Lu, T. Shoji, S. Yamazaki, K. Ogawa, *Corros. Sci.* **58**, 211-228 (2012).
75. S. C. Vogel, H.-G. Priesmeyer, *Rev. Mineral. Geochem.* **63**, 25-57 (2006).
76. G. Dieter, in *Mechanical Metallurgy*. (McGraw-Hill Science, 1986), pp. 70-100.
77. ASTM, in *Metals Test Methods and Analytical Procedures*. (Annual Book of ASTM Standards, 1993), pp. 150-155.
78. D. H. Hur, J. S. Kim, J. S. Baek, J. G. Kim, *Corrosion* **58**, 1031-1038 (2002).
79. N. Pessall, G. P. Airey, B. P. Lingenfelter, *Corrosion* **35**, 100-107 (1979).
80. B. L. Bramfitt, A. O. Benschoter, in *Metallographer's Guide: Practices and Procedures for Irons and Steels*. (ASM International, 2002), Chap. 8, pp. 215-244.
81. N. Sherry, J. Qin, M. S. Fuller, Y. Xie, O. Mola, M. Bauer, N. S. McIntyre, D. Maxwell, D. Liu, E. Matias, C. Armstrong, *Rev. Sci. Instrum.* **submitted**, (2012).
82. J. Chao, A. Mark, M. L. S. Fuller, N. S. McIntyre, R. A. Holt, R. J. Klassen, W. Liu, *Mater. Sci. Eng. A* **524**, 20-27 (2009).
83. J. Chao, A. Mark, M. L. Suominen Fuller, R. I. Barabash, N. Stewart McIntyre, R. A. Holt, R. J. Klassen, W. Liu, *Mater. Res. Soc. Symp. Proc.* **1137**, 1137-EE10-28 (2008), doi:10.1557/PROC-1137-EE10-28.
84. J. Chao, A. F. Mark, M. L. S. Fuller, N. S. McIntyre, R. A. Holt, O. Yong, R. J. Klassen, L. W. M. Lau, S. Ramamurthy, "Assessment of the Validity of Polychromatic X-Ray Microdiffraction (Pxm) for Strain Studies of Alloy 600" *Rep. No. COG-08-4070* (CANDU Owners Group Inc., 2009).
85. T. M. Holden, R. A. Holt, A. P. Clarke, *Mater. Sci. Eng A* **246**, 180-198 (1998).
86. R. I. Barabash, G. E. Ice, B. C. Larson, W. Yang, in *From Semiconductors to Proteins: Beyond the Average Structure*, S. J. L. T. M. F. Billinge, Ed. (Springer, 2002), pp. 49-66.
87. E. M. Lehockey, A. Brennenstuhl, S. Pagan, M. Clark, G. Ogundele, paper presented at the Proceedings of the 13th International Conference on Degradation in Nuclear Materials-Light Water Reactors., (CNS, 2007), pp. 465-478.
88. J. Chao, M. L. S. Fuller, N. S. McIntyre, A. G. Carcea, R. C. Newman, M. Kunz, N. Tamura, *Acta Mater.* **60**, 781-792 (2012).
89. R. I. Barabash, G. E. Ice, F. J. Walker, *J. Appl. Phys.* **93**, 1457-1464 (2003).
90. M. Hansel, C. A. Boddington, D. J. Young, *Corros. Sci.* **45**, 967-981 (2003).

91. R. Arone, *Eng. Fract. Mech.* **9**, 241-249 (1977).
92. J. Chao, M. L. S. Fuller, N. Sherry, J. Qin, N. S. McIntyre, J. Ulaganathan, A. G. Carcea, R. C. Newman, M. Kunz, N. Tamura, *Acta Mater.* **60**, 5508-5515 (2012).
93. B. W. Brisson, R. G. Ballinger, A. R. McIlree, *Corrosion* **54**, 504-514 (1998).
94. D.-J. Kim, H. C. Kwon, H. W. Kim, S. S. Hwang, H. P. Kim, *Corros. Sci.* **53**, 1247-1253 (2011).

Appendix I Angle calculation from PXM data for Chapter 3

This appendix presents an example of calculation for the angle between a direction [111] in crystal coordinates system and the neutron diffraction coordinates RD, ND and TD from PXM data.

Necessary input: the rotation matrix from crystal coordinates to sample coordinates.

Example:

Here is the index file from 3D PXM of the mid-bar tensile sample

```
E:\APS-oct07\1p-wire-reconIDL\1p-wire-reconIDL\1per_wire_801_76.SPE
number of grains found: 1
grain no: 0
number of indexed reflections: 11
  x(exp)      y(exp)      h      k      l      ang.dev.  xdev(pix)  ydev(pix)  E(kev)  theta(deg)
615.61444    59.51532    1      3      3      0.01465   -0.23875   -0.04134   8.98668  57.79113
949.95007    616.08917   1      7      3      0.00708   -0.11118   0.04613   20.68222  40.38016
889.15118    227.11414   1      7      5      0.01327   -0.23190   0.06709   19.07503  52.37110
240.45776    544.80511   2      2      2      0.02178   0.28487   -0.21331   9.01085   42.11468
486.99927    189.58180   2      4      4      0.01044   -0.01809   -0.16773   12.94916  53.92779
701.37762    395.56982   2      6      4      0.02806   -0.39065   -0.16208   17.78156  47.23387
521.76599    636.34558   3      5      3      0.06654   0.43898   0.90089   18.16786  39.02227
612.06287    404.33063   3      7      5      0.01274   0.16597   -0.08724   21.75512  46.92931
538.12854    135.22473   3      7      7      0.00556   0.03280   0.08529   21.86197  55.62671
112.58064    207.62813   4      4      6      0.02745   -0.23797   -0.45625   18.16916  52.34613
386.48172    311.89355   4      6      6      0.02040   -0.13678   -0.28341   21.40166  49.87288
dev1, dev2, pixdev= 0.0164300  0.0153900  0.332901
matrix X Y Z -> h k l
-0.2667261958 -0.1868066341  0.1423213333
 0.2139080167 -0.1043602154  0.2639076710
-0.0969301015  0.2837378681  0.1907677352
matrix h k l -> X Y Z
-2.1119308472  1.6937179565 -0.7674899101
-1.4791300297 -0.8263214231  2.2466287613
 1.1268965006  2.0896139145  1.5104938745
  x(exp)      y(exp)      h      k      l      E(kev)  theta(deg)
 773.11127    847.31134   1      3      1     10.62710  32.98481
 848.88068    399.49713   1      5      3     14.09321  47.07741
 608.38574    690.91071   2      4      2     14.10973  37.27711
 773.11127    847.31134   2      6      2     21.25419  32.98481
  65.28474    105.78689   3      3      5     13.97583  54.93261
 423.99872    263.90894   3      5      5     17.12146  51.49842
unindexed reflections: 10
```

The matrix $hkl \rightarrow XYZ$ is used for this calculation, as highlighted with blue box above.

1. matrix $hkl \rightarrow XYZ$

$$\begin{bmatrix} a_{11} & a_{12} & a_{13} \\ a_{21} & a_{22} & a_{23} \\ a_{31} & a_{32} & a_{33} \end{bmatrix} = \begin{bmatrix} -2.1119308472 & 1.6937179565 & -0.7674899101 \\ -1.4791300297 & -0.8263214231 & 2.2466287613 \\ 1.1268965006 & 2.0896139145 & 1.5104938745 \end{bmatrix}$$

$$h, k, l = 1, 1, 1$$

2. Calculate [111] from crystal coordinate system to sample coordinate system

$$\begin{pmatrix} X_1 \\ Y_1 \\ Z_1 \end{pmatrix} = \begin{pmatrix} a_{11} & a_{12} & a_{13} \\ a_{21} & a_{22} & a_{23} \\ a_{31} & a_{32} & a_{33} \end{pmatrix} \begin{pmatrix} h \\ k \\ l \end{pmatrix} = \begin{pmatrix} a_{11} * h + a_{12} * k + a_{13} * l \\ a_{21} * h + a_{22} * k + a_{23} * l \\ a_{31} * h + a_{32} * k + a_{33} * l \end{pmatrix}$$

$$\begin{aligned} \implies X_1 &= -1.185702801 \\ Y_1 &= -0.058822691 \\ Z_1 &= 4.72700429 \end{aligned}$$

3. Calculate the angle to RD, TD and ND (show one calculation for RD). Referring to the Figure 2.4 in Chapter 2, the directions RD, TD and ND in neutron diffraction are the

exact equivalents of x, y and z in PXM, which means RD = $\begin{pmatrix} 1 \\ 0 \\ 0 \end{pmatrix}$, TD = $\begin{pmatrix} 0 \\ 1 \\ 0 \end{pmatrix}$ and ND = $\begin{pmatrix} 0 \\ 0 \\ 1 \end{pmatrix}$ in sample coordinate system in PXM.

To RD $X_2=1, Y_2=0, Z_2=0$,

$$\cos \phi = \frac{X_1 X_2 + Y_1 Y_2 + Z_1 Z_2}{(X_1^2 + Y_1^2 + Z_1^2)^{\frac{1}{2}} (X_2^2 + Y_2^2 + Z_2^2)^{\frac{1}{2}}} = \frac{X_1}{(X_1^2 + Y_1^2 + Z_1^2)^{\frac{1}{2}}}$$

So $\cos \phi = -0.243281001$ and the angle $\phi = 104.080269 = 104.1$

Then the same way to calculate the angle between [111] to TD ($X_2=0, Y_2=1, Z_2=0$)

and ND ($X_2=0, Y_2=0, Z_2=1$), we got 90.7 and 14.1 respectively.

Appendix II Calculation of Schmid factor from Laue data

This appendix presents an example of the calculation of Schmid factor from Laue data for 18h cracked C-ring sample. The stress axis is in the y direction.

Necessary input: Rotation matrix $\mathcal{G}_{\text{sampleToCrystal}}$ which rotates sample coordinate system to crystal coordinate system

Calculation steps

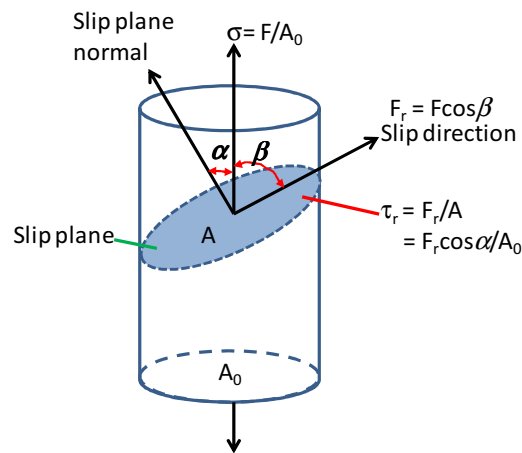


Figure A.1 Illustration of the geometry of slip in a cylinder. Note that $\alpha + \beta \neq 90^\circ$ in general. Adopted from Chapter 1 (Figure 1.3).

1. Express stress vector in the crystal coordinate system

$$\sigma_{\text{crystal}} = \mathcal{G}_{\text{sampleToCrystal}} \cdot \sigma_{\text{sample}}$$

2. For every slip system calculate the following:

$$\cos \alpha \cdot \cos \beta$$

Where α is the angle between σ_{crystal} and normal to the slip plane and β is the angle between σ_{crystal} and slip direction.

Example:

An index file from 2D PXM of 18h cracked C-ring sample after processing:

```

18hCRing_3786.tif
number of grains found:      1
grain no:      0      grainlist file index:      1000
number of indexed reflections:      9
  x(exp)      y(exp)      h      k      l      ang_dev.      xdev(pix)      ydev(pix)      Ener(keV)      2theta(deg)
715.06702      195.14047      0      2      4      0.10254      1.20389      -2.56402      11.08046      89.50659 -1
341.29639      280.30432      1      1      5      0.04763      0.46137      -1.23420      13.61605      83.47250 1
914.76819      384.56485      -1      3      5      0.00261      0.06093      -0.00189      16.39323      78.03152 -2
89.61050      459.43228      2      0      6      0.06117      1.01134      -1.53894      18.52424      73.10780 2
859.37231      67.18979      0      4      6      0.07573      -1.69403      1.35523      16.70286      97.72161 -2
81.82092      169.05539      3      1      7      0.00819      0.20894      0.00564      18.80349      90.89141 2
557.04150      89.68420      1      3      7      0.06143      -0.52993      1.64809      17.92731      96.73356 -
333.19824      171.75166      2      2      8      0.03789      -0.41643      0.94405      20.76752      90.91662 1
983.02307      228.52000      -1      5      7      0.03918      -1.05606      -0.10072      21.81178      87.67423 -3
dev1, dev2, pixdev=      0.0607900      0.0568400      0.0484900
matrix X Y Z -> h k l
  0.25937      0.23857      0.04592
 -0.23879      0.23795      0.11251
  0.04478      -0.11297      0.33396
matrix h k l -> X Y Z
  2.05365      -1.89071      0.35455
  1.88899      1.88404      -0.89447
  0.36362      0.89082      2.64428
Number of missing reflections:      8
x(exp)      y(exp)      h      k      l      energy(keV)      theta(deg)      strfac      theor_integr
369.78546      825.59381      0      0      2      7.93478      52.16798      77.32000      47382.89453
315.65604      2.68067      1      1      3      7.43038      102.27187      55.04300      8323.77539
784.90088      870.57239      -1      1      3      13.23099      51.86016      55.04300      24338.45313
369.78546      825.59381      0      0      4      15.86956      52.16798      46.43600      17090.39648
624.11053      804.80505      -1      1      5      20.21728      53.27464      36.05000      9819.36523
589.18671      343.68069      0      2      6      17.30261      79.23049      30.31700      3037.09790
315.65604      2.68067      2      2      6      14.86076      102.27187      29.20700      2343.69189
350.91037      409.39224      1      1      7      20.49322      74.87411      27.66200      2785.52295
Rfactor:      0.57634002
Rotangle(deg):      47.97391
Rodrigues vector:      -0.19001      0.00097      -0.40227      47.96769
Quaternion:      0.91366      -0.17360      0.00088      -0.36754
Euler angles:      -18.68895      -7.18141      -42.63454
orsnr, orsirxy, orsirxz, orsiryz: 19.99498 -64.69414 71.54382 -64.77228
Rotation matrix, unit cell to sample:
  0.72983      -0.67192      0.12600
  0.67131      0.66955      -0.31788
  0.12922      0.31658      0.93972
Rotation matrix, sample to unit cell:
  0.72983      0.67131      0.12922
 -0.67192      0.66955      0.31658
  0.12600      -0.31788      0.93972

```

In general, use the fourth matrix, rotation matrix, sample to unit cell, as highlighted with blue box above. One calculation is shown as following.

Known: stress axis in sample coordinate system $[010]$, calculate Schmid factor for slip system $\{111\}\bar{1}10$.

1) Calculate σ_{crystal}

$$\begin{aligned}\sigma_{crystal} &= g_{sampleto crystal} \cdot \sigma_{sample} \\ &= \begin{bmatrix} 0.72983 & 0.67131 & 0.12922 \\ -0.67192 & 0.66955 & 0.31658 \\ 0.12600 & -0.31788 & 0.93972 \end{bmatrix} \cdot \begin{bmatrix} 0 \\ 1 \\ 0 \end{bmatrix} \\ &= \begin{bmatrix} 0.67131 \\ 0.66955 \\ -0.31788 \end{bmatrix}\end{aligned}$$

2) Calculate $\cos \alpha$ normal to slip plane is $\mathbf{n} = [111]$

$$\begin{aligned}\cos \alpha &= \frac{\sigma_{crystal} \cdot \mathbf{n}}{|\sigma_{crystal}| \cdot |\mathbf{n}|} \\ &= \frac{\begin{bmatrix} 0.67131 \\ 0.66955 \\ -0.31788 \end{bmatrix} \cdot \begin{bmatrix} 1 \\ 1 \\ 1 \end{bmatrix}}{\sqrt{0.67131^2 + 0.66955^2 + 0.31788^2} \cdot \sqrt{1^2 + 1^2 + 1^2}} \\ &= \frac{1.02298}{\sqrt{3} \cdot \sqrt{0.67131^2 + 0.66955^2 + 0.31788^2}}\end{aligned}$$

3) Calculate $\cos \beta$ slip direction is $\mathbf{d} = [\bar{1}10]$

$$\begin{aligned}\cos \beta &= \frac{\sigma_{crystal} \cdot \mathbf{d}}{|\sigma_{crystal}| \cdot |\mathbf{d}|} \\ &= \frac{\begin{bmatrix} 0.67131 \\ 0.66955 \\ -0.31788 \end{bmatrix} \cdot \begin{bmatrix} -1 \\ 1 \\ 0 \end{bmatrix}}{\sqrt{0.67131^2 + 0.66955^2 + 0.31788^2} \cdot \sqrt{1^2 + 1^2 + 0^2}} \\ &= \frac{-0.00176}{\sqrt{2} \cdot \sqrt{0.67131^2 + 0.66955^2 + 0.31788^2}}\end{aligned}$$

4) Schmid factor for slip system $\{111\}\langle\bar{1}10\rangle$ is

$$m = \cos \alpha \cdot \cos \beta$$

$$= \frac{1.02298 \times (-0.00176)}{\sqrt{6} \cdot (0.67131^2 + 0.66955^2 + 0.31788^2)}$$

$$= -0.000735$$

Take the absolute value, so $m = 0.000735$

5) Use the same method to calculate Schmid factor for all slip systems, take the highest number as the Schmid factor for this grain. Therefore, the Schmid factor for this grain is 0.41311 with the most possible activated slip system $\{111\}\bar{1}01$.

glide plane	glide direction	Schmid factor
	< -1, 1, 0>	0.00073
{ 1, 1, 1}	< -1, 0, 1>	0.41311
	< 0, -1, 1>	0.41238
	< -1, 1, 0>	0.00119
{ -1, -1, 1}	< -1, 0, -1>	0.23934
	< 0, -1, -1>	0.23814
	< 1, 1, 0>	0.17304
{ -1, 1, -1}	< -1, 0, 1>	0.12766
	< 0, -1, -1>	0.04539
	< 1, 1, 0>	0.17497
{ -1, 1, 1}	< -1, 0, -1>	0.04612
	< 0, -1, 1>	0.12885

Appendix III Copyright permissions

ELSEVIER LICENSE TERMS AND CONDITIONS

Jul 07, 2012

This is a License Agreement between Jing Chao ("You") and Elsevier ("Elsevier") provided by Copyright Clearance Center ("CCC"). The license consists of your order details, the terms and conditions provided by Elsevier, and the payment terms and conditions.

All payments must be made in full to CCC. For payment instructions, please see information listed at the bottom of this form.

Supplier	Elsevier Limited The Boulevard, Langford Lane Kidlington, Oxford, OX5 1GB, UK
Registered Company Number	1982084
Customer name	Jing Chao
Customer address	1151 Richmond Street London, ON N6A 5B7
License number	2943841355939
License date	Jul 07, 2012
Licensed content publisher	Elsevier
Licensed content publication	Acta Materialia
Licensed content title	The study of stress application and corrosion cracking on Ni-16 Cr-9 Fe (Alloy 600) C-ring samples by polychromatic X-ray microdiffraction
Licensed content author	Jing Chao, Marina L. Suominen Fuller, N. Stewart McIntyre, Anatolie G. Carcea, Roger C. Newman, Martin Kunz, Nobumichi Tamura
Licensed content date	February 2012
Licensed content volume number	60
Licensed content issue number	3
Number of pages	12
Start Page	781
End Page	792
Type of Use	reuse in a thesis/dissertation
Intended publisher of new work	other
Portion	full article
Format	both print and electronic
Are you the author of this Elsevier article?	Yes
Will you be translating?	No
Order reference number	

Title of your thesis/dissertation	Studies of Microscopic Scale Strains in Nickel Alloys resulting from Mechanical and Chemical Forces
Expected completion date	Sep 2012
Estimated size (number of pages)	180
Elsevier VAT number	GB 494 6272 12
Permissions price	0.00 USD
VAT/Local Sales Tax	0.0 USD / 0.0 GBP
Total	0.00 USD

[Terms and Conditions](#)

INTRODUCTION

1. The publisher for this copyrighted material is Elsevier. By clicking "accept" in connection with completing this licensing transaction, you agree that the following terms and conditions apply to this transaction (along with the Billing and Payment terms and conditions established by Copyright Clearance Center, Inc. ("CCC"), at the time that you opened your Rightslink account and that are available at any time at <http://myaccount.copyright.com>).

GENERAL TERMS

2. Elsevier hereby grants you permission to reproduce the aforementioned material subject to the terms and conditions indicated.

3. Acknowledgement: If any part of the material to be used (for example, figures) has appeared in our publication with credit or acknowledgement to another source, permission must also be sought from that source. If such permission is not obtained then that material may not be included in your publication/copies. Suitable acknowledgement to the source must be made, either as a footnote or in a reference list at the end of your publication, as follows:

"Reprinted from Publication title, Vol /edition number, Author(s), Title of article / title of chapter, Pages No., Copyright (Year), with permission from Elsevier [OR APPLICABLE SOCIETY COPYRIGHT OWNER]." Also Lancet special credit - "Reprinted from The Lancet, Vol. number, Author(s), Title of article, Pages No., Copyright (Year), with permission from Elsevier."

4. Reproduction of this material is confined to the purpose and/or media for which permission is hereby given.

5. Altering/Modifying Material: Not Permitted. However figures and illustrations may be altered/adapted minimally to serve your work. Any other abbreviations, additions, deletions and/or any other alterations shall be made only with prior written authorization of Elsevier Ltd. (Please contact Elsevier at permissions@elsevier.com)

6. If the permission fee for the requested use of our material is waived in this instance, please be advised that your future requests for Elsevier materials may attract a fee.

7. Reservation of Rights: Publisher reserves all rights not specifically granted in the combination of (i) the license details provided by you and accepted in the course of this

licensing transaction, (ii) these terms and conditions and (iii) CCC's Billing and Payment terms and conditions.

8. License Contingent Upon Payment: While you may exercise the rights licensed immediately upon issuance of the license at the end of the licensing process for the transaction, provided that you have disclosed complete and accurate details of your proposed use, no license is finally effective unless and until full payment is received from you (either by publisher or by CCC) as provided in CCC's Billing and Payment terms and conditions. If full payment is not received on a timely basis, then any license preliminarily granted shall be deemed automatically revoked and shall be void as if never granted. Further, in the event that you breach any of these terms and conditions or any of CCC's Billing and Payment terms and conditions, the license is automatically revoked and shall be void as if never granted. Use of materials as described in a revoked license, as well as any use of the materials beyond the scope of an unrevoked license, may constitute copyright infringement and publisher reserves the right to take any and all action to protect its copyright in the materials.

9. Warranties: Publisher makes no representations or warranties with respect to the licensed material.

10. Indemnity: You hereby indemnify and agree to hold harmless publisher and CCC, and their respective officers, directors, employees and agents, from and against any and all claims arising out of your use of the licensed material other than as specifically authorized pursuant to this license.

11. No Transfer of License: This license is personal to you and may not be sublicensed, assigned, or transferred by you to any other person without publisher's written permission.

12. No Amendment Except in Writing: This license may not be amended except in a writing signed by both parties (or, in the case of publisher, by CCC on publisher's behalf).

13. Objection to Contrary Terms: Publisher hereby objects to any terms contained in any purchase order, acknowledgment, check endorsement or other writing prepared by you, which terms are inconsistent with these terms and conditions or CCC's Billing and Payment terms and conditions. These terms and conditions, together with CCC's Billing and Payment terms and conditions (which are incorporated herein), comprise the entire agreement between you and publisher (and CCC) concerning this licensing transaction. In the event of any conflict between your obligations established by these terms and conditions and those established by CCC's Billing and Payment terms and conditions, these terms and conditions shall control.

14. Revocation: Elsevier or Copyright Clearance Center may deny the permissions described in this License at their sole discretion, for any reason or no reason, with a full refund payable to you. Notice of such denial will be made using the contact information provided by you. Failure to receive such notice will not alter or invalidate the denial. In no event will Elsevier or Copyright Clearance Center be responsible or liable for any costs, expenses or damage incurred by you as a result of a denial of your permission request, other than a refund of the amount(s) paid by you to Elsevier and/or Copyright Clearance Center for denied permissions.

LIMITED LICENSE

The following terms and conditions apply only to specific license types:

15. Translation: This permission is granted for non-exclusive world **English** rights only unless your license was granted for translation rights. If you licensed translation rights you may only translate this content into the languages you requested. A professional translator must perform all translations and reproduce the content word for word preserving the integrity of the article. If this license is to re-use 1 or 2 figures then permission is granted for non-exclusive world rights in all languages.

16. Website: The following terms and conditions apply to electronic reserve and author websites:

Electronic reserve: If licensed material is to be posted to website, the web site is to be password-protected and made available only to bona fide students registered on a relevant course if:

This license was made in connection with a course,

This permission is granted for 1 year only. You may obtain a license for future website posting.

All content posted to the web site must maintain the copyright information line on the bottom of each image,

A hyper-text must be included to the Homepage of the journal from which you are licensing at <http://www.sciencedirect.com/science/journal/xxxxx> or the Elsevier homepage for books at <http://www.elsevier.com> , and

Central Storage: This license does not include permission for a scanned version of the material to be stored in a central repository such as that provided by Heron/XanEdu.

17. Author website for journals with the following additional clauses:

All content posted to the web site must maintain the copyright information line on the bottom of each image, and the permission granted is limited to the personal version of your paper. You are not allowed to download and post the published electronic version of your article (whether PDF or HTML, proof or final version), nor may you scan the printed edition to create an electronic version. A hyper-text must be included to the Homepage of the journal from which you are licensing at <http://www.sciencedirect.com/science/journal/xxxxx>

. As part of our normal production process, you will receive an e-mail notice when your article appears on Elsevier's online service ScienceDirect (www.sciencedirect.com). That e-mail will include the article's Digital Object Identifier (DOI). This number provides the electronic link to the published article and should be included in the posting of your personal version. We ask that you wait until you receive this e-mail and have the DOI to do any posting.

Central Storage: This license does not include permission for a scanned version of the material to be stored in a central repository such as that provided by Heron/XanEdu.

18. Author website for books with the following additional clauses:

Authors are permitted to place a brief summary of their work online only.

A hyper-text must be included to the Elsevier homepage at <http://www.elsevier.com> . All content posted to the web site must maintain the copyright information line on the bottom of each image. You are not allowed to download and post the published electronic version of your chapter, nor may you scan the printed edition to create an electronic version.

Central Storage: This license does not include permission for a scanned version of the

material to be stored in a central repository such as that provided by Heron/XanEdu.

19. **Website** (regular and for author): A hyper-text must be included to the Homepage of the journal from which you are licensing at <http://www.sciencedirect.com/science/journal/xxxxx>. or for books to the Elsevier homepage at <http://www.elsevier.com>

20. **Thesis/Dissertation**: If your license is for use in a thesis/dissertation your thesis may be submitted to your institution in either print or electronic form. Should your thesis be published commercially, please reapply for permission. These requirements include permission for the Library and Archives of Canada to supply single copies, on demand, of the complete thesis and include permission for UMI to supply single copies, on demand, of the complete thesis. Should your thesis be published commercially, please reapply for permission.

21. **Other Conditions**:

v1.6

If you would like to pay for this license now, please remit this license along with your payment made payable to "COPYRIGHT CLEARANCE CENTER" otherwise you will be invoiced within 48 hours of the license date. Payment should be in the form of a check or money order referencing your account number and this invoice number RLNK500814025.

Once you receive your invoice for this order, you may pay your invoice by credit card. Please follow instructions provided at that time.

Make Payment To:
Copyright Clearance Center
Dept 001
P.O. Box 843006
Boston, MA 02284-3006

For suggestions or comments regarding this order, contact RightsLink Customer Support: customercare@copyright.com or +1-877-622-5543 (toll free in the US) or +1-978-646-2777.

Gratis licenses (referencing \$0 in the Total field) are free. Please retain this printable license for your reference. No payment is required.

**ELSEVIER LICENSE
TERMS AND CONDITIONS**

Jul 07, 2012

This is a License Agreement between Jing Chao ("You") and Elsevier ("Elsevier") provided by Copyright Clearance Center ("CCC"). The license consists of your order details, the terms and conditions provided by Elsevier, and the payment terms and conditions.

All payments must be made in full to CCC. For payment instructions, please see information listed at the bottom of this form.

Supplier	Elsevier Limited The Boulevard, Langford Lane Kidlington, Oxford, OX5 1GB, UK
Registered Company Number	1982084
Customer name	Jing Chao
Customer address	1151 Richmond Street London, ON N6A 5B7
License number	2943840276208
License date	Jul 07, 2012
Licensed content publisher	Elsevier
Licensed content publication	Materials Science and Engineering: A
Licensed content title	Study of residual elastic- and plastic-deformation in uniaxial tensile strained nickel-based Alloy 600 samples by polychromatic X-ray microdiffraction (PXM) and neutron diffraction methods
Licensed content author	Jing Chao, Alison Mark, Marina L. Suominen Fuller, N. Stewart McIntyre, Richard A. Holt, Robert J. Klassen, Wenjun Liu
Licensed content date	25 October 2009
Licensed content volume number	524
Licensed content issue number	1-2
Number of pages	8
Start Page	20
End Page	27
Type of Use	reuse in a thesis/dissertation
Portion	full article
Format	both print and electronic
Are you the author of this Elsevier article?	Yes
Will you be translating?	No
Order reference number	
Title of your thesis/dissertation	Studies of Microscopic Scale Strains in Nickel Alloys resulting from Mechanical and Chemical Forces

Expected completion date	Sep 2012
Estimated size (number of pages)	180
Elsevier VAT number	GB 494 6272 12
Permissions price	0.00 USD
VAT/Local Sales Tax	0.0 USD / 0.0 GBP
Total	0.00 USD
Terms and Conditions	

INTRODUCTION

1. The publisher for this copyrighted material is Elsevier. By clicking "accept" in connection with completing this licensing transaction, you agree that the following terms and conditions apply to this transaction (along with the Billing and Payment terms and conditions established by Copyright Clearance Center, Inc. ("CCC"), at the time that you opened your Rightslink account and that are available at any time at <http://myaccount.copyright.com>).

GENERAL TERMS

2. Elsevier hereby grants you permission to reproduce the aforementioned material subject to the terms and conditions indicated.

3. Acknowledgement: If any part of the material to be used (for example, figures) has appeared in our publication with credit or acknowledgement to another source, permission must also be sought from that source. If such permission is not obtained then that material may not be included in your publication/copies. Suitable acknowledgement to the source must be made, either as a footnote or in a reference list at the end of your publication, as follows:

"Reprinted from Publication title, Vol /edition number, Author(s), Title of article / title of chapter, Pages No., Copyright (Year), with permission from Elsevier [OR APPLICABLE SOCIETY COPYRIGHT OWNER]." Also Lancet special credit - "Reprinted from The Lancet, Vol. number, Author(s), Title of article, Pages No., Copyright (Year), with permission from Elsevier."

4. Reproduction of this material is confined to the purpose and/or media for which permission is hereby given.

5. Altering/Modifying Material: Not Permitted. However figures and illustrations may be altered/adapted minimally to serve your work. Any other abbreviations, additions, deletions and/or any other alterations shall be made only with prior written authorization of Elsevier Ltd. (Please contact Elsevier at permissions@elsevier.com)

6. If the permission fee for the requested use of our material is waived in this instance, please be advised that your future requests for Elsevier materials may attract a fee.

7. Reservation of Rights: Publisher reserves all rights not specifically granted in the combination of (i) the license details provided by you and accepted in the course of this licensing transaction, (ii) these terms and conditions and (iii) CCC's Billing and Payment terms and conditions.

8. **License Contingent Upon Payment:** While you may exercise the rights licensed immediately upon issuance of the license at the end of the licensing process for the transaction, provided that you have disclosed complete and accurate details of your proposed use, no license is finally effective unless and until full payment is received from you (either by publisher or by CCC) as provided in CCC's Billing and Payment terms and conditions. If full payment is not received on a timely basis, then any license preliminarily granted shall be deemed automatically revoked and shall be void as if never granted. Further, in the event that you breach any of these terms and conditions or any of CCC's Billing and Payment terms and conditions, the license is automatically revoked and shall be void as if never granted. Use of materials as described in a revoked license, as well as any use of the materials beyond the scope of an unrevoked license, may constitute copyright infringement and publisher reserves the right to take any and all action to protect its copyright in the materials.

9. **Warranties:** Publisher makes no representations or warranties with respect to the licensed material.

10. **Indemnity:** You hereby indemnify and agree to hold harmless publisher and CCC, and their respective officers, directors, employees and agents, from and against any and all claims arising out of your use of the licensed material other than as specifically authorized pursuant to this license.

11. **No Transfer of License:** This license is personal to you and may not be sublicensed, assigned, or transferred by you to any other person without publisher's written permission.

12. **No Amendment Except in Writing:** This license may not be amended except in a writing signed by both parties (or, in the case of publisher, by CCC on publisher's behalf).

13. **Objection to Contrary Terms:** Publisher hereby objects to any terms contained in any purchase order, acknowledgment, check endorsement or other writing prepared by you, which terms are inconsistent with these terms and conditions or CCC's Billing and Payment terms and conditions. These terms and conditions, together with CCC's Billing and Payment terms and conditions (which are incorporated herein), comprise the entire agreement between you and publisher (and CCC) concerning this licensing transaction. In the event of any conflict between your obligations established by these terms and conditions and those established by CCC's Billing and Payment terms and conditions, these terms and conditions shall control.

14. **Revocation:** Elsevier or Copyright Clearance Center may deny the permissions described in this License at their sole discretion, for any reason or no reason, with a full refund payable to you. Notice of such denial will be made using the contact information provided by you. Failure to receive such notice will not alter or invalidate the denial. In no event will Elsevier or Copyright Clearance Center be responsible or liable for any costs, expenses or damage incurred by you as a result of a denial of your permission request, other than a refund of the amount(s) paid by you to Elsevier and/or Copyright Clearance Center for denied permissions.

LIMITED LICENSE

The following terms and conditions apply only to specific license types:

15. **Translation:** This permission is granted for non-exclusive world **English** rights only unless your license was granted for translation rights. If you licensed translation rights you may only translate this content into the languages you requested. A professional translator must perform all translations and reproduce the content word for word preserving the integrity of the article. If this license is to re-use 1 or 2 figures then permission is granted for non-exclusive world rights in all languages.

16. **Website:** The following terms and conditions apply to electronic reserve and author websites:

Electronic reserve: If licensed material is to be posted to website, the web site is to be password-protected and made available only to bona fide students registered on a relevant course if:

This license was made in connection with a course,

This permission is granted for 1 year only. You may obtain a license for future website posting.

All content posted to the web site must maintain the copyright information line on the bottom of each image,

A hyper-text must be included to the Homepage of the journal from which you are licensing at <http://www.sciencedirect.com/science/journal/xxxxx> or the Elsevier homepage for books at <http://www.elsevier.com> , and

Central Storage: This license does not include permission for a scanned version of the material to be stored in a central repository such as that provided by Heron/XanEdu.

17. **Author website** for journals with the following additional clauses:

All content posted to the web site must maintain the copyright information line on the bottom of each image, and the permission granted is limited to the personal version of your paper. You are not allowed to download and post the published electronic version of your article (whether PDF or HTML, proof or final version), nor may you scan the printed edition to create an electronic version. A hyper-text must be included to the Homepage of the journal from which you are licensing at <http://www.sciencedirect.com/science/journal/xxxxx> . As part of our normal production process, you will receive an e-mail notice when your article appears on Elsevier's online service ScienceDirect (www.sciencedirect.com). That e-mail will include the article's Digital Object Identifier (DOI). This number provides the electronic link to the published article and should be included in the posting of your personal version. We ask that you wait until you receive this e-mail and have the DOI to do any posting.

Central Storage: This license does not include permission for a scanned version of the material to be stored in a central repository such as that provided by Heron/XanEdu.

18. **Author website** for books with the following additional clauses:

Authors are permitted to place a brief summary of their work online only.

A hyper-text must be included to the Elsevier homepage at <http://www.elsevier.com> . All content posted to the web site must maintain the copyright information line on the bottom of each image. You are not allowed to download and post the published electronic version of your chapter, nor may you scan the printed edition to create an electronic version.

Central Storage: This license does not include permission for a scanned version of the material to be stored in a central repository such as that provided by Heron/XanEdu.

19. **Website** (regular and for author): A hyper-text must be included to the Homepage of the journal from which you are licensing at <http://www.sciencedirect.com/science/journal/xxxxx>. or for books to the Elsevier homepage at <http://www.elsevier.com>

20. **Thesis/Dissertation**: If your license is for use in a thesis/dissertation your thesis may be submitted to your institution in either print or electronic form. Should your thesis be published commercially, please reapply for permission. These requirements include permission for the Library and Archives of Canada to supply single copies, on demand, of the complete thesis and include permission for UMI to supply single copies, on demand, of the complete thesis. Should your thesis be published commercially, please reapply for permission.

21. **Other Conditions**:

v1.6

If you would like to pay for this license now, please remit this license along with your payment made payable to "COPYRIGHT CLEARANCE CENTER" otherwise you will be invoiced within 48 hours of the license date. Payment should be in the form of a check or money order referencing your account number and this invoice number RLNK500814020.

Once you receive your invoice for this order, you may pay your invoice by credit card. Please follow instructions provided at that time.

**Make Payment To:
Copyright Clearance Center
Dept 001
P.O. Box 843006
Boston, MA 02284-3006**

For suggestions or comments regarding this order, contact RightsLink Customer Support: customercare@copyright.com or +1-877-622-5543 (toll free in the US) or +1-978-646-2777.

Gratis licenses (referencing \$0 in the Total field) are free. Please retain this printable license for your reference. No payment is required.

**CAMBRIDGE UNIVERSITY PRESS LICENSE
TERMS AND CONDITIONS**

Jul 07, 2012

This is a License Agreement between Jing Chao ("You") and Cambridge University Press ("Cambridge University Press") provided by Copyright Clearance Center ("CCC"). The license consists of your order details, the terms and conditions provided by Cambridge University Press, and the payment terms and conditions.

All payments must be made in full to CCC. For payment instructions, please see information listed at the bottom of this form.

License Number	2943841037915
License date	Jul 07, 2012
Licensed content publisher	Cambridge University Press
Licensed content publication	MRS Online Proceedings Library
Licensed content title	X-ray Micro Laue Diffraction and Neutron Diffraction Analysis of Residual Elastic Strains in a 1% Uniaxial Tensile Tested Nickel Alloy 600 Sample
Licensed content author	
Licensed content date	Dec 31, 1969
Volume number	1137
Issue number	-1
Start page	0
End page	0
Type of Use	Dissertation/Thesis
Requestor type	Author
Portion	Full article
Author of this Cambridge University Press article	Yes
Author / editor of the new work	Yes
Order reference number	
Territory for reuse	World
Title of your thesis / dissertation	Studies of Microscopic Scale Strains in Nickel Alloys resulting from Mechanical and Chemical Forces
Expected completion date	Sep 2012
Estimated size(pages)	180
Billing Type	Invoice
Billing address	1151 Richmond Street Chemistry Building, Western University London, ON N6A 5B7 Canada

Customer reference info

Total 0.00 USD

Terms and Conditions

TERMS & CONDITIONS

Cambridge University Press grants the Licensee permission on a non-exclusive non-transferable basis to reproduce, make available or otherwise use the Licensed content 'Content' in the named territory 'Territory' for the purpose listed 'the Use' on Page 1 of this Agreement subject to the following terms and conditions.

1. The License is limited to the permission granted and the Content detailed herein and does not extend to any other permission or content.
2. Cambridge gives no warranty or indemnity in respect of any third-party copyright material included in the Content, for which the Licensee should seek separate permission clearance.
3. The integrity of the Content must be ensured.
4. The License does extend to any edition published specifically for the use of handicapped or reading-impaired individuals.
5. The Licensee shall provide a prominent acknowledgement in the following format: author/s, title of article, name of journal, volume number, issue number, page references, , reproduced with permission.

Other terms and conditions: None

v1.0

If you would like to pay for this license now, please remit this license along with your payment made payable to "COPYRIGHT CLEARANCE CENTER" otherwise you will be invoiced within 48 hours of the license date. Payment should be in the form of a check or money order referencing your account number and this invoice number RLNK500814024.

Once you receive your invoice for this order, you may pay your invoice by credit card. Please follow instructions provided at that time.

**Make Payment To:
Copyright Clearance Center
Dept 001
P.O. Box 843006
Boston, MA 02284-3006**

For suggestions or comments regarding this order, contact RightsLink Customer Support: customercare@copyright.com or +1-877-622-5543 (toll free in the US) or +1-978-646-2777.

Gratis licenses (referencing \$0 in the Total field) are free. Please retain this printable license for your reference. No payment is required.

**ELSEVIER LICENSE
TERMS AND CONDITIONS**

Aug 22, 2012

This is a License Agreement between Jing Chao ("You") and Elsevier ("Elsevier") provided by Copyright Clearance Center ("CCC"). The license consists of your order details, the terms and conditions provided by Elsevier, and the payment terms and conditions.

All payments must be made in full to CCC. For payment instructions, please see information listed at the bottom of this form.

Supplier	Elsevier Limited The Boulevard, Langford Lane Kidlington, Oxford, OX5 1GB, UK
Registered Company Number	1982084
Customer name	Jing Chao
Customer address	1151 Richmond Street London, ON N6A 5B7
License number	2974480140078
License date	Aug 22, 2012
Licensed content publisher	Elsevier
Licensed content publication	Acta Materialia
Licensed content title	Plastic and elastic strains in short and long cracks in Alloy 600 studied by polychromatic X-ray microdiffraction and electron backscatter diffraction
Licensed content author	Jing Chao, Marina L. Suominen Fuller, Nathaniel Sherry, Jinhui Qin, N. Stewart McIntyre, Jaganathan Ulaganathan, Anatolie G. Carcea, Roger C. Newman, Martin Kunz, Nobumichi Tamura
Licensed content date	September 2012
Licensed content volume number	60
Licensed content issue number	15
Number of pages	8
Start Page	5508
End Page	5515
Type of Use	reuse in a thesis/dissertation
Portion	full article
Format	both print and electronic
Are you the author of this Elsevier article?	Yes
Will you be translating?	No
Order reference number	
Title of your thesis/dissertation	Studies of Microscopic Scale Strains in Nickel Alloys resulting from Mechanical and Chemical Forces

Expected completion date	Oct 2012
Estimated size (number of pages)	180
Elsevier VAT number	GB 494 6272 12
Permissions price	0.00 USD
VAT/Local Sales Tax	0.0 USD / 0.0 GBP
Total	0.00 USD
Terms and Conditions	

INTRODUCTION

1. The publisher for this copyrighted material is Elsevier. By clicking "accept" in connection with completing this licensing transaction, you agree that the following terms and conditions apply to this transaction (along with the Billing and Payment terms and conditions established by Copyright Clearance Center, Inc. ("CCC"), at the time that you opened your Rightslink account and that are available at any time at <http://myaccount.copyright.com>).

GENERAL TERMS

2. Elsevier hereby grants you permission to reproduce the aforementioned material subject to the terms and conditions indicated.

3. Acknowledgement: If any part of the material to be used (for example, figures) has appeared in our publication with credit or acknowledgement to another source, permission must also be sought from that source. If such permission is not obtained then that material may not be included in your publication/copies. Suitable acknowledgement to the source must be made, either as a footnote or in a reference list at the end of your publication, as follows:

“Reprinted from Publication title, Vol /edition number, Author(s), Title of article / title of chapter, Pages No., Copyright (Year), with permission from Elsevier [OR APPLICABLE SOCIETY COPYRIGHT OWNER].” Also Lancet special credit - “Reprinted from The Lancet, Vol. number, Author(s), Title of article, Pages No., Copyright (Year), with permission from Elsevier.”

4. Reproduction of this material is confined to the purpose and/or media for which permission is hereby given.

5. Altering/Modifying Material: Not Permitted. However figures and illustrations may be altered/adapted minimally to serve your work. Any other abbreviations, additions, deletions and/or any other alterations shall be made only with prior written authorization of Elsevier Ltd. (Please contact Elsevier at permissions@elsevier.com)

6. If the permission fee for the requested use of our material is waived in this instance, please be advised that your future requests for Elsevier materials may attract a fee.

7. Reservation of Rights: Publisher reserves all rights not specifically granted in the combination of (i) the license details provided by you and accepted in the course of this licensing transaction, (ii) these terms and conditions and (iii) CCC's Billing and Payment terms and conditions.

8. License Contingent Upon Payment: While you may exercise the rights licensed immediately upon issuance of the license at the end of the licensing process for the transaction, provided that you have disclosed complete and accurate details of your proposed use, no license is finally effective unless and until full payment is received from you (either by publisher or by CCC) as provided in CCC's Billing and Payment terms and conditions. If full payment is not received on a timely basis, then any license preliminarily granted shall be deemed automatically revoked and shall be void as if never granted. Further, in the event that you breach any of these terms and conditions or any of CCC's Billing and Payment terms and conditions, the license is automatically revoked and shall be void as if never granted. Use of materials as described in a revoked license, as well as any use of the materials beyond the scope of an unrevoked license, may constitute copyright infringement and publisher reserves the right to take any and all action to protect its copyright in the materials.

9. Warranties: Publisher makes no representations or warranties with respect to the licensed material.

10. Indemnity: You hereby indemnify and agree to hold harmless publisher and CCC, and their respective officers, directors, employees and agents, from and against any and all claims arising out of your use of the licensed material other than as specifically authorized pursuant to this license.

11. No Transfer of License: This license is personal to you and may not be sublicensed, assigned, or transferred by you to any other person without publisher's written permission.

12. No Amendment Except in Writing: This license may not be amended except in a writing signed by both parties (or, in the case of publisher, by CCC on publisher's behalf).

13. Objection to Contrary Terms: Publisher hereby objects to any terms contained in any purchase order, acknowledgment, check endorsement or other writing prepared by you, which terms are inconsistent with these terms and conditions or CCC's Billing and Payment terms and conditions. These terms and conditions, together with CCC's Billing and Payment terms and conditions (which are incorporated herein), comprise the entire agreement between you and publisher (and CCC) concerning this licensing transaction. In the event of any conflict between your obligations established by these terms and conditions and those established by CCC's Billing and Payment terms and conditions, these terms and conditions shall control.

14. Revocation: Elsevier or Copyright Clearance Center may deny the permissions described in this License at their sole discretion, for any reason or no reason, with a full refund payable to you. Notice of such denial will be made using the contact information provided by you. Failure to receive such notice will not alter or invalidate the denial. In no event will Elsevier or Copyright Clearance Center be responsible or liable for any costs, expenses or damage incurred by you as a result of a denial of your permission request, other than a refund of the amount(s) paid by you to Elsevier and/or Copyright Clearance Center for denied permissions.

LIMITED LICENSE

The following terms and conditions apply only to specific license types:

15. **Translation:** This permission is granted for non-exclusive world **English** rights only unless your license was granted for translation rights. If you licensed translation rights you may only translate this content into the languages you requested. A professional translator must perform all translations and reproduce the content word for word preserving the integrity of the article. If this license is to re-use 1 or 2 figures then permission is granted for non-exclusive world rights in all languages.

16. **Website:** The following terms and conditions apply to electronic reserve and author websites:

Electronic reserve: If licensed material is to be posted to website, the web site is to be password-protected and made available only to bona fide students registered on a relevant course if:

This license was made in connection with a course,

This permission is granted for 1 year only. You may obtain a license for future website posting,

All content posted to the web site must maintain the copyright information line on the bottom of each image,

A hyper-text must be included to the Homepage of the journal from which you are licensing at <http://www.sciencedirect.com/science/journal/xxxxx> or the Elsevier homepage for books at <http://www.elsevier.com> , and

Central Storage: This license does not include permission for a scanned version of the material to be stored in a central repository such as that provided by Heron/XanEdu.

17. **Author website** for journals with the following additional clauses:

All content posted to the web site must maintain the copyright information line on the bottom of each image, and the permission granted is limited to the personal version of your paper. You are not allowed to download and post the published electronic version of your article (whether PDF or HTML, proof or final version), nor may you scan the printed edition to create an electronic version. A hyper-text must be included to the Homepage of the journal from which you are licensing at <http://www.sciencedirect.com/science/journal/xxxxx> . As part of our normal production process, you will receive an e-mail notice when your article appears on Elsevier's online service ScienceDirect (www.sciencedirect.com). That e-mail will include the article's Digital Object Identifier (DOI). This number provides the electronic link to the published article and should be included in the posting of your personal version. We ask that you wait until you receive this e-mail and have the DOI to do any posting.

Central Storage: This license does not include permission for a scanned version of the material to be stored in a central repository such as that provided by Heron/XanEdu.

18. **Author website** for books with the following additional clauses:

Authors are permitted to place a brief summary of their work online only.

A hyper-text must be included to the Elsevier homepage at <http://www.elsevier.com> . All content posted to the web site must maintain the copyright information line on the bottom of each image. You are not allowed to download and post the published electronic version of your chapter, nor may you scan the printed edition to create an electronic version.

Central Storage: This license does not include permission for a scanned version of the material to be stored in a central repository such as that provided by Heron/XanEdu.

19. **Website** (regular and for author): A hyper-text must be included to the Homepage of the journal from which you are licensing at <http://www.sciencedirect.com/science/journal/xxxxx>. or for books to the Elsevier homepage at <http://www.elsevier.com>

20. **Thesis/Dissertation**: If your license is for use in a thesis/dissertation your thesis may be submitted to your institution in either print or electronic form. Should your thesis be published commercially, please reapply for permission. These requirements include permission for the Library and Archives of Canada to supply single copies, on demand, of the complete thesis and include permission for UMI to supply single copies, on demand, of the complete thesis. Should your thesis be published commercially, please reapply for permission.

21. **Other Conditions**:

v1.6

If you would like to pay for this license now, please remit this license along with your payment made payable to "COPYRIGHT CLEARANCE CENTER" otherwise you will be invoiced within 48 hours of the license date. Payment should be in the form of a check or money order referencing your account number and this invoice number RLNK500843683.

Once you receive your invoice for this order, you may pay your invoice by credit card. Please follow instructions provided at that time.

**Make Payment To:
Copyright Clearance Center
Dept 001
P.O. Box 843006
Boston, MA 02284-3006**

For suggestions or comments regarding this order, contact RightsLink Customer Support: customercare@copyright.com or +1-877-622-5543 (toll free in the US) or +1-978-646-2777.

Gratis licenses (referencing \$0 in the Total field) are free. Please retain this printable license for your reference. No payment is required.

Curriculum Vitae

Name: Jing Chao

Post-secondary Education and Degrees: University of Western Ontario
London, Ontario Canada
2006-2012 Ph.D

University of Science and Technology of China
Hefei, Anhui China
2003-2006 M.Sc

Anhui University
Hefei, Anhui China
1999-2003 B.Eng

Honors and Awards: Western Graduate Research Scholarship
University of Western Ontario
2006 – 2011

Outstanding Undergraduate Student Scholarship (2nd)
Anhui University
2002 – 2003

Outstanding Undergraduate Student Scholarship (1st)
Anhui University
2001 – 2002

Outstanding Undergraduate Student Scholarship (3rd)
Anhui University
2000 – 2001

Outstanding Undergraduate Student Scholarship (3rd)
Anhui University
1999 – 2000

Related Work Experience Teaching Assistant, Research Assistant
The University of Western Ontario
2006-2011

Research Assistant
University of Science and Technology of China
2003-2006

Publications:

J. Chao, M. L. S. Fuller, N. Sherry, J. Qin, N. S. McIntyre, J. Ulaganathan, A. G. Carcea, R. C. Newman, M. Kunz and N. Tamura, Plastic and Elastic Strains in Short and Long Cracks in Alloy 600 studied by Polychromatic X-ray Microdiffraction (PXM) and Electron Backscatter Diffraction (EBSD). *Acta Materialia* **2012**, accepted.

J. Chao, M. L. S. Fuller, N. S. McIntyre, A. G. Carcea, R. C. Newman, M. Kunz and N. Tamura, The study of stress application and corrosion cracking on Ni-16 Cr-9 Fe (Alloy 600) C-ring samples by polychromatic X-ray microdiffraction. *Acta Materialia* **2012**, 60 (3), 781-792.

J. Chao, M. L. S. Fuller, N. S. McIntyre, A. G. Carcea, R. C. Newman, M. Kunz and N. Tamura, The Study of Stress Corrosion Cracking on Alloy 600 C-Ring Samples by Polychromatic X-Ray Microdiffraction in *15th International Conference on Environmental Degradation*, edited by J. T. Busby, G. Ilevbare, & P. L. Andesen (The Minerals, Metals & Materials Society, Colorado, **2011**), 1773-1782.

J. Chao, M. Suominen Fuller, S. Ramamurthy, N.S. McIntyre, and R. Feng, Polychromatic x-ray microdiffraction (PXM) of local stress corrosion cracking in alloy 600 using the VESPERS beamline. *Canadian Light Source Activity Report* **2009**, 146-147.

J. Chao, A.F. Mark, M.L. Suominen Fuller, N.S. McIntyre, R.A. Holt, O. Yong, R.J. Klassen, L.W.M. Lau and S. Ramamurthy, Assessment of the validity of polychromatic x-ray microdiffraction (PXM) for strain studies of alloy 600. COG Report No. COG-08-4070, Mar. **2009**.

J. Chao, A. Mark, M.L. Suominen Fuller, N. S. McIntyre, R.A. Holt, R.J. Klassen, W. Liu, Study of residual elastic- and plastic- deformation in uniaxial tensile strained nickel-based alloy 600 samples by polychromatic x-ray microdiffraction (PXM) and neutron diffraction method. *Material Science and Engineering A* **2009**, 524, 20-27.

J. Chao, A. Mark, M.L. Suominen Fuller, R.I. Barabash, N.S. McIntyre, R.A. Holt, R.J. Klassen, W. Liu, X-ray micro Laue diffraction and neutron diffraction analysis of residual elastic strains in a 1% uniaxial tensile tested nickel alloy 600 sample. *Materials Research Society Symposium Proceedings* **2009**, 1137E, 10-28.

J. Chao, X.Y. Zhang, J.B. Dai, Z. Ge, L.L. Feng, Synthesis of a novel core-shell type acrylic-polyurethane hybrid emulsion containing siloxane and fluorine as well as water and the oil resistances of cured films. *Chinese Chemical letters* **2006**, 17 (8), 1121-1124.

Conferences/Poster Presentations:

24th Canadian Materials Science Conference (June 5 – 8, 2012)
University of Western Ontario, London ON, Canada

2011 Advanced Light Source user meeting (October 3-5, 2011), Poster
Lawrence Berkeley National Laboratory, California, USA

2011 CAMBR Distinguished Lecturer and Research Day (June 23, 2011) Poster
London, Ontario, Canada

2010 Canadian Light Source Users' Meeting (June 17-18, 2010) Poster, 2nd Prize
Saskatoon, Saskatchewan Canada

92nd Canadian Chemistry Conference and Exhibition (May 30-June 3, 2009) Oral
presentation
Hamilton, Ontario Canada

2008 Advanced Photon Source User Meeting (May 4-8, 2008) Poster
Argonne National Laboratory, Chicago, USA